THE UNIVERSITY OF MANITOBA

FEASIBILITY INVESTIGATION OF THE MEASUREMENT OF ^{5}He(g.s., $\frac{3}{2}^-$) TENSOR POLARIZATION IN THE $^4\mathrm{He}(\vec{\mathrm{p}},\pi^+)^5\mathrm{He} \longrightarrow \mathrm{n} + \alpha$ REACTION AT $T_p = 400$ MeV

by

HUAIQUN GUAN

A THESIS

SUBMITTED TO THE

FACULTY OF GRADUATE STUDIES AND RESEARCH

IN PARTIAL FULFILLMENT OF THE REQUIREMENTS

FOR THE DEGREE OF MASTER OF SCIENCE

IN

NUCLEAR PHYSICS

DEPARTMENT OF PHYSICS

WINNIPEG, MANITOBA

April 1, 1992

ISBN 0-315-77958-6

THE UNIVERSITY OF MANITOBA

FEASIBILITY INVESTIGATION OF THE MEASUREMENT OF ^{5}He(g.s., $\frac{3}{2}^-$) TENSOR POLARIZATION IN THE $^4\mathrm{He}(\vec{p},\pi^+)^5\mathrm{He} \longrightarrow \mathrm{n} + \alpha$ REACTION AT $T_p = 400$ MeV

by

HUAIQUN GUAN

A Thesis submitted to the Faculty of Graduate Studies of the University of Manitoba in partial fulfillment of the requirements for the degree of

MASTER OF SCIENCE

Abstract

A detailed feasibility investigation has been undertaken for the measurement of the tensor polarization of the recoiling ^{5}He nucleus in the $^4\mathrm{He}(\vec{\mathrm{p}},\pi^+)^5\mathrm{He}$ reaction. The ^{5}He(g.s.) nucleus ($\mathrm{J^P} = \frac{3}{2}^-$) decays strongly to a neutron and an α particle. By measuring the distribution of the α-particles, the information for the determination of the polarization tensors t_{kq} is obtained. In the transverse frame, these tensors are restricted to t_{00}, t_{20} and t_{22}.

For such a feasibility investigation, a Monte Carlo simulation was performed which included the effects of finite geometry, beam divergence, pion and α-particle energy loss and multiple scattering. The event reconstruction to the ^{5}He c.m. system was then carried out for these simulated laboratory distributions. Finally, a least squares and a maximum likelihood fitting procedure were applied to analyse the data to extract the t_{kq} polarization tensors.

As well, physical and practical considerations of a design for a ^{4}He gas target were investigated. A prototype design was constructed, tested and concluded to be suitable.

Acknowledgements

I am particularly grateful to my advisor Dr. W. R. Falk for his guidance and close attention extended to me throughout my years of graduate study.

I would also like to thank fellow Ph.D. graduate student Keith Furutani for his moral support in using the VAX computers and other valuable suggestions.

Also, I would like to extend gratitude to technician G. Roy for his kindness in helping me to perform the pressure tests to the target.

Contents

1 Introduction 1

2 Formalism of Recoil Polarization Observables and Measurement Techniques 5

2.1 Basic Formalism 5

2.1.1 Density Matrix and Statistical Tensors 5

2.1.2 The Angular Correlation Function 7

2.1.3 Decay Mechanism 8

2.1.4 Symmetries 10

2.2 Experimental Technique and Tensor Extraction Method 11

2.3 Sequential Decay Model 14

2.4 The $^4\mathrm{He}(\vec{\mathrm{p}},\pi^+)^5\mathrm{He}(\mathrm{g.s.},\frac{3}{2}^-) \rightarrow \mathrm{n}+\alpha$ Correlation Experiment . . . 16

2.5 Theoretical Predictions of ^{5}He Polarization 19

3 The Monte Carlo Simulation Process 28

3.1 The General Geometry 28

3.2 Event Generation Process 32

3.2.1 Proton 32

3.2.2 Pion (π^+) 34

3.2.3 α−particle 37

3.3 Simulation Subroutines 40

3.3.1 COTRAN and Some Analytical Geometry 40

3.3.2 Dispersion-Matched Beam and Phase Space Ellipse 42

3.3.3 The Energy Loss 46
3.3.4 Multiple Scattering 50
3.3.5 Kinematics 53
3.3.6 The ^{5}He g.s. Excitation Function 57
3.4 The Simulation Results for Individual Harmonic Functions 58
3.5 Simulated Experimental Data (SED) 60

4 Event Reconstruction and Data Analysis Simulation 65
4.1 Event Target Reconstruction 65
4.1.1 The Reconstruction Process 66
4.1.2 Reconstruction Results 68
4.2 Data Analysis Simulation 72
4.2.1 Event Number Normalization 72
4.2.2 Tensor Extraction Method 73
4.2.3 Record Arrays for SIFDs and SCFD 77
4.2.4 Fitting Results, Goodness of Fit and Errors 78
4.3 Alternate Reference Frames 89
4.4 An Alternative Arrangement of the Experiment 93

5 The ^{4}He Gas Target Design and the Pressure Test 98
5.1 Physical Considerations of the Target Design 98
5.1.1 ^{4}He Gas Target 99
5.1.2 Target Wall 100
5.2 Target Construction 101
5.3 Target Pressure Tests 104
5.3.1 Rupture Pressure 105
5.3.2 Leak Tightness 106

6 Conclusion 108

Bibliography 110

Appendices 113

A Reference Frames and Rotations 113

B Additional Geometries 116

C Some Short Notations in the Text 118

D TRIUMF DASS/SASP and Beam Line 4B Specifications 119

E Havar 121

List of Figures

2.1 Schematic of Correlation Measurement for $A(a,b)B_{\rightarrow Y+z}$ 12

2.2 The Process of Extracting the Polarization Tensors 15

2.3 Velocity diagram for the sequential decay reaction $A(a,b)B_{\rightarrow Y+z}$. 16

2.4 ^{5}He Energy Level Diagram 17

2.5 The Typical Pion Spectrum (Counting Versus $n+\alpha$ Excitation Energy) Observed in the $^4\mathrm{He}(\vec{\mathrm{p}},\pi^+)^5\mathrm{He}$ Reaction (TRIUMF E564) 18

2.6 A schematic of the TRIUMF DASS/SASP facilities 20

2.7 The Differential Cross Section and Analyzing Power of $^4\mathrm{He}(\vec{\mathrm{p}},\pi^+)^5\mathrm{He}$ 22

2.8 Angular Distribution of ^{5}He Tensor Polarization in $^4\mathrm{He}(\vec{\mathrm{p}},\pi^+)^5\mathrm{He}$ at $T_p = 240MeV$ (Re-solid line, Im-open box) 24

2.9 Angular Distribution of ^{5}He Tensor Polarization in $^4\mathrm{He}(\vec{\mathrm{p}},\pi^+)^5\mathrm{He}$ at $T_p = 300MeV$ (Re-solid line, Im-open box) 25

2.10 Angular Distribution of ^{5}He Tensor Polarization in $^4\mathrm{He}(\vec{\mathrm{p}},\pi^+)^5\mathrm{He}$ at $T_p = 400MeV$ (Re-solid line, Im-open box) 26

2.11 Angular Distribution of ^{5}He Tensor Polarization in $^4\mathrm{He}(\vec{\mathrm{p}},\pi^+)^5\mathrm{He}$ at $T_p = 500MeV$ (Re-solid line, Im-open box) 27

3.1 The General Geometry 30

3.2 The Schematic of Constructing an Event 33

3.3 The Geometric Approximation of π^+ Multiple Scattering 36

3.4 The Effective (a) Horizontal and (b) Vertical Acceptance of π^+ Detector for the Reaction Point o. (c) The Full Acceptance (Shadowed Area) 38

3.5 The Geometry of COTRAN Transformation 41
3.6 The (a) Energy Dispersion and (b) Position Dispersion of the Proton Beam at $T_p = 400MeV$ Generated in the Monte-Carlo Simulation 44
3.7 The Schematic View of Phase Space Effect 44
3.8 The Horizontal Ellipse Generated in the Monte-Carlo Simulation . 45
3.9 The Landau Universal Distribution 48
3.10 The α and π^+ Energy Loss Distribution in both Target Gas and Cell Wall in the Simulation Process 51
3.11 The α and π^+ multiple scattering distribution in both the target gas and cell wall in the simulation process. The vertical scale shows the number of events scattered at an angle θ. 54
3.12 The Velocity Diagram of the Kinematics 56
3.13 Kinematics for $T_P = 400\ MeV$ (The Exci. Energy of ^{5}He is 0.893 MeV in the calculation of T_π, $T_{^5\mathrm{He}}$, $\theta_{^5\mathrm{He}}$ and T_α). 57
3.14 ^{5}He g.s. Excitation Energy relating $n + \alpha$ (a) The depicted analytical distribution and (b) Generated distribution in the simulation process 59
3.15 The π^+ and ^{5}He Energy Distributions in the Simulation Process . 59
3.16 α Energy Spectrum and its Position Distribution (Recorded in $o_{\alpha d}x_{\alpha d}y_{\alpha d}$ frame shown in Fig. 3.1) for Each Harmonic Functions Listed in Table 3.2 (In Transverse Frame). (a):W_0, (b):$W_1(+)$, (c):$W_1(-)$. 61
3.17 Contin. of Fig 3.16. (d):$W_2(+)$, (e):$W_2(-)$, (f):$W_3(+)$, (g):$W_3(-)$. 62
3.18 The sliced view of the acceptable *volume* of t_{20}, $Re(t_{22})$ and $Im(t_{22})$ 63
3.19 *Simulated Experimental Data* (a) α Energy spectrum (b) α position distribution for $(t_{20}, Re(t_{22}), Im(t_{22}))$ =(-0.2,-0.6,0.2) 64

4.1 The schematic of the target reconstruction (top view) 67
4.2 Event reconstruction distributions (left) and original distributions (right) for individual harmonic functions. (a): W_0, (b): $W_1(+)$, (c): $W_1(-)$ 69

4.3 Continuation of Fig 4.2 (d): $W_2(+)$, (e): $W_2(-)$, (f): $W_3(+)$, (g): $W_3(-)$ 70
4.4 Reconstruction distributions for (a) T_p, (b) $T_{^5\mathrm{He}}$ and (c) ^{5}He g.s. Exci. Energy 71
4.5 (a)Event reconstruction distribution of the SED and (b)the original $W(\theta, \phi)$ distribution at $(t_{20}, Re(t_{22}), Im(t_{22})) = (-0.2, -0.6, 0.2)$ . . 71
4.6 Example of Event counts normalization in 1 dimension 73
4.7 (a) The *pure mathematical* (ie. no instrumental effect) distribution of the correlation function (b) The SCFD, both at $(t_{20}, Re(t_{22}), Im(t_{22}))$ = (-0.2,-0.6,0.2) 79
4.8 The distributions of (a): the SCFD; (b) the fitted data recorded in a 16×14 array 86
4.9 The distributions of (a): the SCFD; (b) the fitted data; recorded in a 32×18 array 87
4.10 The distributions of (a): the SCFD; (b) the fitted data; recorded in a 8×12 array 88
4.11 The Block Diagram of Tensor Extractions in the Alternate Frames 92
4.12 The distributions of (a): the SCFD; (b) the fitted data; recorded in a 16×14 array in helicity frame 94
4.13 Event target reconstruction distributions for various PSD arrays with element sizes: (a)$1.0 \times 1.0 cm^2$, (b) $2.0 \times 2.0 cm^2$, (c) $3.0 \times 3.0 cm^2$, (d) $6.0 \times 6.0 cm^2$. 96

5.1 The Schematic of the Stress Calculation 100
5.2 The drawing of the target in (a): the side view and (b): the top view. units: in , ^4He gas inlet , ^4He gas , liquid N_2 102
5.3 The prototype of the target: (a) a taken apart view, (b) an intact target. 103
5.4 A practical arrangement of the reaction geometry (top view) . . . 104
5.5 The Schematic View of the Target Test 105

List of Tables

3.1 Some Simulation Parameters 31

3.2 The Individual Harmonic Functions in the Correlation Function $W(\theta, \phi)$ 39

3.3 The Moliere Function 52

3.4 Maximum Values of the Correlation Functions 63

4.1 Absolute Probability Integration of the Individual Harmonic Functions 74

4.2 Five Record Arrays 80

4.3 Fitting Results for full α acceptance (5 Counts, 5 Arrays), to be continued 81

4.4 The example of SIFDs counts cancellation (full α acceptance, record array 16×14) 83

4.5 The example of the fitting results (full α acceptance, SCFD counts 37008) 83

4.6 Example of the covariant error matrix, SCFD counts 37008, Record Array 16×14 84

4.7 Tensors extracted by fitting SCFD with the pure mathematical individual distributions 85

4.8 The SIFDs Counts (Limited α Acceptance, Record Array 16×14) 89

4.9 Fitting Results (Limited α Acceptance, SCFD counts 36852) . . . 89

4.10 Fitting Results for limited α acceptance (3 Counts, 5 Arrays) . . . 90

4.11 The fitted Tensors in Helicity Frame 91

4.12 Tensor Rotations from Transverse to Helicity Frame 93
4.13 Fitting Results (4 Element Sizes of PSD, 4 Record Arrays, SCFD counts 8737) 97

5.1 Target rupture tests 105
5.2 The long term leak test results 106

A.1 $d^2_{M',M}(\beta)$ 114

Chapter 1

Introduction

The exclusive (p, π^+) reaction on nuclei has been extensively studied in the past 20 years[1]. During the early phase of this period, interest was motivated largely by the hope that exclusive (p, π^+) reactions would become a useful spectroscopic tool for obtaining the new information on nuclear structure, particularly on the high momentum components of nuclear wave functions. Most experiments were performed near threshold with medium heavy target nuclei($A > 7$). However, a key problem complicating the study is the interplay between the reaction mechanism and the nuclear structure. It is hard to disentangle the uncertainties in the nuclear structure from others related with the reaction mechanism such as the relative importance of one step and two step processes. The one step process is the pionic stripping process based on an analogy with another high momentum transfer process, the (d, p) reaction. This simplest possible model of the (p, π^+) reaction is far from satisfactorily explaining the experimental data.

Therefore, systematic studies of a large number of cases will likely be necessary to gain a full understanding of the (p, π^+) reaction mechanisms which, in addition to the one step process, should also include two-nucleon or higher order processes.

Systematic measurement of the energy dependence of the (p, π^+) differential cross sections was the most commonly made measurement. Indeed the shape of the angular distributions for most nuclei depends strongly upon the nuclear states

selected.

In the past 15 years, with the advent of high intensity polarized proton beams, data for analyzing powers in these reactions has become a powerful new observable for the understanding of the pion production mechanism. The similarities of the angular distributions of the analyzing powers for exclusive $A(p,\pi^+)B$ reactions and the $pp \rightarrow d\pi^+$ reaction have been reported numerous times[2,3]. Korkmaz et al[4] also observed that the analyzing powers in the continuum for $^{13}C(p,\pi^+)X$ reaction is very similar to that of the $pp \rightarrow d\pi^+$ reaction.

The study of the (p,π^+) reaction mechanism is very important in the Δ_{1232} resonance region using very light nuclei because the latter are fairly well understood and have simple structures. In this energy region, signatures of the Δ_{1232} resonance via the $NN \rightarrow NN\pi^+$ reaction, if present, should be the least ambiguous. This should make the separation of nuclear structure effects from those of reaction mechanism more reliable.

With the objective of obtaining such information on light nuclei we have, during the past two years, performed two experiments, ^{3}He(p,π^+)^{4}He (TRIUMF E413) and ^{4}He($\vec{\text{p}}$,π^+)^{5}He (TRIUMF E564) [5], to measure the differential cross sections and analyzing power as a function of angle and incident proton energy.

It is well known that analyzing power data are frequently more useful to the understanding of nuclear reaction mechanisms than are the differential cross sections. This is also true of the intermediate energy (p,π^+) reaction. The analyzing power measurements we performed plus the data of some other (p,π^+) reactions[6] in the past few years indicate that there might be a substantial spin dependence in the Δ_{1232} resonance region. If the spin dependence is connected to the reaction mechanism rather than to simple initial and final state interactions, then in addition to the analyzing power, the measurement of the polarization of the recoil nucleus B might be an important higher order observable which could provide additional information to clarify the reaction mechanism.

The work discussed in this thesis is a detailed feasibility investigation for the

second stage of our TRIUMF Experiment E564, that would measure the $k = 2$ tensor polarization of the g.s. $J^\pi = \frac{3}{2}^-$ state of ^{5}He arising from the reaction. The additional spin information so obtained will be invaluable in sorting out the details of the reaction mechanisms. This polarization measurement relies on the breakup reaction $^5\mathrm{He}(\mathrm{g.s.}, \frac{3}{2}^-) \rightarrow \mathrm{n} + \alpha$. Angular correlation measurements between the π^+ and the α-particle permit determination of the statistical tensors describing the ^{5}He recoil nucleus polarization. For this particular decay, these tensors are restricted to t_{00}, t_{20}, and t_{22}[7].

The experimental capability of measurements of spin observables of nuclear scattering and reactions, such as analyzing powers, polarization of reaction products etc., with the use of polarized beams, targets and/or related methods, have provided nuclear physicists a useful tool to probe the subtleties of nuclear interactions. These experiments span a wide range of nuclear disciplines, from measurements probing complicated reaction mechanisms (such as our proposed measurement) to tests of fundamental symmetries (like Charge Symmetry Breaking experiments, etc).

Spin may be described as a property of a physical system (either one particle such as a proton, neutron, nucleus, etc., or a particle ensemble). The description of spin phenomena is always connected to a particular coordinate system. Although the choice is arbitrary, the preferred frame in nuclear physics for the study of two-body reactions A(a,b)B is that of the *Madison convention*[8] where the y-axis is taken perpendicular to the reaction plane and the z-axis along the incident beam direction. Later we will refer to this frame as the *Beam Helicity Frame.* In our work, for reasons of simplicity in description of the recoil breakup distributions, the preferred frame is chosen to be the *Recoil Transverse* frame[7] with z-axis normal to the reaction plane and x-axis along the direction of the recoil nucleus.

Possible experiments involving spin fall into five broad categories[10]:

(a) $\mathrm{A}(\mathrm{a}, \vec{\mathrm{b}})\mathrm{B}$ or $\mathrm{A}(\mathrm{a}, \mathrm{b})\vec{\mathrm{B}}$ Polarization measurement

(b) $\mathrm{A}(\vec{\mathrm{a}}, \mathrm{b})\mathrm{B}$ or $\vec{\mathrm{A}}(\mathrm{a}, \mathrm{b})\mathrm{B}$ Analysing Power measurement

(c) $A(\vec{a}, \vec{b})B$ or $A(\vec{a}, b)\vec{B}$ Polarization transfer

(d) $\vec{A}(\vec{a}, b)B$ Spin correlation(initial state)

(e) $A(a, \vec{B})\vec{b}$ Spin correlation(final state)

Our proposed experiment will employ a polarized proton beam and therefore the measurement falls under category (c).

Chapter 2

Formalism of Recoil Polarization Observables and Measurement Techniques

The following sections will give a short introduction to the treatment of polarization observables and the experimental techniques used to measure correlated sequential decay distributions of the recoiling nucleus produced in a nuclear reaction. The discussion will also be related to the $^4\mathrm{He}(\vec{\mathrm{p}},\pi^+)^5\mathrm{He}(\mathrm{g.s.},\frac{3}{2}^-)$ Reaction.

2.1 Basic Formalism

The description of this topic follows that given by Simonius[7].

2.1.1 Density Matrix and Statistical Tensors

The underlying motivation for measuring polarization effects in nuclear reactions is that they allow the study of coherence effects among the elements of the transition matrix (transition amplitudes) describing the process. In a two-body nuclear reaction of the form $A(a,b)B$, the spin dependence of the observables may be characterized by the transition matrix denoted by $T^{m_b m_B}_{m_a m_A}$. The elements of the

transition matrix give the amplitude for the transition from the initial state, whose constituents have spin projections (m_a, m_A) to the final state with spin projections (m_b, m_B). One may construct the density matrix describing the state of the recoil nucleus B from the transition amplitudes as follows:

$$\rho_{m_B m_{B'}} = \sigma(\theta)^{-1} \sum_{m_a, m_A, m_b} T^{m_b m_B} T^{m_b m_{B'} *}_{m_a m_A}, \tag{2.1}$$

where $\sigma(\theta)$ is the differential cross section which ensures that $\mathrm{Tr}(\rho) = 1$. Indeed, ρ contains the measurable information, since for any hermitian operator O of recoil nucleus B the expectation value is

$$< O >= Tr(\rho O). \tag{2.2}$$

Although the density matrix has an intuitive interpretation, its transformation to an irreducible tensor representation facilitates application of parity and rotational symmetries. The transformation is given by:

$$t_{kq} = \hat{s} \sum_{m_B m_{B'}} (-1)^{s-m_B} < s, m_{B'}, s, -m_B | kq > \rho_{m_B m_{B'}}, \tag{2.3}$$

with the inverse

$$\rho_{m_B, m_{B'}} = \hat{s}^{-1} \sum_{k,q} (-1)^{s-m_B} < s, m_{B'}, s, -m_B | kq > t_{kq}, \tag{2.4}$$

where:

s is the spin of recoil nucleus B and $\hat{s} = \sqrt{2s+1}$,

m is the projection of s on some z-axis,

$< s, m_{B'}, s, -m_B | kq >$ is the Clebsch-Gordon coefficient,

t_{kq} is the irreducible statistical tensor of rank k, $0 \leq k \leq 2s$ with components $-k \leq q \leq k$ (along the same z-axis).

The density matrix is hermitian which leads to the following symmetry property of the statistical tensors:

$$t_{kq} = (-1)^q t^*_{k,-q}. \tag{2.5}$$

2.1.2 The Angular Correlation Function

The interactions governing the decay processes of the recoil nucleus are explicitly dependent upon the spin state of the nucleus. The polarization in space (ie. m-value) manifests itself in the spatial distribution of the break-up products following the decay. One may use measurements of such distributions (eg. the correlated decay distributions to be used in this work) to extract information concerning the spin state of the recoil nucleus. So, the spin dependent decay distribution is said to be used to *analyse* the spin of the nucleus before decay. That decay distribution may be represented by the expectation value of some hermitian operator H

$$< H >= Tr(\rho H) = \sum_{m_B m_{B'}} H_{m_B m_{B'}} \rho_{m_{B'} m_B}, \tag{2.6}$$

where $H_{m_B m_{B'}}$ is the decay interaction matrix element, as formulated in the following subsection §2.1.3. Inserting equation (2.4) into (2.6) yields:

$$< H >= \sum_{k,q} t_{kq} \sum_{m_B m_{B'}} \hat{s}^{-1}(-1)^{s-m_{B'}} < s, m_{B'}, s, -m_B | kq > H_{m_B m_{B'}} = \sum_{k,q} t_{kq} T^*_{kq}, \tag{2.7}$$

where

$$T^*_{kq} = \sum_{m_B m_{B'}} \hat{s}^{-1}(-1)^{s-m_{B'}} < s, m_{B'}, s, -m_B | kq > H_{m_B m_{B'}}, \tag{2.8}$$

is termed the analyzing power tensor of the polarization *analyzer* (here *analyzer* could be thought of as a *black box* with a counter in which one measures the decay distribution which depends on the polarization). The hermiticity of H also leads to the relations

$$T_{kq} = (-1)^q T^*_{k,-q}. \tag{2.9}$$

We could use the correlation function $W(\theta, \phi)$, which is the probability per unit solid angle for a decay into a given direction (θ, ϕ) in the rest frame, to represent $< H >$. ((θ, ϕ) is also the direction of measurement taken by the analyzer.) If an arbitrary direction in the rest frame is chosen as the Z-axis direction, then the *analyzer* exhibits axial symmetry only when taken along this direction , ie. only

$q = 0$ terms in T_{kq} describe this particular measurement. We therefore have:

$$W(0,\phi) = \sum_k t_{k0} T^*_{k0} = \sum_k t_{k0} A_k, \tag{2.10}$$

where we have set $T^*_{k0} = A_k$. By rotating the T^*_{k0} in the active sense(See Appendix A) with Euler angles $(\alpha, \beta, \gamma) = (\phi, \theta, 0)$, one may realize the measurement along (θ, ϕ), ie.

$$T^*_{kq}(\theta,\phi) = D^k_{q0}(\phi,\theta,0) A_k = \sqrt{\frac{4\pi}{2k+1}} Y^*_{kq}(\theta,\phi) A_k. \tag{2.11}$$

Therefore the T_{kq} could be factored into a spherical harmonic function (describing the spatial dependence of T_{kq}) and a real term containing information concerning the specific interaction that governs the decay.

In the end, in any particular reference frame the correlation function may be written as:

$$W(\theta,\phi) = \sum_{k,q} \sqrt{\frac{4\pi}{2k+1}} A_k t_{kq} Y^*_{kq}(\theta,\phi), \tag{2.12}$$

when decomposed into an explicit real valued form we have:

$$\mathrm{W}(\theta,\phi) = \sum_{\mathrm{k,q}} 2\mathrm{A_k}(-1)^{\mathrm{q}} \sqrt{\frac{(\mathrm{k-q})!}{(\mathrm{k+q})!}} \mathrm{P^q_k}(\cos\theta)(\mathrm{Re(t_{kq})}\cos(\mathrm{q}\phi) + \mathrm{Im(t_{kq})}\sin(\mathrm{q}\phi))(1-\delta_{\mathrm{q},0}). \tag{2.13}$$

2.1.3 Decay Mechanism

Evaluation of the radiation parameter A_k requires explicit knowledge of the decay mechanism. If the intermediate particle B is in a well defined state (ie., orbital and spin angular momentum), then the parity is conserved provided no significant weak interaction. So, applying the parity operation to the correlation function requires $W(\pi-\theta, \phi+\pi) = W(\theta,\phi)$ which leads to the requirement that k be even valued. This follows from the parity of the spherical harmonics $Y_{kq}(\pi-\theta, \phi+\pi) = (-1)^k Y_{kq}(\theta,\phi)$ and that t_{kq} is invariant under parity operation. Therefore it implies

$$A_k = 0 \qquad for \quad k = odd.$$

The decay B $\rightarrow$ Y + z is characterized by the decay transition amplitude[10]

$$T^{m_B}_{m_Y m_z} = < \vec{k}, m_Y, m_z | T | m_B >, \tag{2.14}$$

here $\vec{k}$ is the relative momentum of Y and z. The interaction matrix element is:

$$H_{m_B m_{B'}} = \sum_{m_Y m_z} T^{m_B}_{m_Y m_z} T^{m_{B'}}_{m_Y m_z}. \tag{2.15}$$

Now considering the distribution along the z-axis, the projection of orbital angular momentum $m_l = 0$ on this direction makes $m_B = m_Y + m_z$. So

$$W(0, \phi) = \sum_{m_B} \rho_{m_B m_B} \sum_{m_B = m_Y + m_z} |T^{m_B}_{m_Y m_z}|^2 = \sum_{m_B} \rho_{m_B m_B} C_{m_B}, \tag{2.16}$$

here $C_{m_B} = |F^{m_B}_{m_Y m_z}|^2$.

Substituting equation (2.4) under $m_{B'} = m_B$ into (2.16) and comparing it with (2.10), one find

$$A_k = \hat{s}^{-1} \sum_{m_B} (-1)^{s - m_B} < s, m_B, s, -m_B | k0 > C_{m_B}. \tag{2.17}$$

The overall normalization has to be chosen such that

$$A_0 = 1 \qquad or \qquad \sum_{M_B} C_{m_B} = \hat{s}^2 = 2s + 1, \tag{2.18}$$

since $< s, m_B, s, -m_B | 00 > = (-1)^{s - m_B} \hat{s}^{-1}$. Note that the summation is only taken with $m_B = m_Y + m_z$ now.

Parity conservation together with a rotation of 180° around the y-axis implies

$$T^{m_B}_{m_Y m_z} = \pi_B \pi_Y \pi_z (-1)^{s - s_Y - s_z} T^{-m_B}_{-m_Y - m_z}, \tag{2.19}$$

where the various π's are the intrinsic parities. Equation (2.19) then yields $C_{m_B} = C_{-m_B}$.

In the end, we have

$$A_k = \delta_{k,even} \hat{s} \sum_{m_B \geq 0} (-1)^{s - m_B} < s, m_B, s, -m_B | k0 > C_{m_B} (2 - \delta_{m_B, 0}). \tag{2.20}$$

For $s \rightarrow \frac{1}{2} + 0$, $C_{\frac{1}{2}} = C_{-\frac{1}{2}} = \frac{(2s+1)}{2}$ only,

$$A_k = \delta_{k,even} \hat{s} (-1)^{s - \frac{1}{2}} < s, \frac{1}{2}, s, -\frac{1}{2} | k0 > . \tag{2.21}$$

In the decay ^{5}He$(\frac{3}{2}^-) \rightarrow$ n$(\frac{1}{2}^+) + \alpha(0^+)$, $A_0 = 1$ and $A_2 = -1$.

2.1.4 Symmetries

The discussion in the preceding section shows $A_k = 0$ for $k = odd$. Thus, information can only be obtained for t_{kq} with $k = even$ in any frame, even though the reaction itself may produce polarization in $k = odd$ tensors. Other symmetries related to the statistical tensors are discussed as follows:

Axial Symmetry

A state of nucleus B is axially symmetric around the z-axis if and only if $t_{kq} = 0$ for $q \neq 0$. ie. only t_{k0} survives if the z-axis is chosen in direction of the symmetry axis. In any other frame where the direction of symmetry axis is (θ_s, ϕ_s), the polarization tensor is:

$$t_{kq}(\theta_s, \phi_s) = D^{k*}_{q0}(\phi_s, \theta_s, 0) t_{k0} = \sqrt{\frac{4\pi}{2k+1}} Y_{kq}(\theta_s, \phi_s) t_{k0}. \tag{2.22}$$

Obviously, since t_{kq} and T_{kq} have the same form of representation (2.3) and (2.8), they follow the same form of transformation (2.22) and (2.11) based on axial symmetry. Note that (θ, ϕ) in (2.11) is the direction of measurement taken by the *analyzer* or the decay direction and therefore has nothing to do with (θ_s, ϕ_s) in (2.22), which only represents the direction of the polarization symmetry-axis.

Reflection Symmetry

Another kind of symmetry is called the reflection symmetry. A reflection in a plane may be represented by the parity operation (reflection on the origin), which leaves the t_{kq} invariant since parity is conserved, plus a rotation of 180° about an axis perpendicular ($\perp$) to the reaction plane. Then

if the y-axis is $\perp$ to the reaction plane

$$t_{kq} = (-1)^{k+q} t_{k,-q}, \tag{2.23}$$

and if the z-axis is $\perp$ to the reaction plane

$$t_{kq} = (-1)^{q} t_{kq}. \tag{2.24}$$

On considering these together with (2.5), we see that the t_{kq} are real if the y-axis is $\perp$ to the reaction plane, and complex if the z-axis is $\perp$ to the reaction plane. In the latter case, $t_{kq} = 0$ for $q = odd$. The frame we adhere to in this work is the transverse frame and therefore only tensors with k and q both even integers need to be considered. The analyzing power tensors T_{kq} follow the same reflection symmetries as do the t_{kq}.

In summarizing, applying (2.13), the correlation function for ^{5}He(g.s., $\frac{3}{2}^-$) $\rightarrow$ n + α in the transverse frame is:

$$\mathrm{W}(\theta,\phi) = \mathrm{t}_{00} - \frac{1}{2}(3\cos^2\theta - 1)\mathrm{t}_{20} - \sqrt{\frac{3}{2}}\mathrm{Re}(\mathrm{t}_{22})\sin^2\theta\cos 2\phi - \sqrt{\frac{3}{2}}\mathrm{Im}(\mathrm{t}_{22})\sin^2\theta\sin 2\phi. \tag{2.25}$$

The normalization is $t_{00} = 1$ and the overall normalization is $\int \mathrm{W}(\theta,\phi)\mathrm{d}\Omega = 4\pi$.

2.2 Experimental Technique and Tensor Extraction Method

Correlation experiments for the purpose of extracting polarization observables of the recoil nucleus arising from a two body reaction require the measurements of the spatial distribution of the decay products. Such measurements are carried out in coincidence with the light particle b being measured at a fixed angle θ_b. The kinematics of the reaction provide a fixed recoil direction in the scattering plane, about which the decay products distribute themselves according to the correlation function, from which the polarization observables may be extracted. Fig. 2.1 gives a schematic view of such a measurement. The breakup velocity in the laboratory frame is the summation of the recoil velocity in this frame with the breakup velocity in the recoil c.m. frame. In such a relationship, the correlation distribution in the laboratory then manifests itself in the energy and position of the decayed particle Y. In order to extract a complete set of polarization tensors it is normally necessary to take measurements in several planes, usually coplanar and non-coplanar measurements[11] with respect to the initial reaction plane.

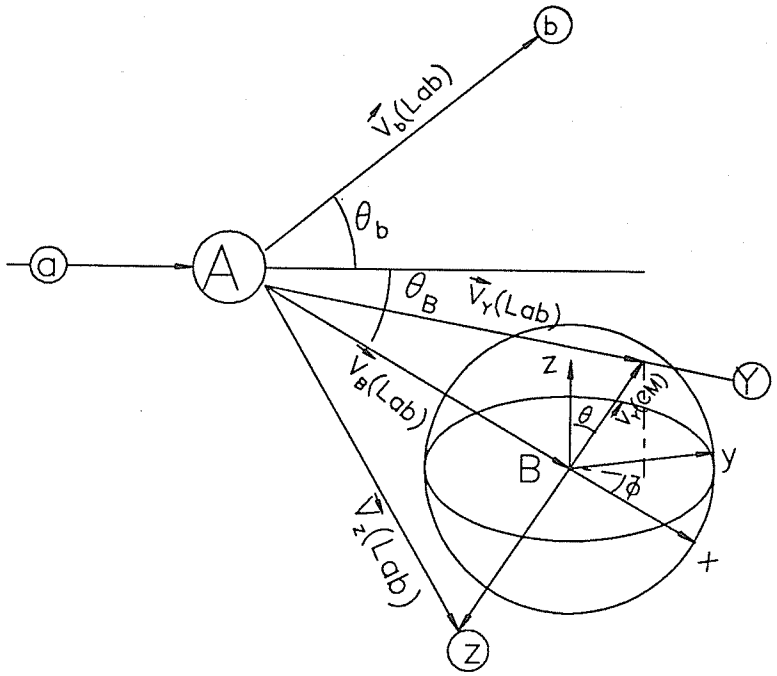

Figure 2.1: Schematic of Correlation Measurement for $A(a,b)B_{\rightarrow Y+z}$

The reaction and decay kinematics play a defining role in the viability of a correlation experiment, about which more detailed information can be found in Ref. [12] §1.2, where various experimental techniques are introduced for different kinds of reaction kinematics. We only recall one kind where both decay products possess considerable mass and consequently exhibit a fairly broad distribution in energy and space, allowing direct mapping of the lab recoil distributions into the recoil c.m. system to obtain the correlation distributions. Our proposed measurement for ^{5}He(g.s., $\frac{3}{2}^-$) $\rightarrow$ n + α is such a case.

A rectangular silicon surface barrier position sensitive detector (PSD), capable of $0.5mm$ spatial resolution and 50 KeV energy resolution, allows relatively economical measurements of the decay distributions in the laboratory in one plane at a time.

The experimental measurements for determining the ^{5}He polarization arising from the ^{4}He$(\vec{p},\pi^+)^5$He reaction would use a similar but somewhat more complicated technique. We would measure the full decay distributions of ^{5}He(g.s., $\frac{3}{2}^-$) $\rightarrow$ n + α in the laboratory for the α-particles with a large acceptance detector rather than just taking the measurements in one plane at a time. When the laboratory distributions are transformed back to the recoil c.m. system, the full angular correlation distribution can be mapped out.

The laboratory distributions corresponding to each harmonic function in the correlation function (2.25), associated with each individual tensor, are calculated in a Monte Carlo simulation, with all of the instrumental effects such as finite geometry, energy loss, multiple scattering etc. included in the calculation. Reconstruction of these individual *'laboratory'* distributions back to the recoil c.m. system yields the *Experimental-like* distributions for each harmonic function. These act as the base functions in fitting to the full correlation function in order to extract the tensors. The fitting procedure will apply the least-squares and the maximum-likelihood method. Full details of all these procedures are presented in §4.2.

Shown in Fig. 2.2 is a block diagram of the process, in which the two boxes within the dashed lines are designed for calculating a *Simulated Experimental Data* (SED, see §3.5 for detail) through the *Monte-Carlo Apparatus* for *Data Analysis Simulation* in Chapter 4.

2.3 Sequential Decay Model

Many 3-body break-up reactions proceed essentially via sequential decay processes: $A + a \rightarrow b + B \rightarrow b + Y + z$, where the unstable nucleus B is a resonance in the subsystem $Y - z$ which can be regarded as a quasi-bound intermediate resonant state. Under such an assumption and appropriate kinematical conditions, Heiss [13] developed a microscopic calculation of the differential cross-section for three-body breakup taking into account the dependence on the relative energy of $Y - z$.

According to Heiss, the three-particle sequential decay process is described in relation to two center of mass (c.m.) systems: The reaction c.m. system and the recoil c.m. system. The cross-section can be written (for a given angle θ_b^c) as:

$$\frac{d\sigma}{dT_{Y-z}d\Omega_{Y-z}d\Omega_b^c} = F(T_{Y-z})W(\theta_b^c, \Omega_{Y-z}). \tag{2.26}$$

W is the angular correlation function as defined in §2.1.2 in a model-independent way. $F(T_{Y-z})$ is the so called enhancement factor as defined and formulated in the microscopic calculation, which should reproduce the shape of the resonance of the recoil nucleus. Ω_b^c denotes the direction of the detected light particle b in the reaction c.m. system of $A(a,b)B$, or effectively, the direction of ^{5}He chosen for observing the breakup distribution (since $\theta_B^c = 180° - \theta_b^c$). Here T_{Y-z} and Ω_{Y-z} are the relative energy and the decay solid angle of the $Y - z$ subsystem in the recoil c.m. system. The diagram relating the two c.m. systems is shown in Fig. 2.3, where $OX_{BH}Y_{BH}Z_{BH}$ is the reaction c.m. system termed *Beam Helicity frame*, since Z_{BH}-axis is taken along the beam direction and, $OX_{Rc}Y_{Rc}Z_{Rc}$ is the *recoil c.m. transverse* frame, since Z_{Rc}-axis is perpendicular to the reaction plane.

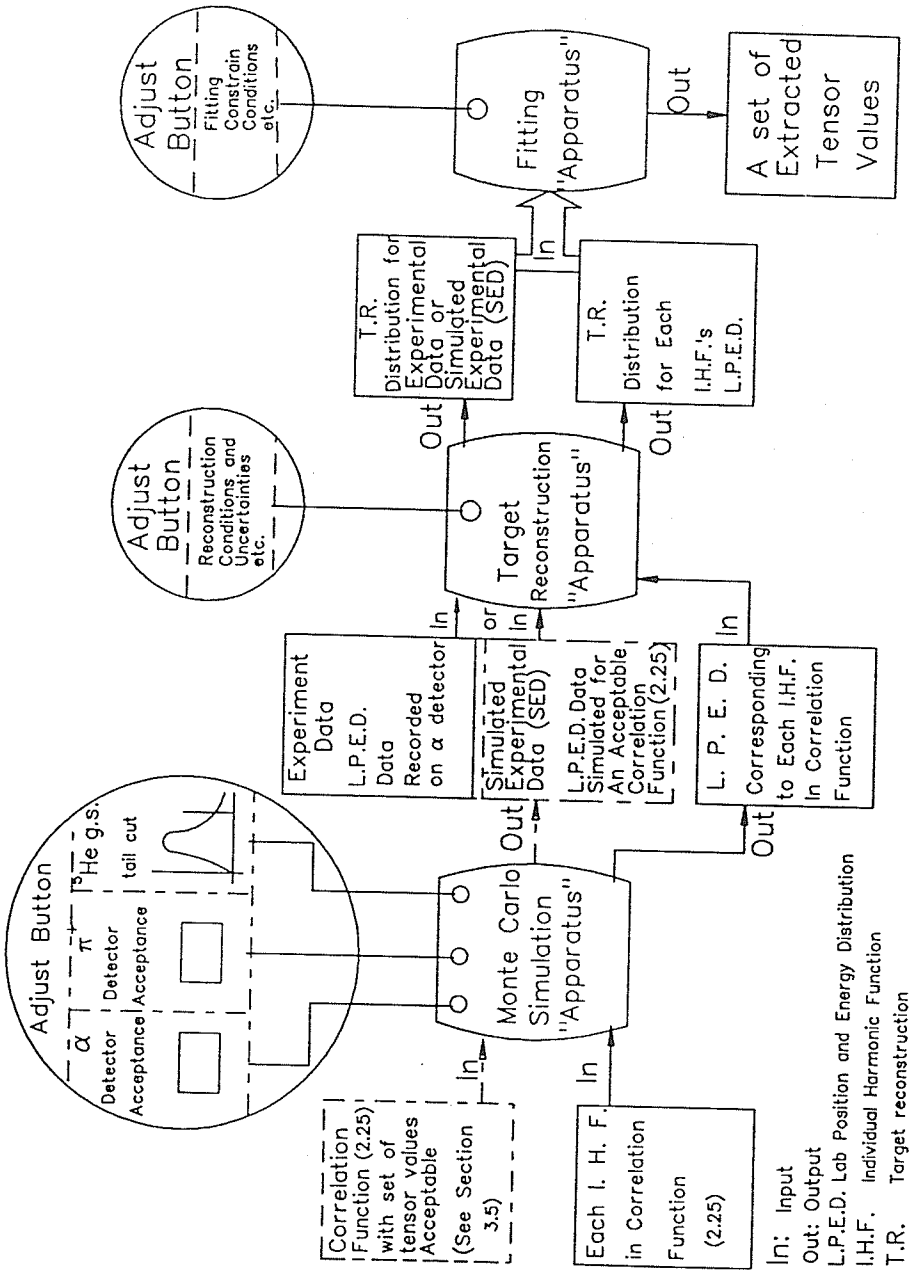

Figure 2.2: The Process of Extracting the Polarization Tensors

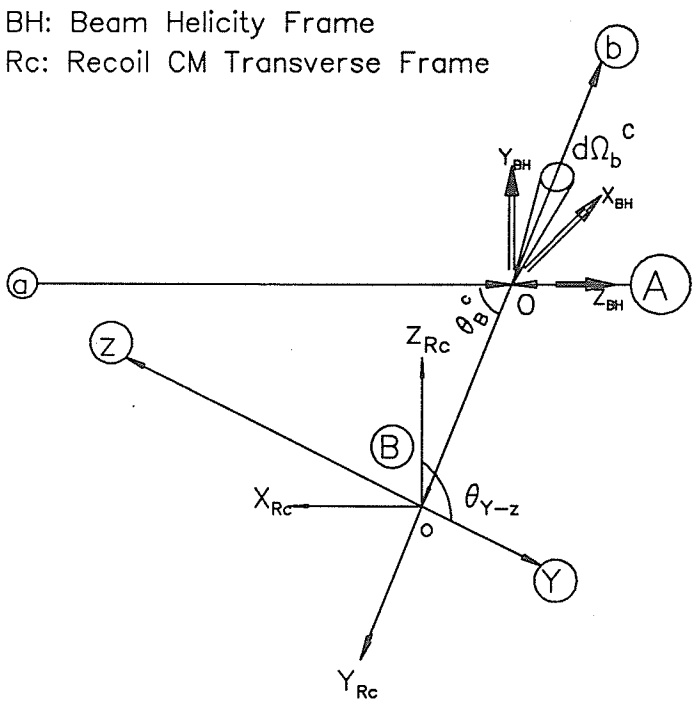

Figure 2.3: Velocity diagram for the sequential decay reaction $A(a,b)B_{\to Y+z}$

Note that $d\Omega_{Y-z} = d\Omega(\theta_{Y-z}, \phi_{Y-z})$ and $d\Omega_b^c = d\Omega(\theta_b^c, \phi_b^c)$.

Integration of (2.26) over the relative energy yields:

$$\frac{d\sigma}{d\Omega_{Y-z} d\Omega_b^c} = W(\theta_b^c, \Omega_{Y-z}) \int F(T_{Y-z}) dT_{Y-z} = W(\theta_b^c, \Omega_{Y-z}). \tag{2.27}$$

In some measurements [14,15], the differential cross sections were determined only for a certain interesting T_{Y-z} value. Then following (2.26) and fitting with least-squares method, one could extract the polarization tensors. In some others [16,17], the angular correlation function (2.27) itself was mapped over the width of the resonance. All these up to now were limited to measurements along a few planes only.

2.4 The $^4\mathrm{He}(\vec{\mathrm{p}}, \pi^+)^5\mathrm{He}(\mathrm{g.s.}, \frac{3}{2}^-) \to \mathrm{n} + \alpha$ Correlation Experiment

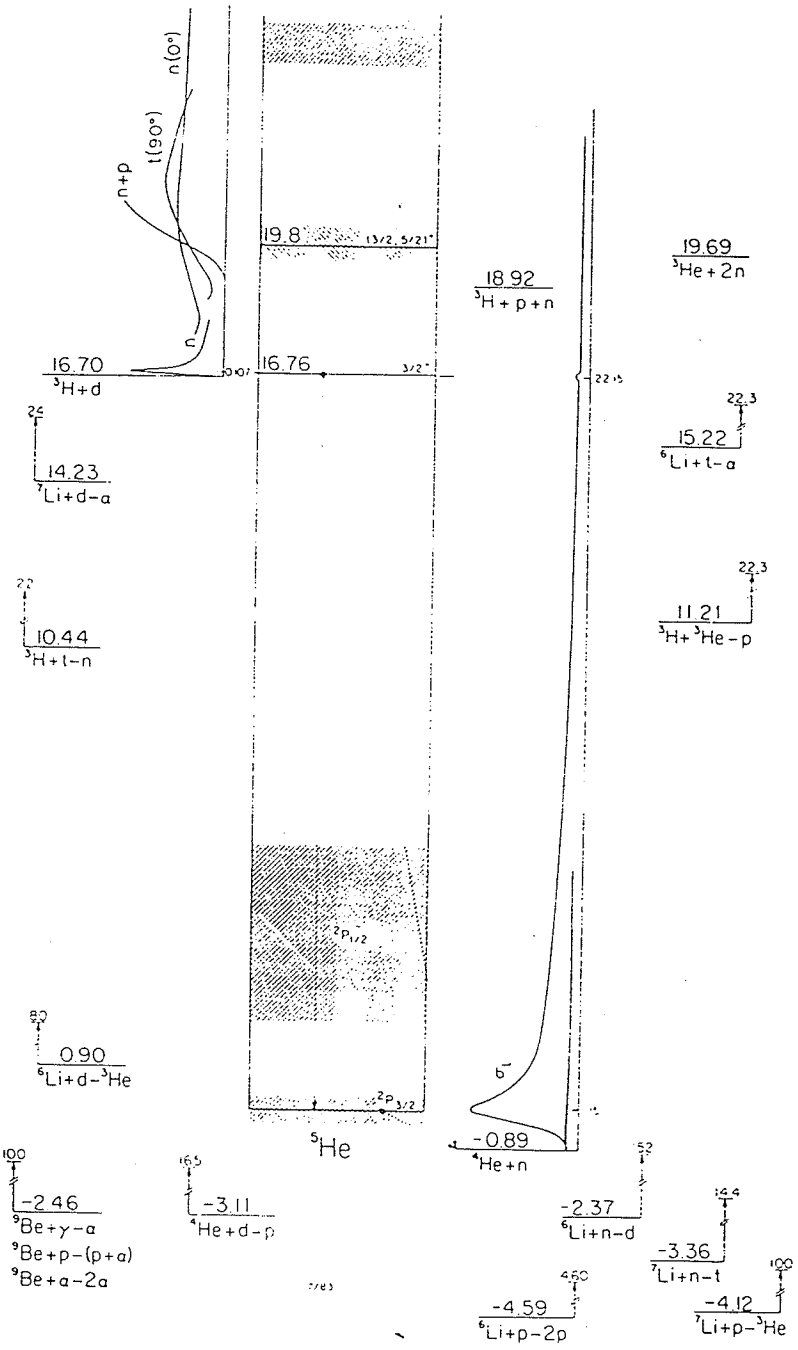

Figure 2.4: ^{5}He Energy Level Diagram

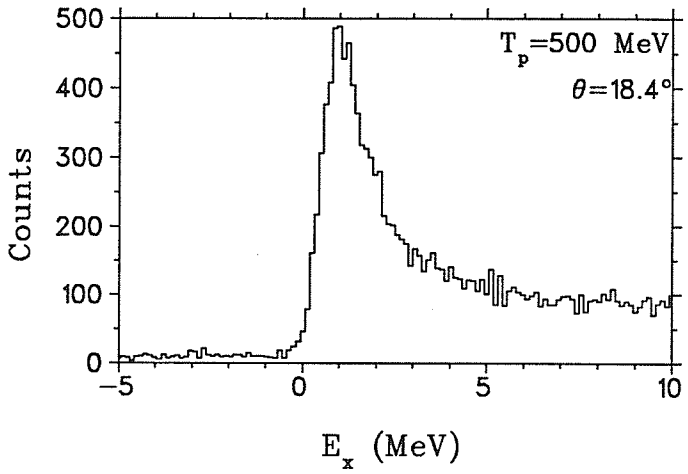

Figure 2.5: The Typical Pion Spectrum (Counting Versus n+α Excitation Energy) Observed in the ^{4}He$(\vec{p},\pi^+)^5$He Reaction (TRIUMF E564)

The ^{4}He$(\vec{p},\pi^+)^5$He(g.s., $\frac{3}{2}^-$) $\rightarrow$ n + α reaction is a typical sequential decay process, where the intermediate nuclear state exhibits a width of about 0.6 MeV. Experimentally, this width is helpful for mapping the correlation distribution in the recoil c.m. frame. In the Monte Carlo simulation for this reaction, we will map the excitation function or the resonance region of ^{5}He(g.s., $\frac{3}{2}^-$) in detail since we will measure the full angular correlation function.

Figure 2.4 is the energy level diagram of ^{5}He[18]. The g.s. $\frac{3}{2}^-$ state of ^{5}He is strongly excited in the ^{4}He$(\vec{p},\pi^+)^5$He reaction. The ^{5}He(g.s., $\frac{3}{2}^-$) decays to $n + \alpha$ (lifetime 2×10^{-22} s). The spatial angular momentum is L=1 only. The excitation function appears rather asymmetric with a fairly long tail on the high excitation energy side due to phase space effects. The width of the state is about $\Gamma = 0.60\ MeV$, and the resonance peak at an $n + \alpha$ excitation energy of 0.893 MeV. The most recent measurements of these values can be found in Ref. [19]. There is a very broad first excited state ($P_{1/2}$), with a position and width of approximately 4 MeV and 4 MeV respectively [the uncertainty in both

of these values is $\pm 1\ MeV$]. This state is not strongly excited compared to the $\frac{3}{2}^-$ ground state. No evidence for the $\frac{3}{2}^+$ state at 16.76 MeV excitation was observed in the pion spectra of the TRIUMF Experiment E564.

Figure 2.5 shows a typical pion spectrum observed in the $^4\mathrm{He}(\vec{p},\pi^+)^5\mathrm{He}$ reaction for E564. The counting distribution is graphed versus the ^{5}He excitation energy. During the experiment, typical counting rates of $\sim 4000/hr$ were observed from a target having thickness of $\sim 140 mg/cm^3$.

The second phase of the experiment will employ the TRIUMF Dual Arm/Second Arm Spectrometer (DASS/SASP) facility to make coincident measurements between the pion and α, with the Medium Resolution Spectrometer (MRS) for detecting π^+, and $SASP$, which has a relatively larger acceptance, for detecting the α. The MRS has been in service for many years, and SASP is currently being installed.

A schematic view of the facilities is shown in Fig 2.6, with the various spectrometer parameters tabulated in Appendix 4 (Table I for SASP and Table II for MRS respectively). Table III outlines the specifications of the beam line 4B which will be used.

Initially, the measurements proposed will cover an angular range of $\sim 30-120°$ at beam energies of 400, 500 MeV. The expected number of correlation events ($\pi^+\alpha$) to be recorded is $\sim$ 6000 minimum.

2.5 Theoretical Predictions of ^{5}He Polarization

Since our present knowledge of the exclusive $A(p,\pi^+)B$ reaction gives compelling evidence of the dominance of the underlying pp $\rightarrow$ dπ^+ process, numerous efforts have been made in the past to interpret nuclear pion production data in terms of the pp $\rightarrow$ dπ^+ reaction. H. Fearing[20], in his review of pion production, discussed this connection.

As a related approach, Falk and Furutani have developed a plane wave impulse

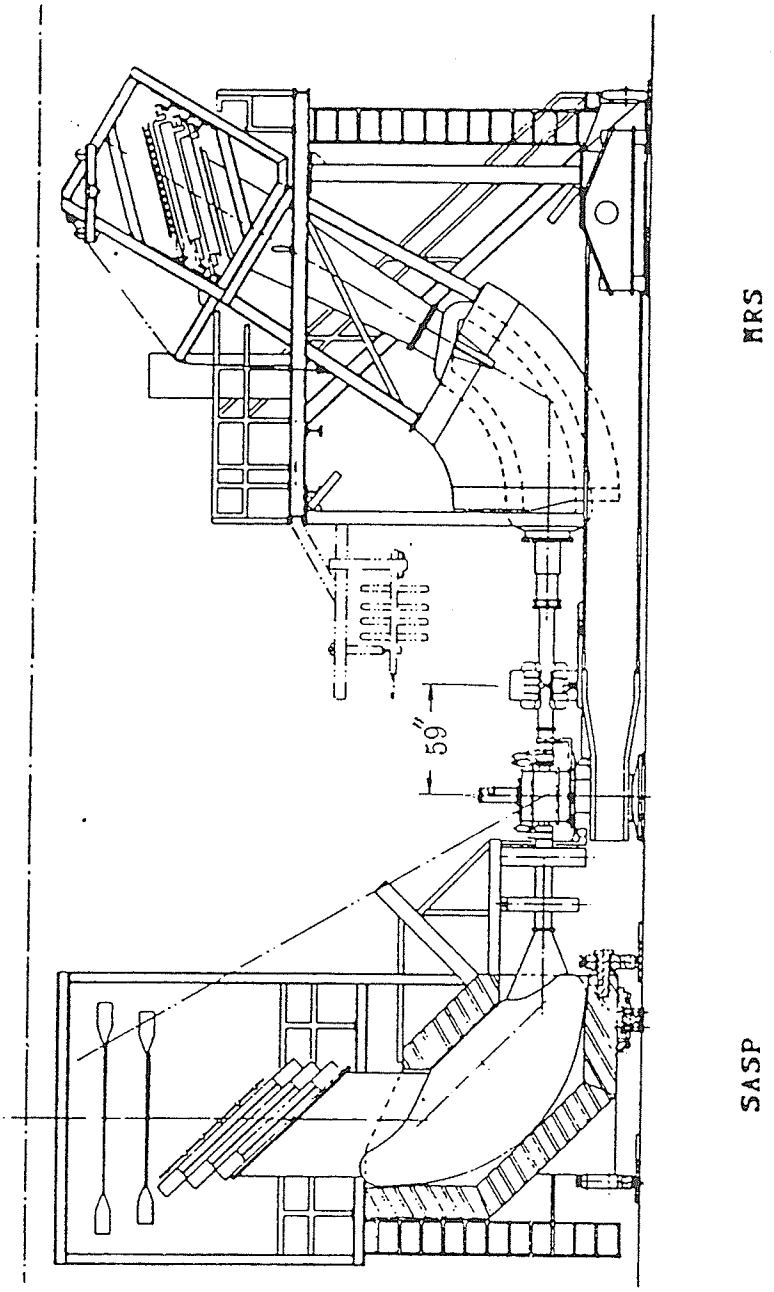

Figure 2.6: A schematic of the TRIUMF DASS/SASP facilities

model[21] in which the amplitudes for the A(p, π^+)A + 1 reaction are expressed in terms of the $pp \rightarrow d\pi^+$ spin-dependent amplitudes as a continuous function of energy. Various spin-dependent observables can be calculated with these amplitudes. The formulation incorporates the target proton and recaptured deuteron momentum distributions and the Pauli exclusion principle. Calculations with this phenomenological model are applied to ^{4}He($\vec{p}, \pi^+$)^{5}He and the resultant differential cross sections and analysing powers are shown in Fig. 2.7. Reasonable fits for the lowest two energies are obtained, but the quality of the fits, especially at 400 MeV, is not good. Since no other calculations are available for this reaction, the statistical tensors of recoil nucleus ^{5}He(g.s., $\frac{3}{2}^-$) were calculated from the amplitudes of the above model.

The calculation of the amplitudes for ^{4}He($\vec{p}, \pi^+$)^{5}He were carried out in the reaction c.m. frame $OX_{BH}Y_{BH}Z_{BH}$, or *Beam Helicity Frame*, as shown in Fig. 2.3. The various tensors in this frame are:

$$t_{00} = \rho_{\frac{3}{2},\frac{3}{2}} + \rho_{\frac{1}{2},\frac{1}{2}} + \rho_{-\frac{1}{2},-\frac{1}{2}} + \rho_{-\frac{3}{2},-\frac{3}{2}} = Tr(\rho), \tag{2.28}$$

$$t_{20} = \rho_{\frac{3}{2},\frac{3}{2}} - \rho_{\frac{1}{2},\frac{1}{2}} - \rho_{-\frac{1}{2},-\frac{1}{2}} + \rho_{-\frac{3}{2},-\frac{3}{2}}, \tag{2.29}$$

$$t_{21} = \sqrt{2}(-\rho_{\frac{1}{2},\frac{3}{2}} + \rho_{-\frac{3}{2},-\frac{1}{2}}), \tag{2.30}$$

$$t_{22} = \sqrt{2}(\rho_{-\frac{1}{2},\frac{3}{2}} + \rho_{-\frac{3}{2},\frac{1}{2}}). \tag{2.31}$$

In addition, (2.5) yields

$$t_{2,-1} = -t^*_{2,1}, \qquad t_{2,-2} = t^*_{2,2}.$$

The normalization imposed is $t_{00} = Tr(\rho) = 1$. The calculated values of these tensors are plotted versus c.m. scattering angles on the left side of Fig. 2.8 to Fig. 2.11 for the four beam energies respectively. From these figures one sees that only the real part of each tensor survives, consistent with the expected symmetry properties in the *Beam Helicity Frame*. Transforming these tensors with Euler angles $(\frac{\pi}{2}, \frac{\pi}{2}, \pi - \theta^c_{^5\mathrm{He}})$ to the recoil c.m. transverse frame $OX_{Rc}Y_{Rc}Z_{Rc}$ shown in Fig. 2.3, one should also find t_{21} and $t_{2,-1}$ vanishing due to these symmetries

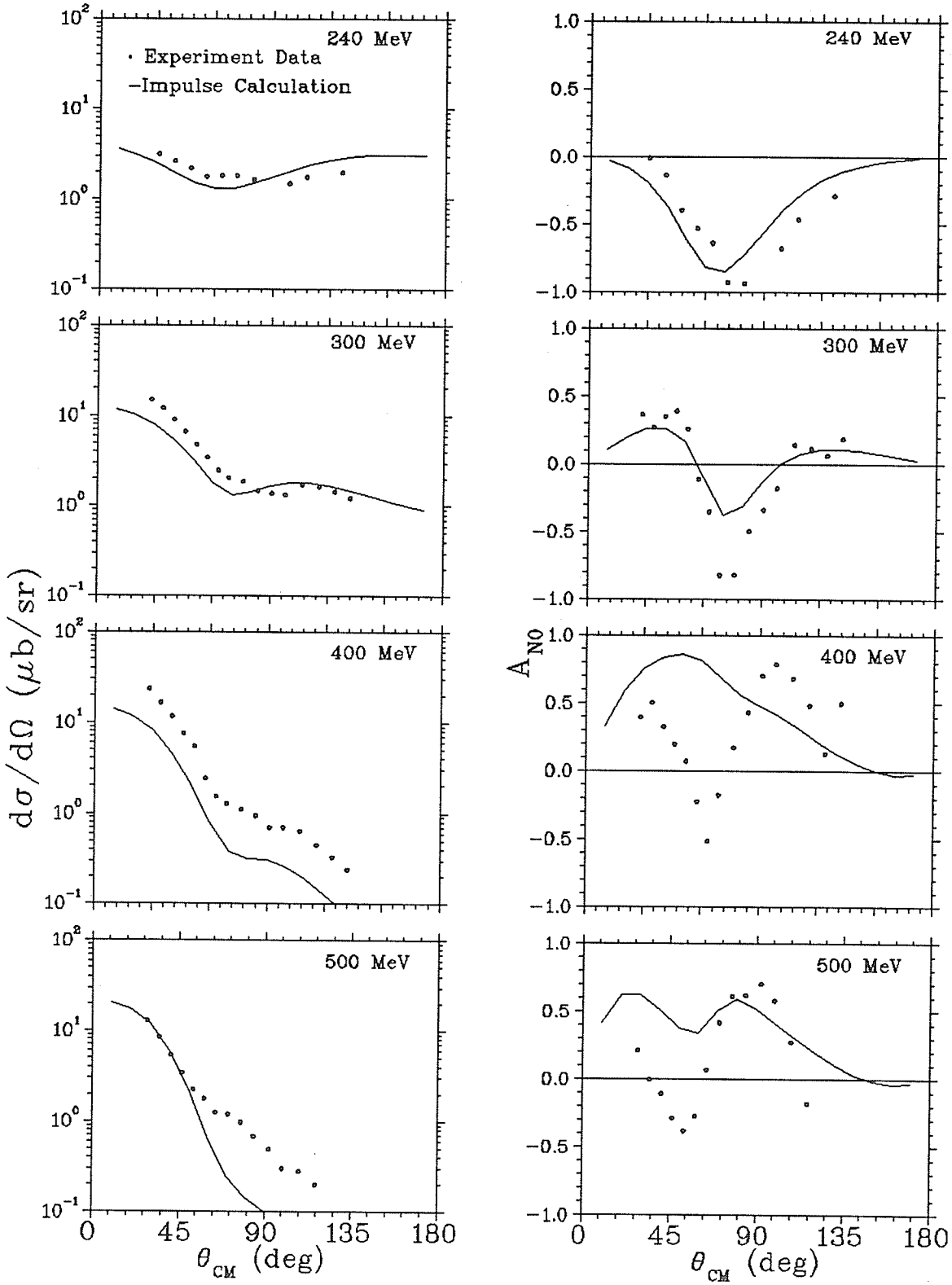

Figure 2.7: The Differential Cross Section and Analyzing Power of ^{4}He$(\vec{p}, \pi^+)^5$He

and t_{20} should be real in this case. The tensor distributions after the rotations are plotted on the right hand side of these figures. Appendix A provides more details about the implementations of these tensor rotations. In the experiment, one can chose various ^{5}He scattering angle $\theta^c_{^5\mathrm{He}}$s (in the reaction c.m. system) for observing the decay distributions.

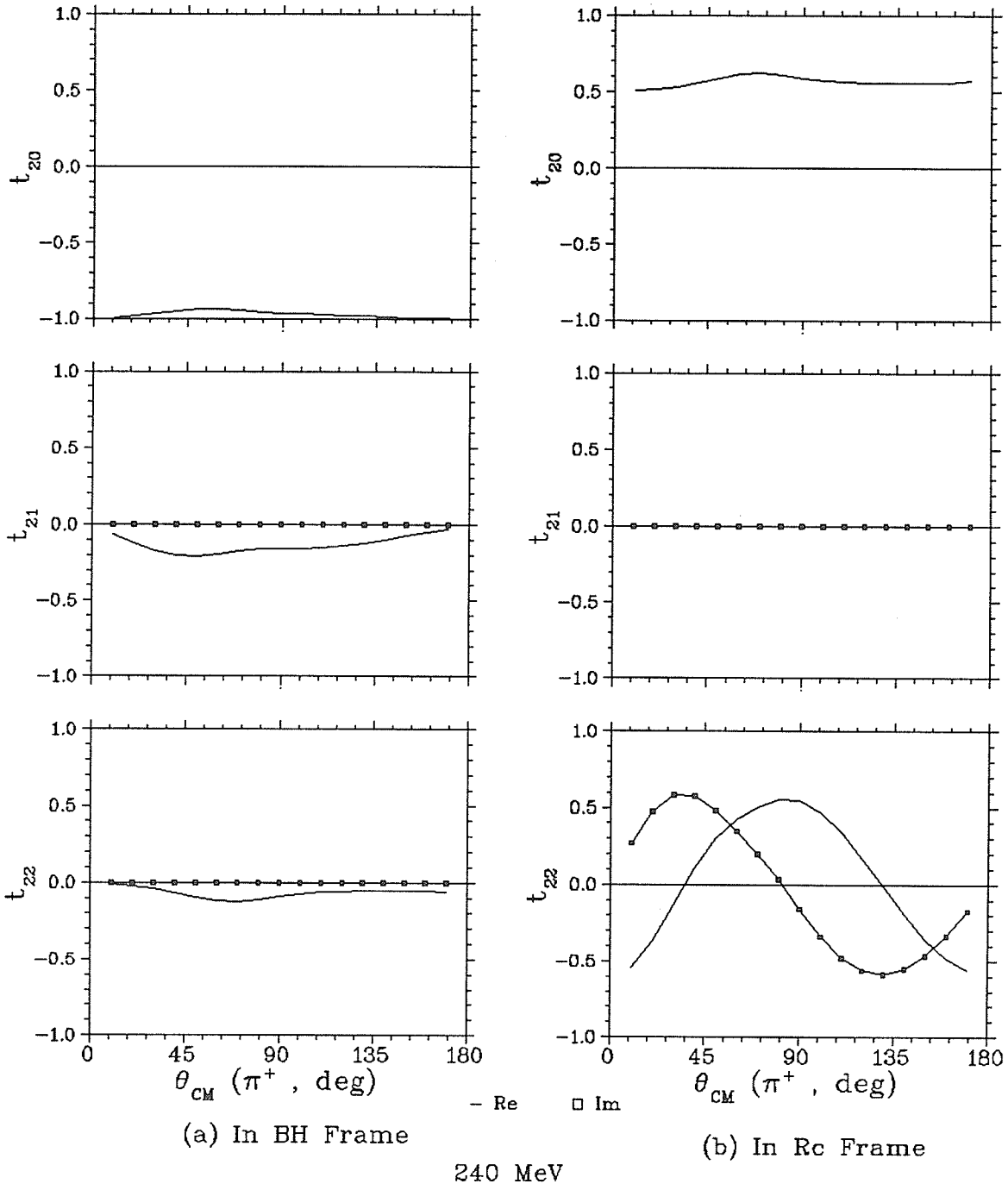

Figure 2.8: Angular Distribution of ^{5}He Tensor Polarization in $^4\mathrm{He}(\vec{\mathrm{p}}, \pi^+)^5\mathrm{He}$ at $T_p = 240MeV$ (Re-solid line, Im-open box)

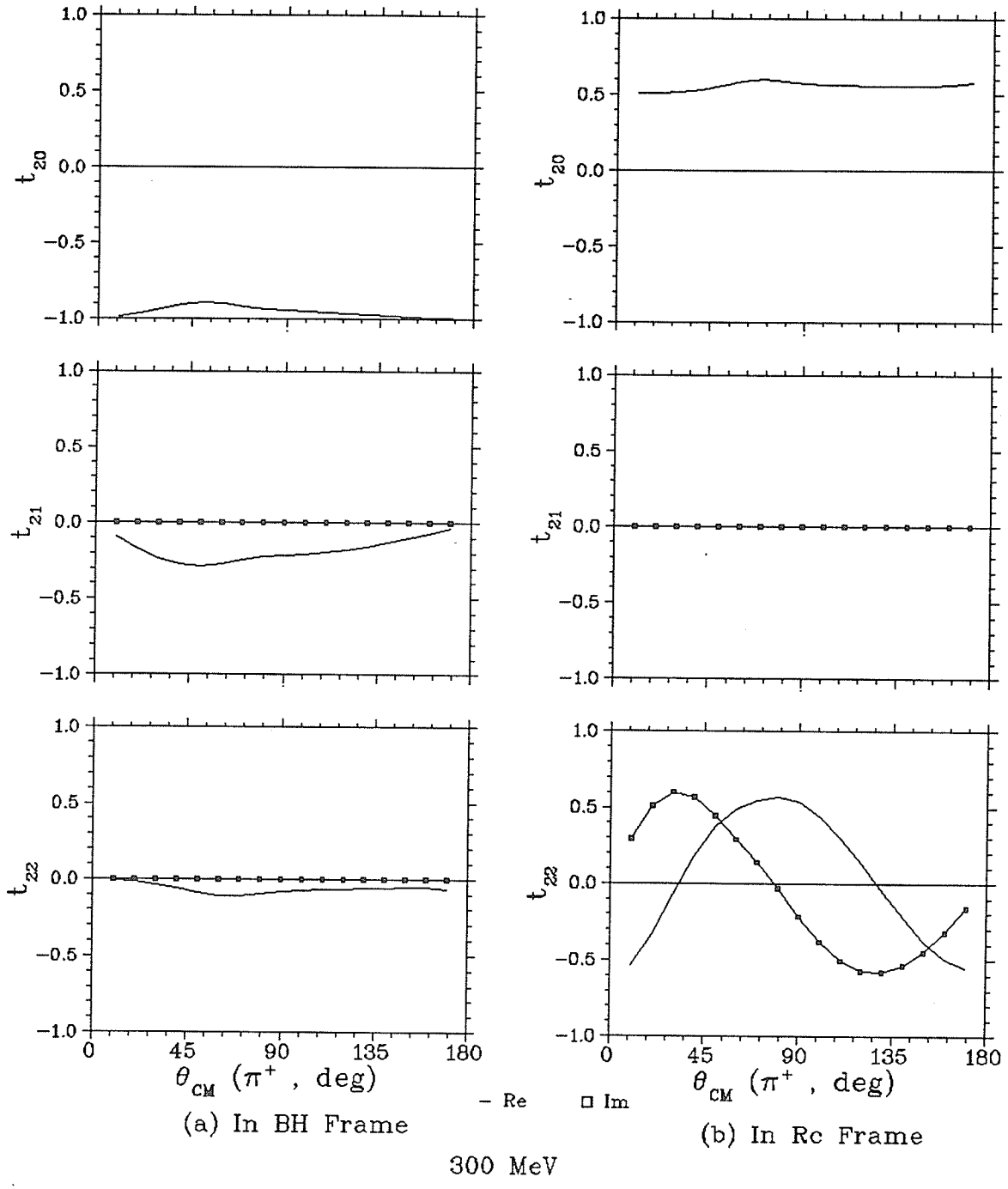

Figure 2.9: Angular Distribution of ^{5}He Tensor Polarization in $^4\mathrm{He}(\vec{\mathrm{p}},\pi^+)^5\mathrm{He}$ at $T_p = 300MeV$ (Re-solid line, Im-open box)

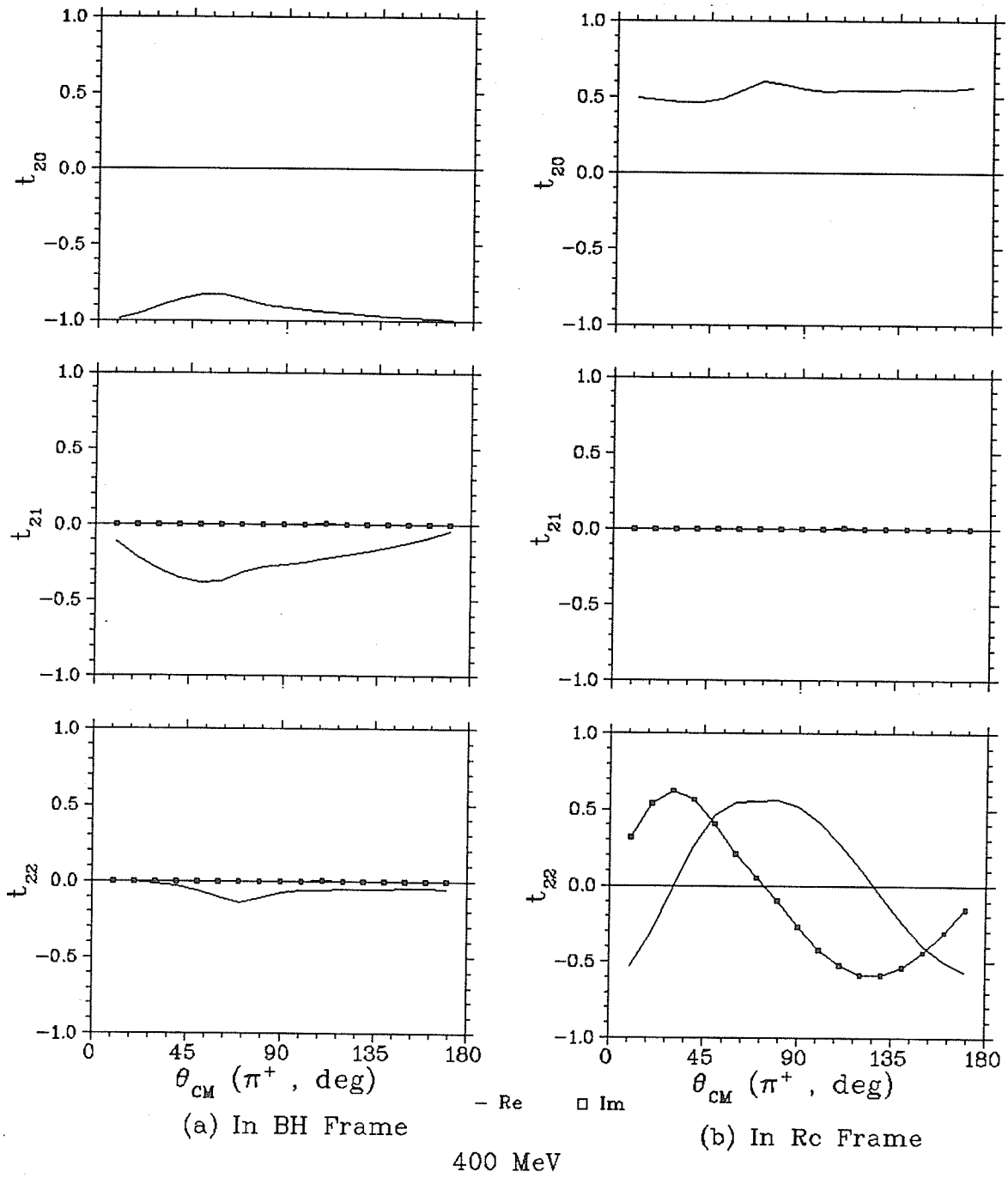

Figure 2.10: Angular Distribution of ^{5}He Tensor Polarization in $^4\mathrm{He}(\vec{\mathrm{p}},\pi^+)^5\mathrm{He}$ at $T_p = 400MeV$ (Re-solid line, Im-open box)

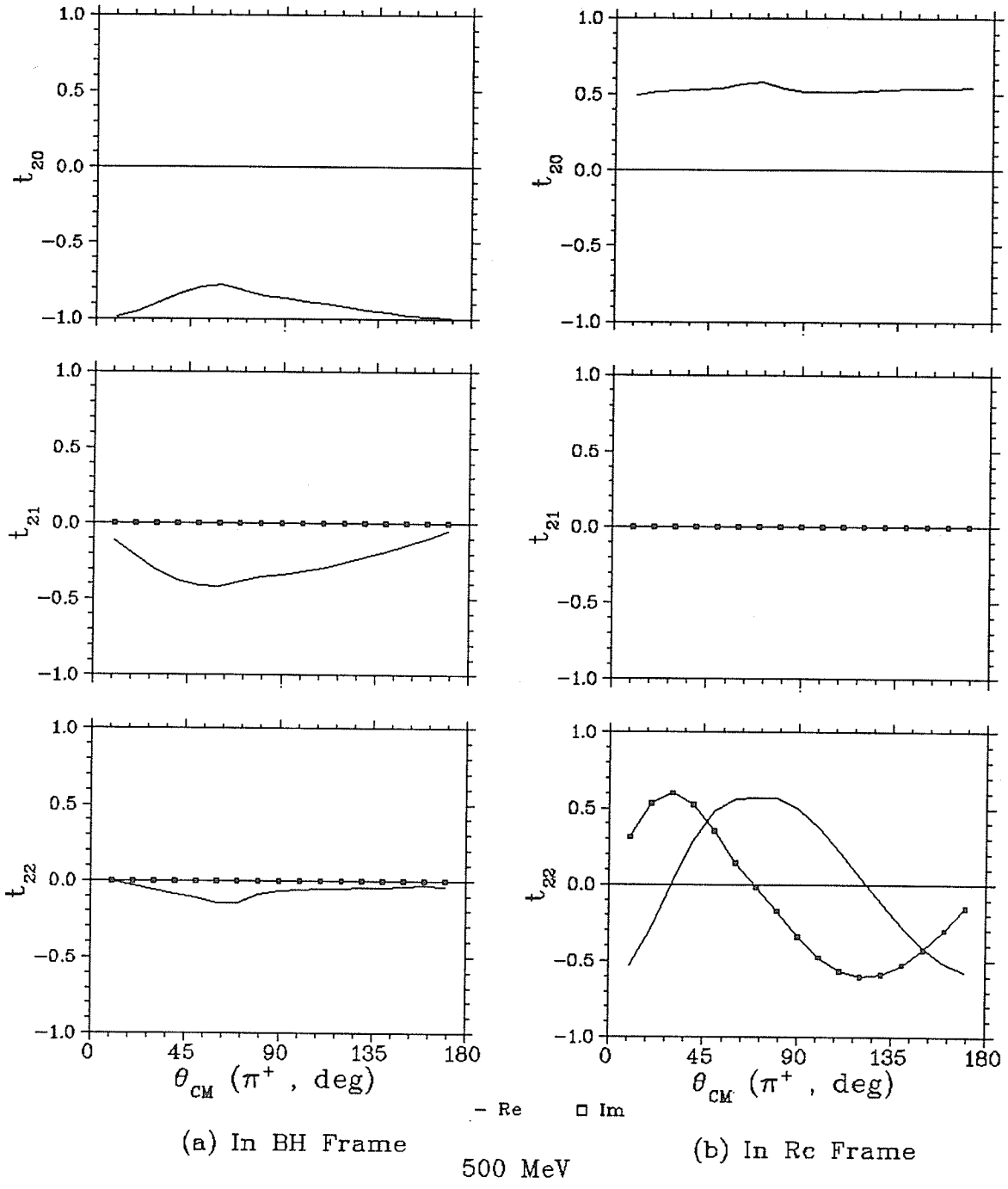

Figure 2.11: Angular Distribution of ^{5}He Tensor Polarization in $^4\mathrm{He}(\vec{\mathrm{p}},\pi^+)^5\mathrm{He}$ at $T_p = 500MeV$ (Re-solid line, Im-open box)

Chapter 3

The Monte Carlo Simulation Process

The proposed experiment has been outlined in §2.4. In this chapter, we will carry out in detail a Monte-Carlo simulation for one such proposed measurement.

The measurement will be made at a beam energy of 400 MeV so that the α-particles will have smaller energy loss and multiple scattering compared with that at a much lower beam energy. The MRS will be positioned at 60° forward to the beam for observing the pion. The ^5He recoils at 17.2° and breaks up to an α-partcle and a neutron in $\sim 10^{-22}$ sec. Located at the ^5He recoil direction, the SASP will be used to detect the α-particle, which has a breakup angle of $\leq 3°$ in laboratory. In such a setting, the pions have an energy of $\sim$ 185 MeV and the energies of α-particles range from 50 to 70 MeV.

Various instrumental parameters involved in the simulation are summarized in Table 3.1.

3.1 The General Geometry

Figure 3.1 is a schematic of the experimental layout for the pion and α particle correlation measurement. The target is a cylindrical cell filled with dilute ^{4}He

gas. Such a gas target is good for producing little energy loss and multiple scattering for α-particles. The Monte-Carlo is taken only as far as the entrances of the two spectrometers. The position and angle uncertainties of the pion are determined by the characteristics of the two sets of Front End Chambers (FEC) at the entrance of the MRS, and similarly the position uncertainty of the α-particle is determined by another FEC at the entrance of the SASP. (Alternatively, it may prove advantageous to dispense with the FEC and rely on event reconstruction for the determination of the α-particle trajectory.)

The general geometry may be summarized by two planes, the median plane and the reaction plane.

Median Plane The plane defined by the center of the cylindrical target O, the center of the π^+ detector acceptance $O_{\pi d}$, and the center of the α detector acceptance $O_{\alpha d}$ (See Fig. 3.1). Both the π^+ and α detector acceptance planes are perpendicular to the median plane. The X and Z axes of the laboratory coordinate system $OXYZ$ lie on the median plane. The Z-axis is taken along the beam-axis and the Y-axis is normal to this plane. The system $oxyz$ is the $OXYZ$ system translated to the reaction point o.

Reaction Plane The plane defined by the trajectories of the incident proton and the emitted pion. Since the ^{5}He recoil also lies in this plane, the transformation to the ^{5}He c.m. system is constructed on this plane as well. There are two possible coordinate systems in the ^{5}He c.m. frame, the Transverse (T) frame and the Helicity (H) frame. The Z_T and Y_H-axes are normal to the reaction plane and the X_T and Z_H-axes are taken to be along the ^{5}He recoil direction.

Some of the geometrical parameters defined in Fig. 3.1 are listed in Table 3.1.

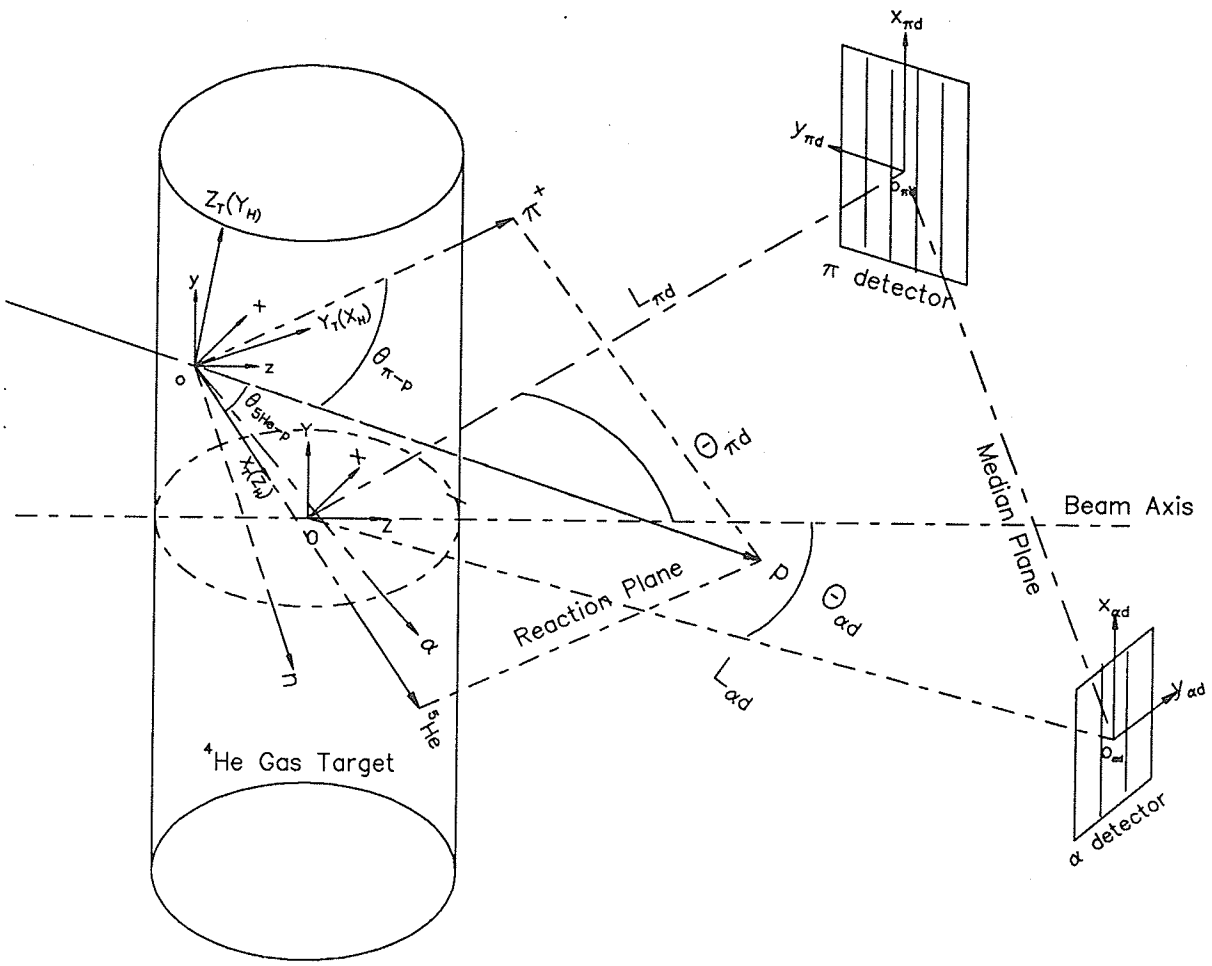

Figure 3.1: The General Geometry

Table 3.1: Some Simulation Parameters

Parameter	Defination	Value
R	Target Radius	1.5 cm
H	Target Height	8.0 cm
TD	Target Thickness	0.00254 cm
$L_{\pi d}$	π^+ Detector Acceptance Plane - Target Distance	63 cm
$L_{\alpha d}$	α Detector Acceptance Plane - Target Distance	100 cm
$\theta_{\pi d,H}$	π^+ Detector (MRS) Horizontal Acceptance	$\pm$ 0.8 deg
$\theta_{\pi d,V}$	π^+ Detector (MRS) Vertical Acceptance	$\pm$ 2.5 deg
$\theta_{\alpha d,H}$	$SASP^\dagger$ Horizontal Acceptance	$\pm$ 2.4 deg
$\theta_{\alpha d,V}$	$SASP^\dagger$ Vertical Acceptance	$\pm$ 5.9 deg
$\rho_{^4He}$	^4He Gas Target Density	0.007 g/cm^3
ρ_{Ha}	Havar Target Wall Density	8.30 g/cm^3
$\Theta_{\pi d}$	Angle of π^+ Detector Axis to Beam Axis	60°
$\Theta_{\alpha d}$	Angle of α Detector Axis to Beam Axis	$\sim$ 17.2°

†: α detector (see §4.2.4 for more detail about the acceptances required).

3.2 Event Generation Process

In this section, we will discuss how to generate the correlated events, each consisting of a pion and an α-particle in the laboratory. Figure 3.2 gives in more detail a schematic view concerning the event generating process.

3.2.1 Proton

The proton beam will be used in Dispersion-Matching mode which offers the possibility for better energy resolution (See §3.3.2 for details). In Dispersion-Matching mode, the proton momentum (or energy) is proportional to its displacement along the Y-axis.

1. First the Y coordinate, or Y_d, of a incident proton is selected from the dispersion information of the beam, and therefore the proton energy is calculated. The protons incident on the target are not necessarily parallel to the beam axis (Z-axis) due to the beam emittance. The beam particles exhibit a distribution in angle and position in a plane perpendicular to the beam-axis. This property can be described by two phase space ellipses, one for each of the horizontal (X) and vertical (Y) axes. These two ellipses are used to select a proton direction (θ_p, ϕ_p) and a reaction point $o(X_o, Y_o, Z_o)$ within the target. Full details of these will be discussed in §3.3.2.

2. Before the reaction takes place, the proton suffers a small amount of energy loss in passing through the target cell wall and along the path-length in the ^{4}He gas (multiple scattering is neglected). Both are subtracted from the incident proton energy. The energy loss calculations will be described in detail in §3.3.3.

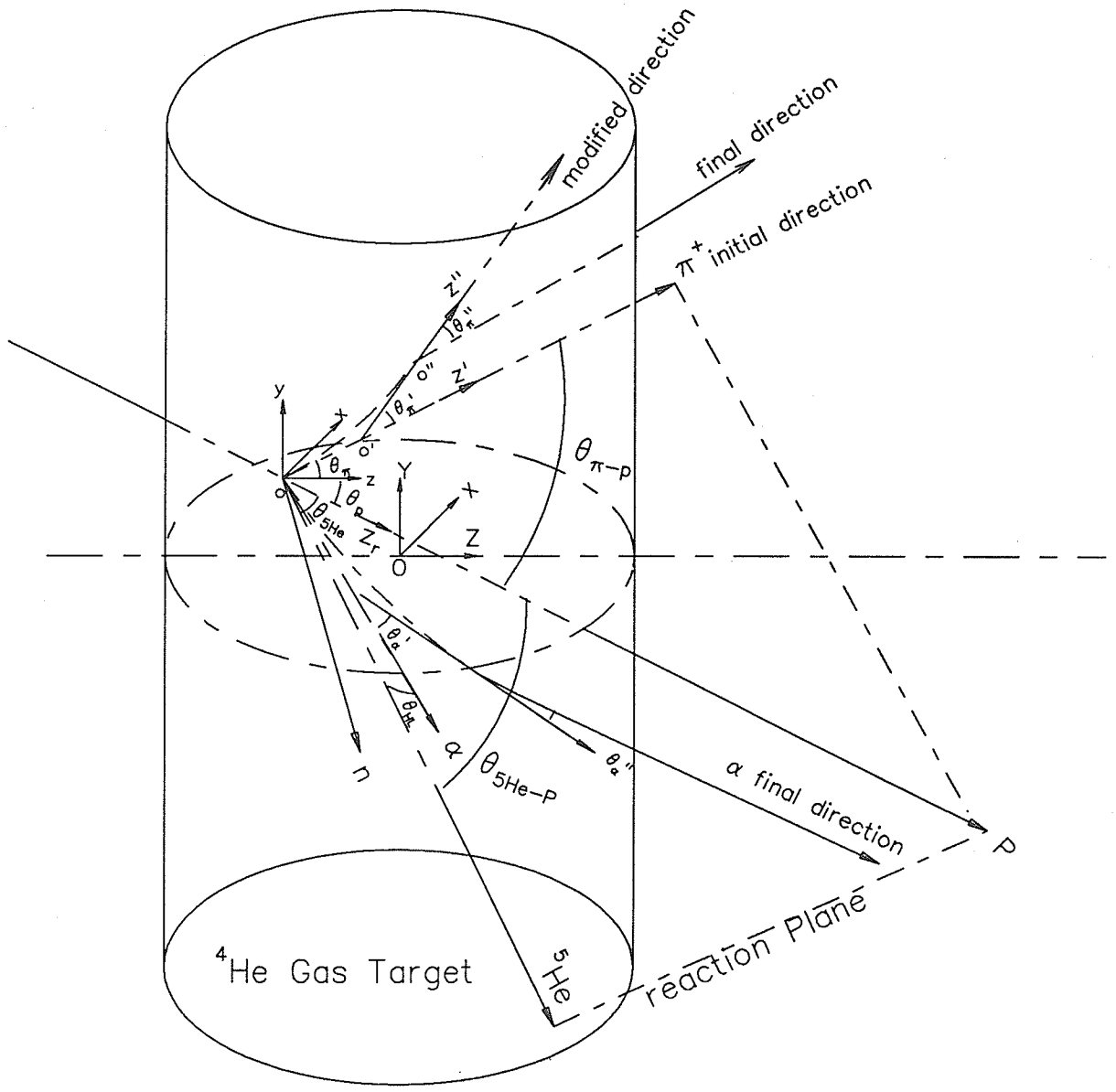

Figure 3.2: The Schematic of Constructing an Event

3.2.2 Pion (π^+)

At reaction point o, the proton interacts with the ^{4}He to produce a pion and ^{5}He. The frame $oxyz$ (which is the $OXYZ$ frame translated to the reaction point o) is rotated to the $ox_ry_rz_r$ frame, where z_r-axis is taken along the proton direction. Note only the z_r-axis is drawn in Fig. 3.2. The implementation of the rotation and the coordinate transformation between frames $oxyz$ and $ox_ry_rz_r$ are described in detail in §3.3.1 and is named COTRAN for generality.

1. The proton trajectory (z_r-axis) only tilts a little from the z-axis due to the emittance ($\theta_p < 1°$), so $ox_ry_rz_r$ and $oxyz$ are nearly the same frame. In addition, the distance between the target and the detector (63 cm) is much greater than the distance between the target center O and the reaction point o ($< 3\ cm$). Because of this, the π^+ scattering angle $\theta_{\pi-p}$ in frame $ox_ry_rz_r$ can be selected around a central value $\Theta_{\pi d}$, the angle formed by the π^+ detector axis with respect to the beam axis as defined in Table3.1. Note that the selection is governed by the angular distribution of the differential cross section (Fig. 2.7) in the region where the π^+ detector is located. The azimuthal angle $\phi_{\pi-p}$ can be uniformly selected around 0° (XZ plane), the center of the vertical angular acceptance of the detector. The pion direction ($\theta_{\pi-p}$, $\phi_{\pi-p}$) is explicitly defined in the $ox_ry_rz_r$ frame.

2. After selecting a ^{5}He mass from its g.s. excitation (See §3.3.6, practically we will map it only up to $3.3MeV$) and resorting to the reaction kinematics (see §3.3.5), we can calculate the ^{5}He scattering angle $\theta_{^5\mathrm{He-p}}$. The $\phi_{^5\mathrm{He-p}} = \phi_{\pi-p} + 180°$ (π^+, ^{5}He are in the reaction plane). Hence the ^{5}He direction ($\theta_{^5\mathrm{He-p}}, \phi_{^5\mathrm{He-p}}$) in the $ox_ry_rz_r$ frame is determined. Kinematics calculation also gives the energies of π^+ and ^{5}He.

3. Using the coordinate transformation program COTRAN, both ($\theta_{\pi-p}, \phi_{\pi-p}$) and ($\theta_{^5\mathrm{He-p}}, \phi_{^5\mathrm{He-p}}$) in $ox_ry_rz_r$ frame can be transformed to $oxyz$ frame to obtain (θ_π, ϕ_π) for π^+ and ($\theta_{^5\mathrm{He}}, \phi_{^5\mathrm{He}}$) for ^{5}He. Here ($\theta_\pi, \phi_\pi$) is denoted as

the initial direction of the π^+.

4. The initial direction and emitting point o define an initial trajectory equation for the π^+ in the $OXYZ$ frame. This equation, together with the inner surface equation of the target cell wall, permits the calculation of its path-length t in ^{4}He gas. From this, the energy loss and multiple scattering can be calculated. Refer to §3.3.4 about the multiple scattering calculation.

5. In determining the final direction of π^+ out of the ^4He gas, we assume that, due to the multiple scattering, π^+ traces an approximately circular arc and deflects gradually all the way through the ^4He gas. So the equivalent effect is that it deflects a total multiple scattering angle θ'_π at the midpoint o' of its initial straight line (path-length t), since from Fig. 3.3, the distance between o and o' is:

$$x = R\tan\frac{\theta'_\pi}{2} = t\frac{\tan\frac{\theta'_\pi}{2}}{\sin\theta'_\pi} \simeq \frac{t}{2}. \tag{3.1}$$

   The last step is due to $\theta'_\pi \ll 1$.

6. Now the frame $oxyz$ is rotated to a new frame $ox'y'z'$ instead of to $ox_ry_rz_r$, with z'-axis taken along the π^+ initial direction. The $ox'y'z'$ frame is further translated to o' (only z'-axis was drawn in Fig. 3.2).

   In frame $o'x'y'z'$, an azimuthal angle ϕ'_π for the multiple scattering can be uniformly selected. The multiple scattered direction (θ'_π, ϕ'_π) defined explicitly in this frame can be transformed to frame $oxyz$ by COTRAN, and yields the modified π^+ direction out of the ^{4}He gas. Since the coordinates for o' can be calculated from Step 4, we can write the modified trajectory equation for the pion in the $OXYZ$ frame.

7. The modified trajectory equation, in conjunction with the surface equations of the target cell wall, allow for the determination of the path-length through the wall. Following this, the energy-loss and multiple scattering in the wall can be calculated. Due to the very thin wall thickness, multiple scattering

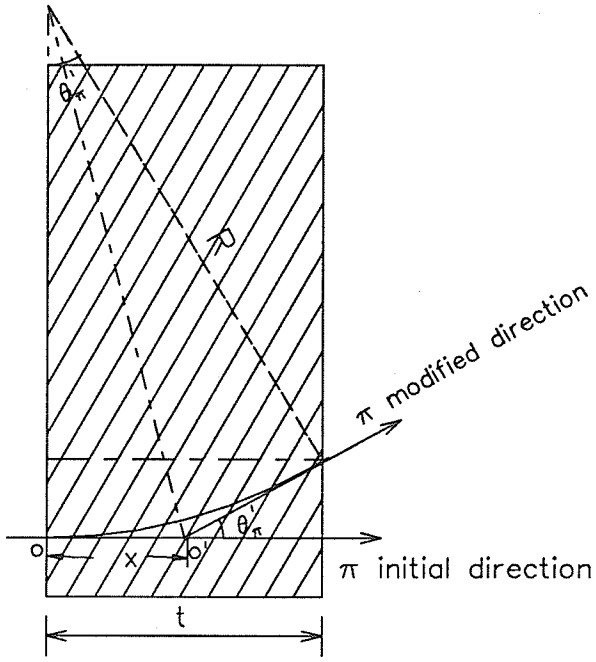

Figure 3.3: The Geometric Approximation of π^+ Multiple Scattering

angle θ''_π can be well defined referring to o'' (the intersection of the modified trajectory with the inner surface) as Fig. 3.3 implies.

8. As a repetition of step 6, frame $o'x'y'z'$ is also rotated and translated to a new frame $o''x''y''z''$, where z'' axis is set along the modified direction of π^+ (only the z''-axis was drawn in Fig. 3.2). In frame $o''x''y''z''$ the scattered direction $(\theta''_\pi, \phi''_\pi)$ is defined. Transforming $(\theta''_\pi, \phi''_\pi)$ to the frame $oxyz$ just uses COTRAN twice, ie. from $o''x''y''z''$ to $o'x'y'z'$ and, from $o'x'y'z'$ to $oxyz$. Therefore, the final direction of the π^+ is determined. With the coordinates of o'' calculated in Step 7, the final pion trajectory equation in $OXYZ$ frame can be set up.

9. The intersection of the final trajectory with the π^+ detector acceptance plane, defines the detection coordinates $(x_{\pi d}, y_{\pi d})$ in $o_{\pi d}x_{\pi d}y_{\pi d}$ frame as shown in Fig. 3.1. If either of the two coordinates is outside the detector acceptance, the event is rejected. Note that due to the magnetic optics of the detector (MRS spectrometer), the effective acceptance for the reac-

tion point o is smaller than the full acceptance for the target center O, as shown in Fig. 3.4.

Finally, a π^+-event is defined by the three experimentally determined quantities: direction, position $(x_{\pi d}, y_{\pi d})$ and energy. Two Front End Chambers (FEC) will be used to measure the direction and position and the MRS will determine the energy.

Note that due to pion decay in the $\sim 11m$ flight path through the MRS, about 50% of the pions will decay to muons. Muon events can be eliminated from pion events by using the event reconstruction information through the MRS, and will not broaden appreciably the pion spectra, as calculated by Furutani[5] in our first phase of the experiment. Since we will use two FECs instead of one FEC at the entrance of the MRS in this experiment, we can determine the pion direction both at the entrance and at the focal plane, and hence the reconstruction process is more tightly constrained.

3.2.3 α−particle

If a π^+-event is accepted, we perform the following calculations for the α-particle.

1. The lifetime of ^{5}He is only about 10^{-22} sec. So, ^{5}He breaks up essentially right at the reaction point o into an α-particle and a neutron.

2. The frame we choose to describe the breakup distribution of ^{5}He is the recoil c.m. transverse frame $oX_TY_TZ_T$ as shown in Fig. 3.1 ($Z_T \perp$ reaction plane), in which the correlation function (2.25) is applied. The individual harmonic functions associated with each statistical tensor t_{kq} in $W(\theta, \phi)$, and their maximum and minimum values, are listed in Table 3.2.

   The α-event is generated, separately, for both the positive and negative portion of each individual distribution function of W_i. In the sampling procedure, for a randomly selected direction (θ_T, ϕ_T), if $W_i(\theta_T, \phi_T) > 0$ and, if a random number selected from (0, Maximum) is $\leq W_i(\theta_T, \phi_T)$, the

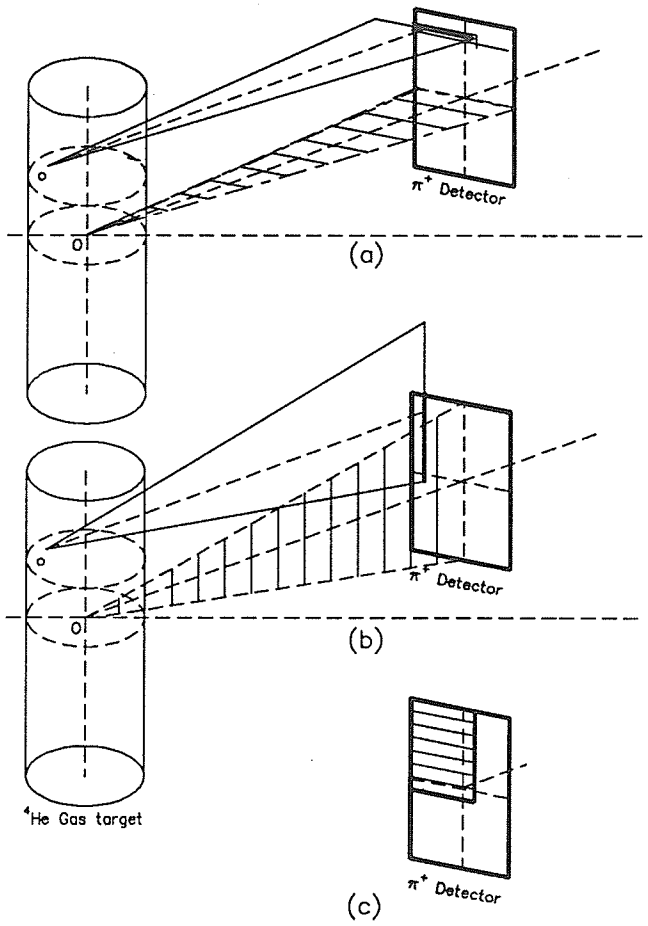

Figure 3.4: The Effective (a) Horizontal and (b) Vertical Acceptance of π^+ Detector for the Reaction Point o. (c) The Full Acceptance (Shadowed Area)

Table 3.2: The Individual Harmonic Functions in the Correlation Function $W(\theta, \phi)$

	Function	Maximum	Minimum
W_0	$1 \sim Y_{00}$	1	1
W_1	$-\frac{1}{2}(3\cos^2\theta - 1) \sim Y_{20}$	$\frac{1}{2}$	-1
W_2	$-\sqrt{\frac{3}{2}}\sin^2\theta\cos 2\phi \sim Re(Y_{22})$	$\sqrt{\frac{3}{2}}$	$-\sqrt{\frac{3}{2}}$
W_3	$-\sqrt{\frac{3}{2}}\sin^2\theta\sin 2\phi \sim Im(Y_{22})$	$\sqrt{\frac{3}{2}}$	$-\sqrt{\frac{3}{2}}$

event is taken as a positive one for W_i (positive only for W_0). Otherwise if $W_i(\theta_T, \phi_T) < 0$, and if a random number selected from (Minimum , 0) is $\geq W_i(\theta_T, \phi_T)$, the event is then accepted as a negative one for W_i.

Transformation of (θ_T, ϕ_T) to the recoil c.m. helicity frame $oX_HY_HZ_H$ (doing a cyclic permutation to the three axes of $oX_TY_TZ_T$ frame, ie., $X_T \rightarrow Z_H, Y_T \rightarrow X_H, Z_T \rightarrow Y_H$) gives the breakup direction (θ_H, ϕ_H). θ_H is the c.m. breakup angle with respect to ^{5}He (Z_H-axis). See Appendix B.4 for details of this transformation.

3. The ^{5}He(g.s., $\frac{3}{2}^-$) $\rightarrow$ n + α breakup kinematics will be described in §3.3.5. Using equation (3.30) we can calculate the laboratory break-up angle θ_{HL} from θ_H. The laboratory azimuthal angle $\phi_{HL} = \phi_H$. (θ_{HL}, ϕ_{HL}) is the breakup direction in the laboratory helicity frame. The α energy is calculated by equation (3.31).

4. The axes of the laboratory helicity frame are the respective axes of the c.m. helicity frame $(oX_HY_HZ_H)$ defined in the $oxyz$ frame as follows:

$$\hat{\mathbf{n}}_{Z_H} = \hat{\mathbf{n}}_{^5\mathrm{He}}, \tag{3.2}$$

$$\hat{\mathbf{n}}_{Y_H} = \frac{\hat{\mathbf{n}}_{^5\mathrm{He}} \times \hat{\mathbf{n}}_p}{|\hat{\mathbf{n}}_{^5\mathrm{He}} \times \hat{\mathbf{n}}_p|}, \tag{3.3}$$

$$\hat{\mathbf{n}}_{X_H} = \hat{\mathbf{n}}_{Y_H} \times \hat{\mathbf{n}}_{Z_H}. \tag{3.4}$$

The transformation of the breakup direction (θ_{HL}, ϕ_{HL}) to the $oxyz$ frame is straight forward (See Appendix B.5). This yields the α initial direction in the $oxyz$ frame.

5. The remaining work is exactly the same as that carried out for the π^+ after its initial direction is determined in the $oxyz$ frame, ie. from step 4 to step 8 in §3.2.2.

6. The intersection of the α trajectory with the α detector plane also defines the α detection coordinates $(x_{\alpha d}, y_{\alpha d})$ in $o_{\pi d}x_{\pi d}y_{\pi d}$ frame. For the time being, all of the α particles correlated with the accepted pions are recorded without further acceptance limitations.

In the end, an α-event is defined by its energy and position $(x_{\alpha d}, y_{\alpha d})$. Experimentally, the SASP and an Front End Chamber (FEC) each will be applied to measure the energy and position respectively.

3.3 Simulation Subroutines

The following sections give descriptions in detail of a few major subroutines used in the simulation process.

3.3.1 COTRAN and Some Analytical Geometry

The subroutine COTRAN is used frequently for trajectory transformation as seen in the preceding section. We assume two coordinate frames: OXYZ and Oxyz, as shown in Fig. 3.5. Rotating the OXYZ frame by an angle θ_0 along an axis lying on the OXY plane by an angle of $90° - \phi_0$ to X-axis, one can easily obtain the Oxyz frame. For instance, frames OXYZ and Oxyz, when applied at the beginning of §3.2.2, represent frames $oxyz$ and $ox_ry_rz_r$ respectively and, $(\theta_0, \phi_0) = (\theta_p, \phi_p)$.

Euler rotations with $(\alpha, \beta, \gamma) = (\phi_0, \theta_0, \phi_0)$ are equivalent to such a transformation [37]:

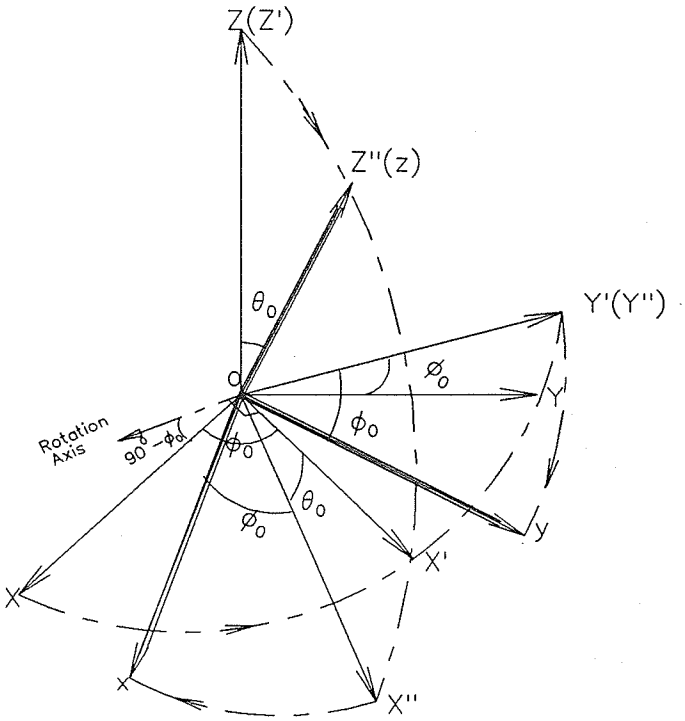

Figure 3.5: The Geometry of COTRAN Transformation

$$\text{OXYZ} \xrightarrow{\phi_0 \text{ alongZ}} \text{OX'Y'Z'} \xrightarrow{\theta_0 \text{ alongY'}} \text{OX''Y''Z''} \xrightarrow{\phi_0 \text{ alongZ''}} \text{Oxyz}.$$

Therefore the coordinate transformation from Oxyz to OXYZ is:

$$\mathbf{M} = \begin{pmatrix} \cos\theta_0\cos^2\phi_0 + \sin^2\phi_0 & \cos\phi_0\sin\phi_0(\cos\theta_0 - 1) & \cos\phi_0\sin\theta_0 \\ \cos\phi_0\sin\phi_0(\cos\theta_0 - 1) & \cos\theta_0\sin^2\phi_0 + \cos^2\phi_0 & \sin\phi_0\sin\theta_0 \\ -\cos\phi_0\sin\theta_0 & -\sin\phi_0\sin\theta_0 & \cos\theta_0 \end{pmatrix}. \quad (3.5)$$

If in the Oxyz frame a particle moves in direction (θ, ϕ) through O , its trajectory unit vector is $\hat{\mathbf{n}} = (n_x, n_y, n_z) = (\sin\theta\cos\phi, \sin\theta\sin\phi, \cos\theta)$. Then in the OXYZ frame (or any frame with axes parallel to the respective axes of the OXYZ frame), the unit vector $\hat{\mathbf{N}} = \mathbf{M}\hat{\mathbf{n}}$. The trajectory equation is:

$$\frac{X - X_O}{N_X} = \frac{Y - Y_O}{N_Y} = \frac{Z - Z_O}{N_Z}, \quad (3.6)$$

where (X_O, Y_O, Z_O) are the coordinates of O measured with respect to the $OXYZ$ frame.

3.3.2 Dispersion-Matched Beam and Phase Space Ellipse

In this subsection, a brief introduction is first given to the Dispersion-Matched Beam. Then from the dispersion information and the phase space ellipses of the beam, we can select the direction, reaction coordinates and energy for an incident proton.

The Principle of Dispersion Matching

TRIUMF beam line 4B can be tuned to produce either an achromatic tune, which has a typical beam spot size of $2mm \times 2mm$, or a dispersed tune. A dispersed tune is the one with the protons distributed according to their momentum along the length of the beam spot perpendicular to the scattering plane. The advantage in using the dispersed tune is for fully utilizing the resolution of the MRS. If the dispersed beam is placed on the target such that the highest momentum protons are located at the top of the beam spot, and the lowest momentum protons are at the bottom, and if the momentum dispersion of the produced pions is exactly the same as the dispersion of the MRS dipole magnet, then pions produced from the large momentum protons will fall on the same location of the focal plane as the pions produced from the small momentum protons. In effect, this reduces the momentum spread of the proton beam to zero, and the resolution obtained will be due to the intrinsic resolving power of the MRS. If an achromatic tune is used, the resolution will be determined primarily by the momentum spread of the proton beam.

The dispersion matching condition is determined from the reaction kinematics and the optical properties of the MRS. The required tune dispersion d is

$$d = -(\frac{D_s}{M_s})(\frac{p_B}{p_S})(\frac{dp_S}{dp_B})_{rm}, \tag{3.7}$$

where

$\frac{D_s}{M_s} = 11cm/\%$ is the dispersion to magnification ratio of the MRS.

p_B is the momentum of the proton beam.

p_S the pion momentum of the central ray through the MRS.
$(\frac{dp_S}{dp_B})$ is the amount that the pion momentum changes when the proton momentum is changed, holding the recoil mass constant. This quantity can be calculated from relativistic kinematics.

The length of the beam spot is determined by the product of the beam momentum spread $\Delta P/P$ and the beam tune dispersion d. For the ^{4}He$(\vec{p},\pi^+)^5$He(g.s.) reaction at $T_p = 400MeV$, $\theta_\pi = 60°$, the kinematic calculation yields $P_p/P_\pi \simeq 3.28$ and $dP_\pi/dP_p \simeq 0.632$. The dispersion tune required is $\simeq -22cm/\%$. Such a tune will produce a beam spot of $\sim 3.2cm$ $(\pm 1.6cm)$ under the momentum spread of $\simeq 0.15\%\Delta P/P$ ($\pm 0.075\%$ for 4B line). We assume the dispersion exhibits a Gaussian distribution of $FWHM$=1.6cm, with a σ-value of $0.68cm$.

The beam dispersion, which is in the horizontal plane, needs to be rotated to the vertical plane before reaching the target, since the MRS is a vertical bending spectrometer. The rotation is accomplished by the twister (a system of six quadruples), which also exchanges the horizontal and vertical phase space as we discuss below.

The total energy dispersion is ΔT_p.

$$\Delta T_p = T_p(1 + \frac{m_p}{m_p + T_p})\frac{\Delta P}{P}. \tag{3.8}$$

A linear dispersion matching relation exists between the dispersed energy T_p and the dispersed position Y_d:

$$T_p = T_{p,av} + \frac{Y_d}{1.6cm} \cdot \frac{\Delta T_p}{2}. \tag{3.9}$$

where $T_{p,av}$ is the average energy of the beam, or the energy on the Median-Plane. The energy resolution of the Dispersion-Matching beam is represented by $\frac{\Delta T_p}{3.2cm}$, which is $\sim 0.04MeV/mm$ for $T_p = 400MeV$. Figure 3.6 shows the spectra of beam energy distribution and position distribution in the vertical direction.

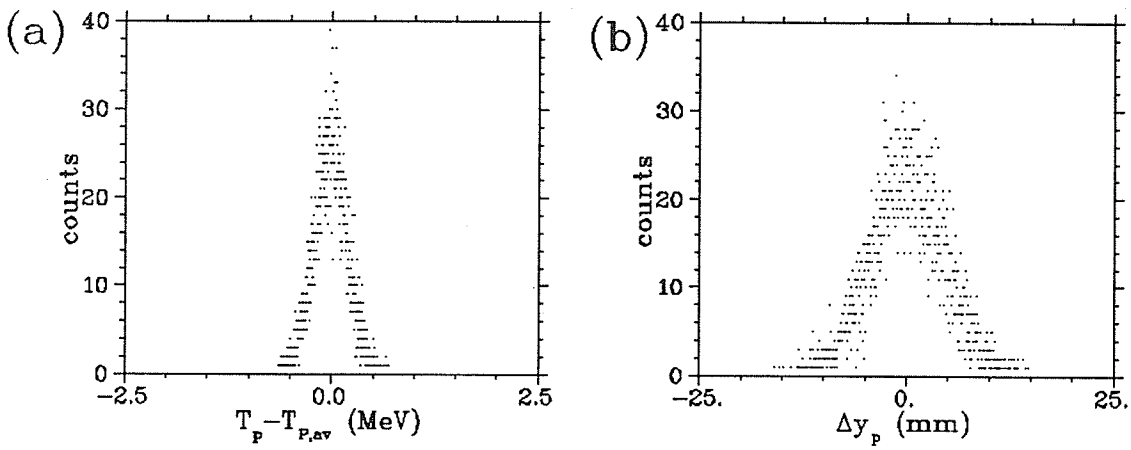

Figure 3.6: The (a) Energy Dispersion and (b) Position Dispersion of the Proton Beam at $T_p = 400MeV$ Generated in the Monte-Carlo Simulation

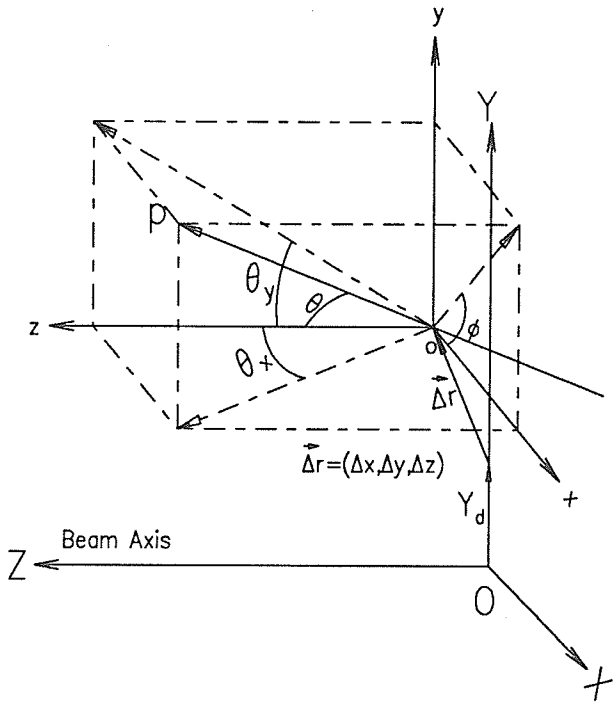

Figure 3.7: The Schematic View of Phase Space Effect

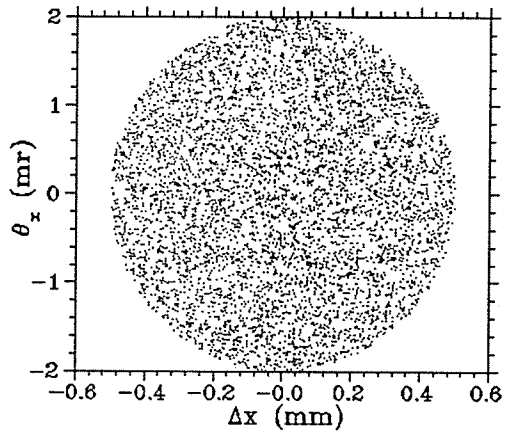

Figure 3.8: The Horizontal Ellipse Generated in the Monte-Carlo Simulation

The Phase Space Ellipses

Figure 3.7 gives a schematic view of the phase space effect of the incident proton beam, in which θ_x, θ_y denote the divergence angles in the horizontal and vertical directions respectively, and $\Delta x, \Delta y$ represent the translations from the dispersed position.

As mentioned in §3.2.1, the distribution $\Delta x - \theta_x$ can be described by a phase space ellipse, and similarly the $\Delta y - \theta_y$ distribution. As the beam drifts in space, the ellipses rotate with their areas remaining constant. If the beam is focused to produce a waist (minimum width) in one direction then an upright phase space ellipse is produced. We can assume at each dispersion position a uniform distribution of protons over the area of the ellipse.

The area of each ellipse is the beam emittance in the corresponding direction. For the TRIUMF 4B beam line, the emittances are:

$$H(X): \ 8.0\pi \ mm \cdot mr, \qquad V(Y): \ 1.0\pi \ mm \cdot mr.$$

When the beam having a dispersed tune passes through the tuning twister, the horizontal and vertical emittances are interchanged. Empirically, the new horizontal ellipse (emittance $1.0\pi \ mm \cdot mr$) has a half width of $0.5mm$ and a

half-divergence of $2.0mr$ and, the new vertical ellipse (emittance $8.0\pi\ mm \cdot mr$) has a half width $0.5mm$ and a half divergence $16.0mr$. As an example, Fig. 3.8 shows the horizontal ellipse generated in the Monte Carlo simulation.

From the two ellipses, we can chose two pairs of parameters $(\Delta x, \theta_x)$ and $(\Delta y, \theta_y)$ for a proton. If Y_d is the dispersed position of the proton, then $(\Delta x, \Delta y + Y_d)$ plus another position coordinate Δz chosen from the uniform distribution along the Z-axis [with $(\Delta x)^2 + (\Delta z)^2 < R^2$] gives the reaction coordinates in the $OXYZ$ frame.

(θ_x, θ_y) determine the incident direction (θ_p, ϕ_p), since

$$\cos\theta_p = \frac{1}{\sqrt{1 + \tan^2\theta_x + \tan^2\theta_y}} \simeq 1, \tag{3.10}$$

$$\tan\phi_p = \frac{\tan\theta_y}{\tan\theta_x}. \tag{3.11}$$

3.3.3 The Energy Loss

When a heavy charged particle passes through a thin absorber of thickness Δx, the average energy loss is:

$$\Delta_{av} = -\frac{dE}{dx} \cdot \Delta x, \tag{3.12}$$

where the stopping power

$$-\frac{dE}{dx} = \frac{4\pi z^2 e^4}{m_e \beta^2} NZ(\ln[\frac{2m_e\beta^2}{I(1-\beta^2)}] - \beta^2), \tag{3.13}$$

is the Bethe-Bloch equation[22], in which β is the velocity and z the charge number of the particle, and Z the atomic number, N the number of atoms/cm^3, and I the mean ionization potential of the absorber.

The problem of the energy loss distribution was treated exactly by Vavilov [23]. That exact distribution can be divided into several categories depending on the values of the parameter κ, where

$$\kappa = \frac{\xi}{\epsilon_{max}}, \tag{3.14}$$

and

$$\epsilon_{max} = \frac{2m_e\beta^2}{(1-\beta^2)},$$
$$\xi = \frac{2\pi z^2 e^4}{m_e\beta^2} NZx = 0.3sz^2\frac{m_eZ}{\beta^2 A},$$

with ϵ_{max} the maximum energy transfer in a single particle-electron collision. s is the mass thickness (g/cm^2) and A is the atomic weight of the absorber.

1. If $\kappa \gg 1.$, the distribution is Gaussian,

$$f_G(\lambda) = \frac{1}{\sqrt{2\pi}\sigma} e^{-\lambda^2}, \tag{3.15}$$
$$\lambda = \frac{\Delta - \Delta_{\rm av}}{\sigma},$$

with the variance $\sigma^2 = 4\pi z^2 e^4 NZx$.

2. If $\kappa \ll 1.$, the distribution is Landau, which is highly asymmetrical with a broad peak (FWHM $= 4.02\xi$ [24]) around the most probable energy loss Δ_{mp}, and a long tail corresponding to higher energy losses. Here

$$f_L(\lambda) = \frac{1}{\pi}\int_0^\infty e^{-u(\ln u+\lambda)} \sin \pi u du, \tag{3.16}$$
$$\lambda = \frac{\Delta - \Delta_{\rm av}}{\xi} - (\ln\kappa + \beta^2 - {\rm C} + 1.0),$$

and $C = 0.577\cdots$ is the Euler constant. The $f_L(\lambda)$ calculated from the above expression is shown in Fig. 3.9. In such cases $\Delta_{mp} \ll \Delta_{av}$ with [24]

$$\Delta_{\rm mp} = \xi(\ln[\frac{2{\rm m_e}\beta^2\xi}{{\rm I}^2(1-\beta^2)}] - \beta^2 + 0.198) = \Delta_{\rm av} + \xi(\ln\kappa + \beta^2 + 0.198). \tag{3.17}$$

3. If $\kappa \sim 1.0$, the exact Vavilov distribution is applied. Then

$$f_V(\lambda) = \frac{\kappa}{\pi\xi} e^{\kappa(1+\beta^2 C)} \int_0^\infty e^{\kappa f_1} \cos(y\lambda + \kappa f_2) dy, \tag{3.18}$$

$$\lambda = \frac{\Delta - \Delta_{\rm av}}{\epsilon_{\rm max}} - \kappa(1 + \beta^2 - {\rm C}) = \kappa(\frac{\Delta - \Delta_{\rm mp}}{\xi} + \ln\kappa - 0.802 + {\rm C}), \tag{3.19}$$

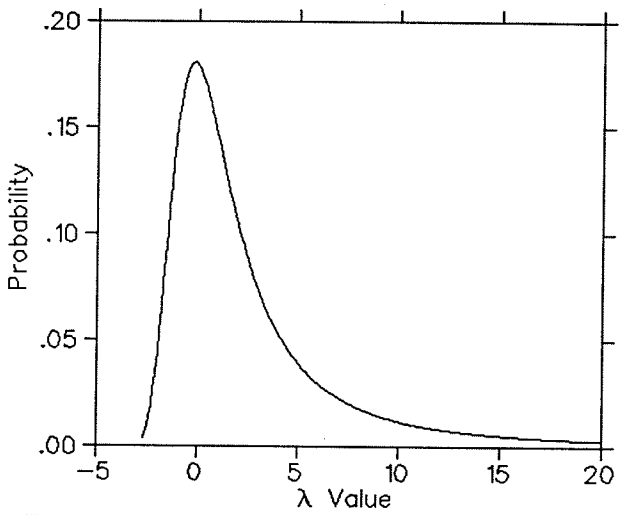

Figure 3.9: The Landau Universal Distribution

where

$$f_1 = \beta^2(\ln y - Ci(y)) - \cos y - ySi(y),$$

$$f_2 = y(\ln y - Ci(y)) + \sin y + \beta^2 Si(y).$$

Si and Ci are the Sine and Cosine integrals[25].

If $\kappa >\sim 1.0$, the exact distribution can be approximated well by

$$f_A(\lambda) = \frac{1}{\eta\sqrt{\pi}} e^{a\lambda - \frac{a^3}{3}} v(\lambda), \tag{3.20}$$

$$\lambda = \frac{\Delta - \Delta_{av}}{\eta} + a^2,$$

in which

$$v(\lambda) = \frac{1}{\sqrt{\pi}} \int_0^\infty \cos(y\lambda + \frac{y^3}{3}) dy,$$

is the Airy function, and

$$\eta = \xi[\frac{(2\kappa)^2}{(1 - \frac{2}{3}\beta^2)}]^{-\frac{1}{3}}, \qquad a = (1 - \frac{\beta^2}{2})[\frac{2\kappa}{(1 - \frac{2}{3}\beta^2)^2}]^{\frac{1}{3}}.$$

In the simulation process, we first calculate the parameter κ for a particle and then try to obtain $f(\lambda)_{max}$ for the distribution appropriate to the particle. From the relative distribution $h(\lambda) = \frac{f(\lambda)}{f(\lambda)_{max}}$, we can choose a λ to determine the energy loss Δ. The applicable κ regions for various distributions are set as follows [26,27]:

1. $\kappa \geq 10$ (Gaussian): here $h_G(\lambda) = e^{-\lambda^2}$, we chose a λ from $(-3, 3)$. $h_G(\lambda)$ is negligible when $|\lambda| > 3$.

2. $\kappa \leq 0.005$ (Landau): $f_L(\lambda)$ is a *universal* function with $f_L(\lambda)_{max} \simeq 0.1806$ at $\lambda = -0.2$. we chose a λ from $(-3, 18)$, since $h_L(\lambda)$ is negligible beyond this region. Based on the $f_L(\lambda)$'s calculated at a series of discrete λ values, using a cubic spline technique[15], the value of $f_L(\lambda)$ for any value of λ and thus $h_L(\lambda)$ can be obtained.

3. $2 \leq \kappa \leq 10$ (AIRY): Now $f_A(\lambda)$ is not a *universal* function of λ. We have to find $f_A(\lambda)_{max}$ for each individual case related via the parameters η and a. Since the Airy function is not skewed much from a Gaussian, we can search $f_A(\lambda)_{max}$ in the area $\Delta - \Delta_{av} = (-3\sigma, +0.5\sigma)$ by calculating $f_A(\lambda)$ step by step with starting point $+0.5\sigma$, until the maximum point is reached. In this manner $h_A(\lambda)$ was determined for each combination of parameters η and a.

4. $0.005 \leq \kappa \leq 2$ (Exact Vavilov): We need to find $f_V(\lambda)_{max}$ for each individual case of ξ as well. From equation (3.17), we note that when $\kappa >\sim 0.3$, the term $\xi(\ln\kappa + \beta^2 + 0.198)$ is ~ 0 or $\Delta_{mp} = \Delta_{av}$. This suggests that when $\kappa >\sim 0.3$, the distribution doesn't deviate much from a Gaussian, and the method described above for Airy's distribution can still be applied. However, when $\kappa < 0.3$, the difference between Δ_{mp} and Δ_{av} is greater and the skewed distribution deviates from a Gaussian and approaches that of the Landau distribution. Now the preferred approach is to search for $f_V(\lambda)_{max}$ around Δ_{mp} rather than around Δ_{av}. The latter part of equation (3.19) is applied and the searching is carried out in the area $\Delta - \Delta_{mp} = (-1.5\sigma, +1.5\sigma)$ with the starting point $+1.5\sigma$ now. In the end, $h_V(\lambda)$ can be determined for any individual ξ case over the whole applicable range of κ.

The simulation results show that almost all p, π^+ particles are Landau distributed both in the ^{4}He gas and in the target cell wall. For α-particles, either the

exact Vavilov distribution or the Airy distribution is involved in both materials.

The target cell wall is made from a high strength cobalt-base alloy material called Havar (Appendix E gives in detail a description of the material properties). Since the stopping power is proportional to Z, the total energy loss in the material has to be weighted according to the sum of each element by its mass content.

Fig. 3.10 shows in detail the energy losses for both π^+ and α-particle obtained from the simulation process, from which we can observe the characteristics for each particle as just described.

3.3.4 Multiple Scattering

A narrow beam of particles transversing an absorber will suffer many small angle scatterings, yielding an angular distribution at the end of the absorber.

In order to describe this multiple scattering, the angular distribution, $F_a(\theta) = \frac{1}{I} \cdot \frac{dI}{d\Omega}$, defined as the probability of the beam intensity scattered into $d\Omega = \sin\theta d\theta d\phi$ is used, where θ is the polar angle with respect to the beam-axis.

$F_a(\theta)$ is given by a function $F(x)$ of the reduced angle $x = \frac{\theta}{\chi_c\sqrt{B}}$[29]

$$F(x) = \frac{1.}{2\pi\chi_c^2 B} \cdot (2exp(-x^2) + \frac{f^{(1)}(x)}{B} + \frac{f^{(2)}(x)}{B^2} + \cdots), \tag{3.21}$$

where $f^{(1)}$ and $f^{(2)}$ are the first and second order Moliere functions respectively[30]. Their values are listed in Table 3.3. Parameter B is defined below.

Since $F_{max}(x) = F(0)$, the relative distribution is $h(x) = \frac{F(x)}{F(0)}$. The definitions according to Marion and Zimmermann[31] for χ_c^2 and b are:

$$\chi_c^2 = 0.1569 \cdot \frac{Z(Z+1)z^2 s}{p^2 \cdot \beta^2 A}, \tag{3.22}$$

$$b = \ln[2730\frac{Z^{\frac{1}{3}}(Z+1)z^2 t}{A\beta^2}] - 0.1544, \tag{3.23}$$

and

$$B - \ln B = b. \tag{3.24}$$

The solution for B is numerically obtained by iterating $B_n = b + \ln B_{n-1}$, with

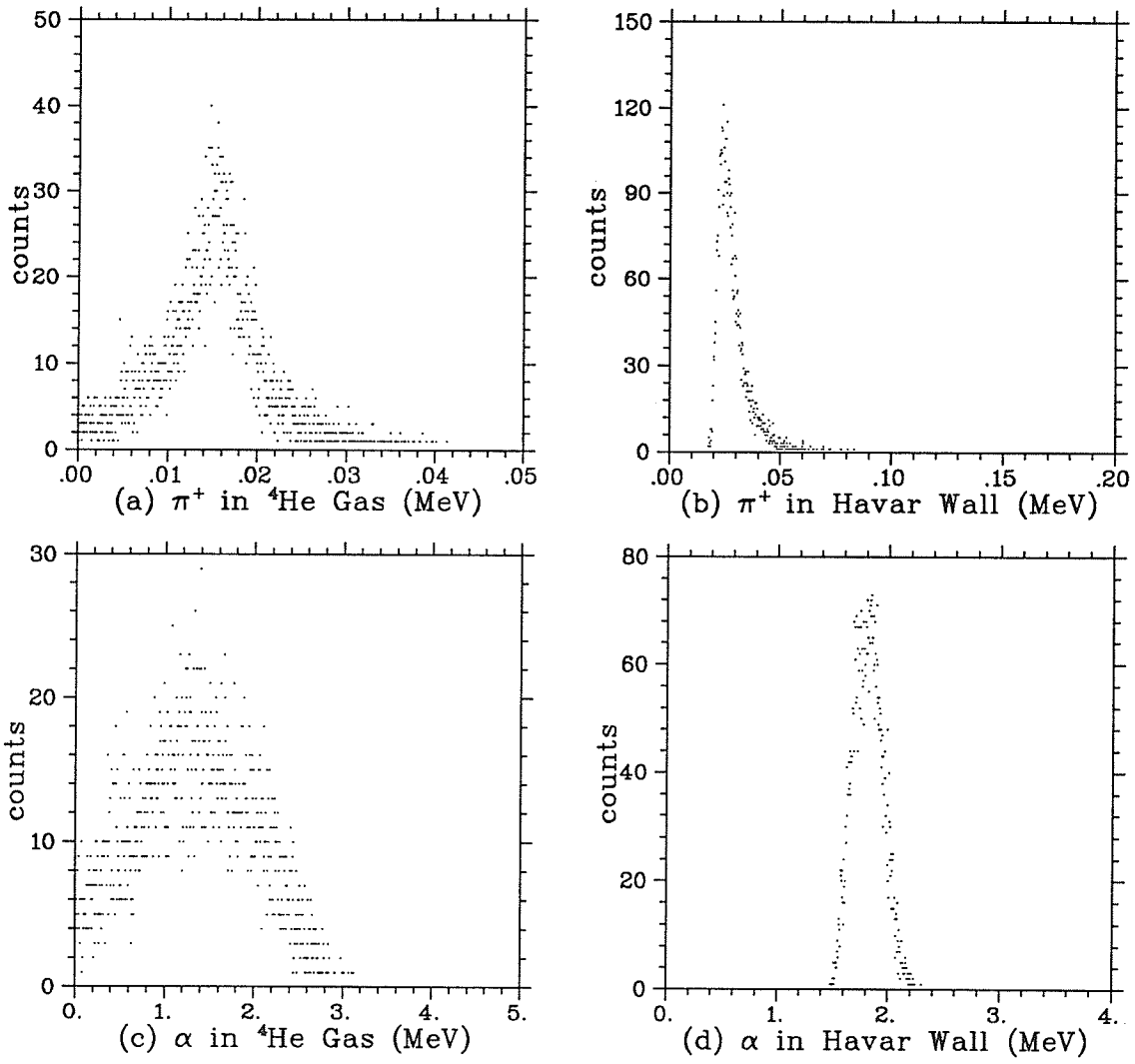

Figure 3.10: The α and π^+ Energy Loss Distribution in both Target Gas and Cell Wall in the Simulation Process

Table 3.3: The Moliere Function

x	$f^{(1)}(x)$	$f^{(2)}(x)$	x	$f^{(1)}(x)$	$f^{(2)}(x)$
0.0	0.845600	2.492900	4.2	0.008460	0.001343
0.2	0.703800	2.069400	4.4	0.006809	0.001291
0.4	0.343700	1.048800	4.6	0.005552	0.001155
0.6	-0.077700	-0.004400	4.8	0.004587	0.000991
0.8	-0.398100	-0.606800	5.0	0.003831	0.000833
1.0	-0.528500	-0.635900	5.2	0.003226	0.000697
1.2	-0.477000	-0.308600	5.4	0.002735	0.000586
1.4	-0.318300	0.052500	5.6	0.002337	0.000492
1.6	-0.139600	0.242300	5.8	0.002010	0.000414
1.8	-0.000600	0.238600	6.0	0.001739	0.000350
2.0	0.078200	0.131600	6.2	0.001514	0.000296
2.2	0.105400	0.019600	6.4	0.001323	0.000252
2.4	0.100800	-0.046700	6.6	0.001163	0.000215
2.6	0.082620	-0.064900	6.8	0.001025	0.000184
2.8	0.062470	-0.054600	7.0	0.000908	0.000158
3.0	0.045500	-0.035680	7.2	0.000807	0.000137
3.2	0.032880	-0.019230	7.4	0.000720	0.000119
3.4	0.024020	-0.008470	7.6	0.000644	0.000103
3.6	0.017910	-0.002640	7.8	0.000579	0.000090
3.8	0.013660	0.000050	8.0	.000521	0.000078
4.0	0.010638	0.001074			

$B_0 = b$ as the starting point and $B = \lim B_n$. Usually only $n = 4$ or 5 iterations are needed.

The solid angle effect is taken into proper consideration by choosing $\cos\theta$ from $(-1, 1)$ rather than choosing θ from $(0°, 180°)$. Furthermore, from equation (3.21) and Table 3.3, it is seen that when $x \geq 8.0$ or $\theta \geq \theta_0 = 8.0\chi_c\sqrt{B}$, $F(x)$ is very small. Hence it is sufficient to choose $\cos\theta$ uniformly from $(\cos\theta_0, 1)$ rather than from $(-1, 1)$, and this makes the sampling more efficient. From the values of f^1, f^2 at discrete values of x, we used a cubic spline technique[13] to get the values for any $x \leq 8.0$.

For the material Havar, the various effective values can be calculated as follows:

$$\begin{aligned} \overline{Z(Z+1)} &= \textstyle\sum_i f_i Z_i(Z_i+1) \qquad for\ \chi_c^2, \\ \overline{Z^{\frac{1}{3}}(Z+1)} &= \textstyle\sum_i f_i Z_i^{\frac{1}{3}},(Z_i+1) \qquad for\ b, \\ \overline{A} &= \textstyle\sum_i f_i A_i \qquad for\ A, \end{aligned}$$

where f_i is the mass fraction of i^{th} element in the material (see Appendix E). The multiple scattering for both π^+ and α-particles from the simulation processes is shown in Fig. 3.11.

3.3.5 Kinematics

The ^{4}He$(\vec{p}, \pi^+)^5$He reaction kinematics as well as the ^{5}He(g.s., $\frac{3}{2}^-$) $\rightarrow$ n + α breakup kinematics are discussed in this section. Fig. 3.12 presents schematically a velocity diagram of them.

^{4}He$(\vec{p}, \pi^+)^5$He Reaction

In the reaction center of mass system, the total energy is

$$E^* = (2T_p M_{4He} + (M_p + M_{4He})^2)^{\frac{1}{2}}, \tag{3.25}$$

and the reaction c.m. velocity is

$$\beta_C = \frac{\sqrt{\Gamma_C^2 - 1}}{\Gamma_C}, \qquad \Gamma_C = \frac{E}{E^*} = \frac{T_p + M_p + M_{4he}}{E^*}.$$

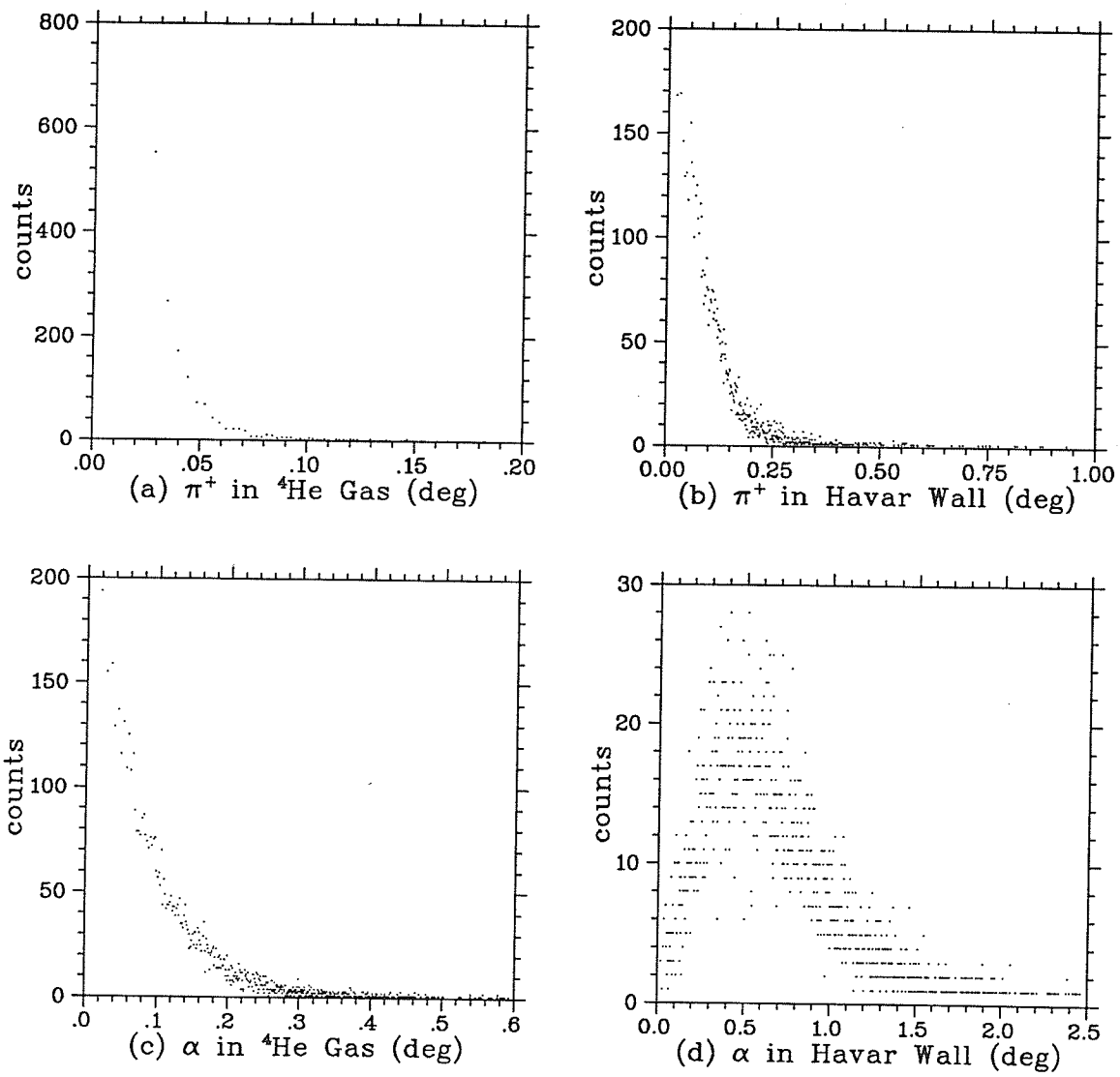

Figure 3.11: The α and π^+ multiple scattering distribution in both the target gas and cell wall in the simulation process. The vertical scale shows the number of events scattered at an angle θ.

Starting from $E^* = E^*_{\pi^+} + E^*_{5He}$ and $P^*_\pi = P^*_{5He} = P^*$, we have

$$\mathrm{P^{*2}} = \frac{[\mathrm{E^{*2}} - (\mathrm{M_{5He}} - \mathrm{M}_\pi)^2][\mathrm{E^{*2}} - (\mathrm{M_{5He}} + \mathrm{M}_\pi)^2]}{4\mathrm{E^{*2}}}. \tag{3.26}$$

therefore

$$\beta^*_\pi = \frac{P^*}{E^*_\pi}, \qquad \beta^*_{^5\mathrm{He}} = \frac{P^*}{E^*_{^5\mathrm{He}}}.$$

For proton energies T_p of 200-500 MeV,

$$\beta_C < \beta^*_\pi, \qquad \beta_C > \beta^*_{^5\mathrm{He}},$$

Thus the π^+ can be emitted through the whole $0° - 180°$ angular range with an energy

$$\mathrm{E}_\pi = \frac{\mathrm{E}^*_\pi + \beta_\mathrm{C}\cos\theta_\pi\sqrt{\mathrm{P^{*2}} - (\Gamma_\mathrm{C}\beta_\mathrm{C}\mathrm{M}_\pi\sin\theta_\pi)^2}}{\Gamma_\mathrm{C}(1 - \beta^2_\mathrm{C}\cos^2\theta_\pi)}. \tag{3.27}$$

If we decide to observe the π^+ in a θ_π direction, then the overall momentum conservation can determines the ^{5}He recoil angle and its momentum value as follows:

$$\tan\theta_{^5\mathrm{He}} = \frac{\mathrm{P}_\pi\sin\theta_\pi}{\mathrm{P_p} - \mathrm{P}_\pi\cos\theta_\pi}, \qquad \mathrm{P}_{^5\mathrm{He}} = \mathrm{P}_\pi\frac{\sin\theta_\pi}{\sin\theta_{^5\mathrm{He}}}.$$

Since $\beta_C > \beta^*_{^5\mathrm{He}}$, the laboratory recoil angle of ^{5}He is less than $90°$.

$^5\mathrm{He}(\mathrm{g.s.}, \frac{3}{2}^-) \rightarrow \mathrm{n} + \alpha$ Breakup

In the ^{5}He rest frame (recoil c.m. system), the four-momentum $\mathbf{P} = (\vec{\mathrm{P}}, \mathrm{iE})$ conservation $\mathbf{P}_{^5\mathrm{He}} = \mathbf{P}_\alpha + \mathbf{P_n}$ or $\mathbf{P^2_n} = (\mathbf{P}_{^5\mathrm{He}} - \mathbf{P}_\alpha)^2$ gives

$$-M^2_n = -M^2_{^5\mathrm{He}} - M^2_\alpha + 2M_{^5\mathrm{He}}E^*_\alpha, \tag{3.28}$$

with excitation energy $Q = M_{^5\mathrm{He}} - M_\alpha - M_n$ substituted in, (3.28) yields

$$E^*_\alpha = \frac{Q^2 + 2QM_n}{2M_{^5\mathrm{He}}} + M_\alpha. \tag{3.29}$$

Assuming that in the ^{5}He c.m. frame (Helicity System), the α breakup angle is θ^*_α, then in the laboratory frame the breakup angle is

$$\tan\theta_\alpha = \frac{\tan\theta^*_\alpha}{\gamma_\mathrm{c}(1 + \frac{\beta_\mathrm{c}}{\beta^*_\alpha\cos\theta^*_\alpha})}, \tag{3.30}$$

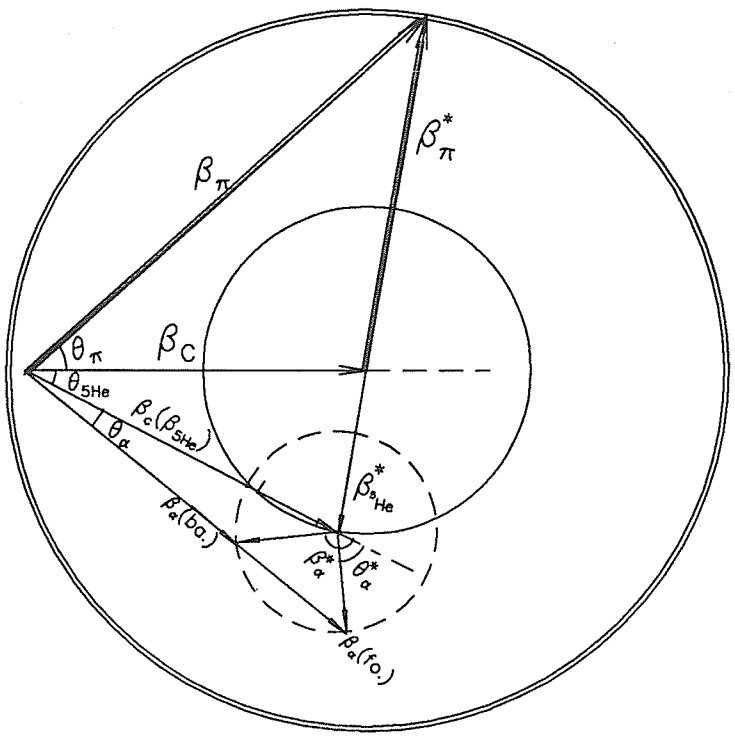

Figure 3.12: The Velocity Diagram of the Kinematics

and the α energy

$$E_\alpha = \gamma_c(E^*_\alpha + \beta_c P^*_\alpha \cos\theta^*_\alpha), \tag{3.31}$$

where β_c is the ^{5}He (recoil center of mass) velocity and β^*_α is the velocity of the α-particle in the ^{5}He rest frame. Since $\beta^*_\alpha < \beta_c$ if the ^{5}He is produced by 200-500 MeV protons, there also exists a maximum breakup angle in the laboratory frame (See right of Fig. 3.13). At each lab angle less than the maximum breakup angle, α-particles of two different energies can be emitted.

In the Monte-Carlo simulation (See §3.2.3), first an α direction (θ_T, ϕ_T) was selected according to the angular distribution in the c.m. transverse system, then (θ_T, ϕ_T) was transformed to the c.m. Helicity System to obtain the breakup direction (θ_H, ϕ_H). With the breakup angle θ_H (θ^*_α) known, we can use (3.30) and (3.31) to calculate the laboratory breakup angle θ_{HL} (θ_α) and energy E_α.

Fig. 3.13 shows the kinematical calculation at $T_p = 400\ MeV$, from which we see $\theta_{^5\mathrm{He}}$ reaches a maximum value $\simeq 17.2°$ when $\theta_\pi = 60°$. In an actual

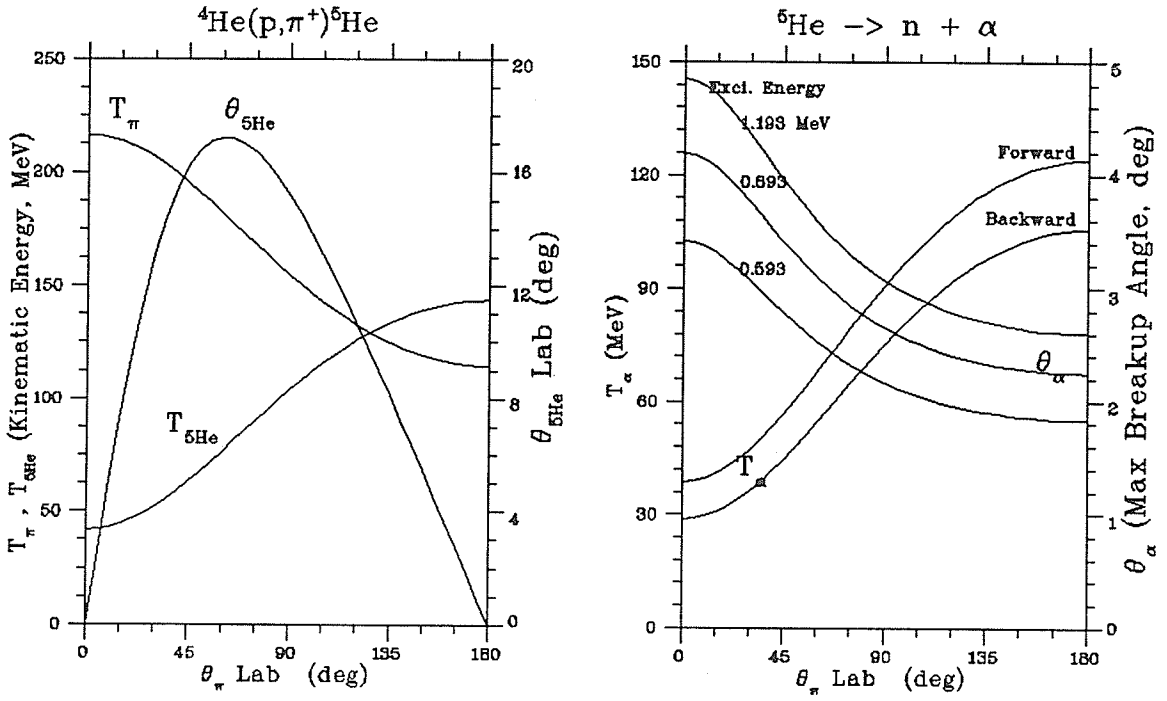

Figure 3.13: Kinematics for $T_P = 400\ MeV$ (The Exci. Energy of ^{5}He is 0.893 MeV in the calculation of T_π, T_{5He}, θ_{5He} and T_α).

experiment, a good initial choice for the π^+ and α detectors would be along these two directions respectively. Selecting the largest possible angle for the ^{5}He recoil also means that the breakup α-particles will appear at larger angles with respect to the beam direction, and away from the intense proton elastic scattering.

3.3.6 The ^{5}He g.s. Excitation Function

In a previous study of the ^{4}He$(\vec{p},\pi^+)^5$He reaction, Germond and Wilkin[32] performed a calculation of the final state interactions between the n and α for the ^{5}He low lying states in terms of the separable potentials acting in the $n-\alpha$ system. The model reproduces well the ^{5}He excitation energy spectra observed in the ^{4}He$(\vec{p},\pi^+)^5$He reactions at $T_p = 201\ MeV$ [33] and $T_p = 800\ MeV$ [6]. Based on such a model, Furutani[5] also performed a similar but simplified calculation by further assuming that the final state interaction is independent of the momentum

transfer. The calculation also did a good job of describing the peak shapes of our TRIUMF E564 experimental data. In addition, he found that, apart from a normalization factor, the ^{5}He recoil spectrum is independent of angle and proton energy, at least for an excitation energy up to 5 MeV.

Now for simplicity, we try to use an analytical function to depict such an asymmetrical distribution. One method might be the modification of the symmetrical Breit-Wigner distribution, which in a simplified form (up to a normalization constant) is:

$$f(x) = \frac{1}{1+x^2}, \qquad x = \frac{E - E_0}{\frac{\Gamma}{2}}, \tag{3.32}$$

The modification factor could be in the form $e^{\frac{x}{C}}$, or

$$F(x) = \frac{1}{1+x^2} e^{\frac{x}{C}}, \tag{3.33}$$

where C is some positive number. For ^{5}He g.s., $E_0 = 0$, a satisfactory empirical form for C was found to be

$$C = \begin{cases} 1.5 & x < 0 (E < 0), \\ 1.5 + \frac{x}{6} & x > 0 (E > 0). \end{cases}$$

The function $F(E)$, as shown in Fig. 3.14(a), can well depict the excitation function. Fig. 3.14(b) shows the ^{5}He g.s. generated in the simulation process based on this function.

3.4 The Simulation Results for Individual Harmonic Functions

We performed our calculation at proton beam energy $T_{P,av} = 400\ MeV$. The upper limit ^{5}He g.s. excitation energy was chosen at 3.3 MeV. α detector acceptances were assumed large enough to accept all of the breakup α-particles.

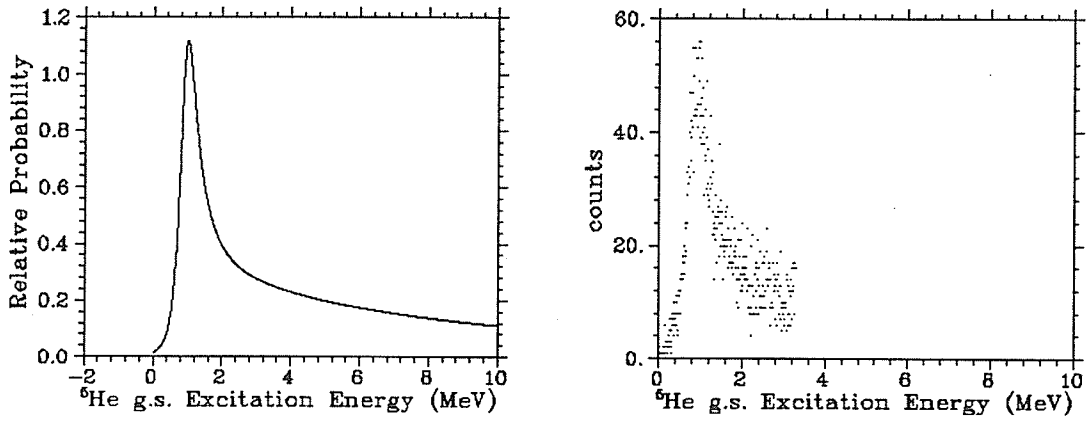

Figure 3.14: ^{5}He g.s. Excitation Energy relating $n+\alpha$ (a) The depicted analytical distribution and (b) Generated distribution in the simulation process

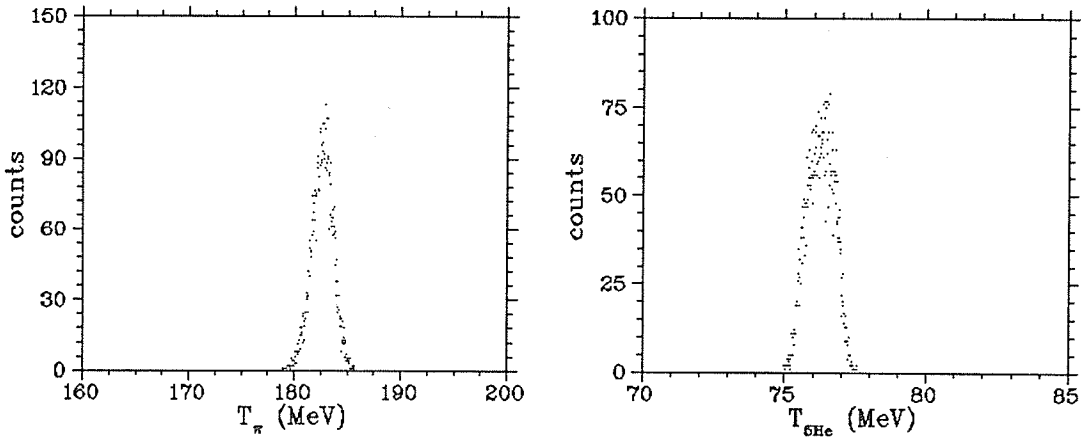

Figure 3.15: The π^+ and ^{5}He Energy Distributions in the Simulation Process

The energy spectra of the π^+ and ^{5}He are plotted in Fig. 3.15. Fig. 3.16 and Fig. 3.17 show the α energy spectrum and its position distribution for each individual harmonic function in the correlation function (2.25). The positive and negative events are calculated and graphed separately.

3.5 Simulated Experimental Data(SED)

Under the normalization condition $t_{00} = 1$, we try to search for those sets of tensor polarization values $(t_{20}, Re(t_{22}), Im(t_{22}))$ in the correlation function $W(\theta, \phi)$ that meet the following requirements:

1. $W(\theta, \phi) \geq 0$ for any (θ, ϕ) in $(0-180°, 0-360°)$, ie. the breakup probability shouldn't be negative in the whole range of solid angle.

2. The positivity of the density matrix $0 \leq \rho_{m_B m_B} \leq 1$ and $\sum_{m_B} \rho_{m_B m_B} = 1$ imposes the following restrictions on the tensor values for spin $S = \frac{3}{2}$ [7]:

$$(a) \quad -1 \leq t_{20} \leq 1, \qquad (b) \quad \sum_{kq} |t_{kq}|^2 \leq 2S + 1 = 4, \qquad (c) \quad t_{00} = Tr(\rho). \tag{3.34}$$

Shown in Fig. 3.18 is the sliced view of the searched *volume* in the space spanned by t_{20}, $Re(t_{22})$ and $Im(t_{22})$, in which each point represents an acceptable set of tensor polarization values. The set of polarization tensors to be extracted from the real experiment is a point somewhere within this *volume*.

Since no real experimental data have been measured as yet, we have to obtain a sample of simulated data for checking the validity of the tensor extraction process described in the following chapter. As shown in Fig. 2.2 (the two dash-boxes), we can generate this simulated data by picking a point from the *volume* (which means a set of acceptable tensors as noted in the input block), putting the values into $W(\theta, \phi)$ and passing this through the *Monte Carlo apparatus*. Now the input is the non-negative full correlation function. Depending on the sign of t_{20}, the maximum of the function is listed in Table 3.4.

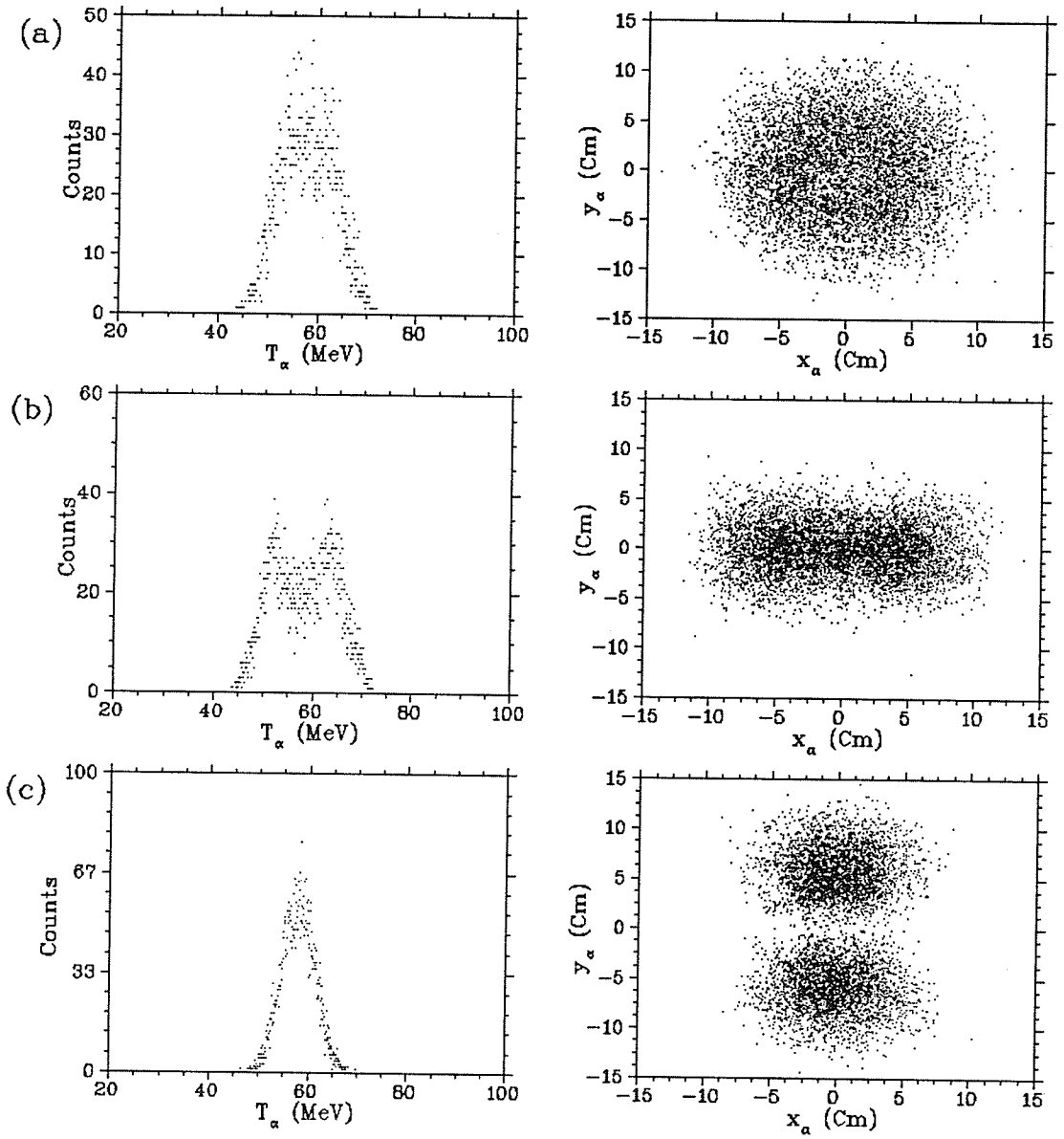

Figure 3.16: α Energy Spectrum and its Position Distribution (Recorded in $o_{\alpha d}x_{\alpha d}y_{\alpha d}$ frame shown in Fig. 3.1) for Each Harmonic Functions Listed in Table 3.2 (In Transverse Frame). (a):W_0, (b):$W_1(+)$, (c):$W_1(-)$.

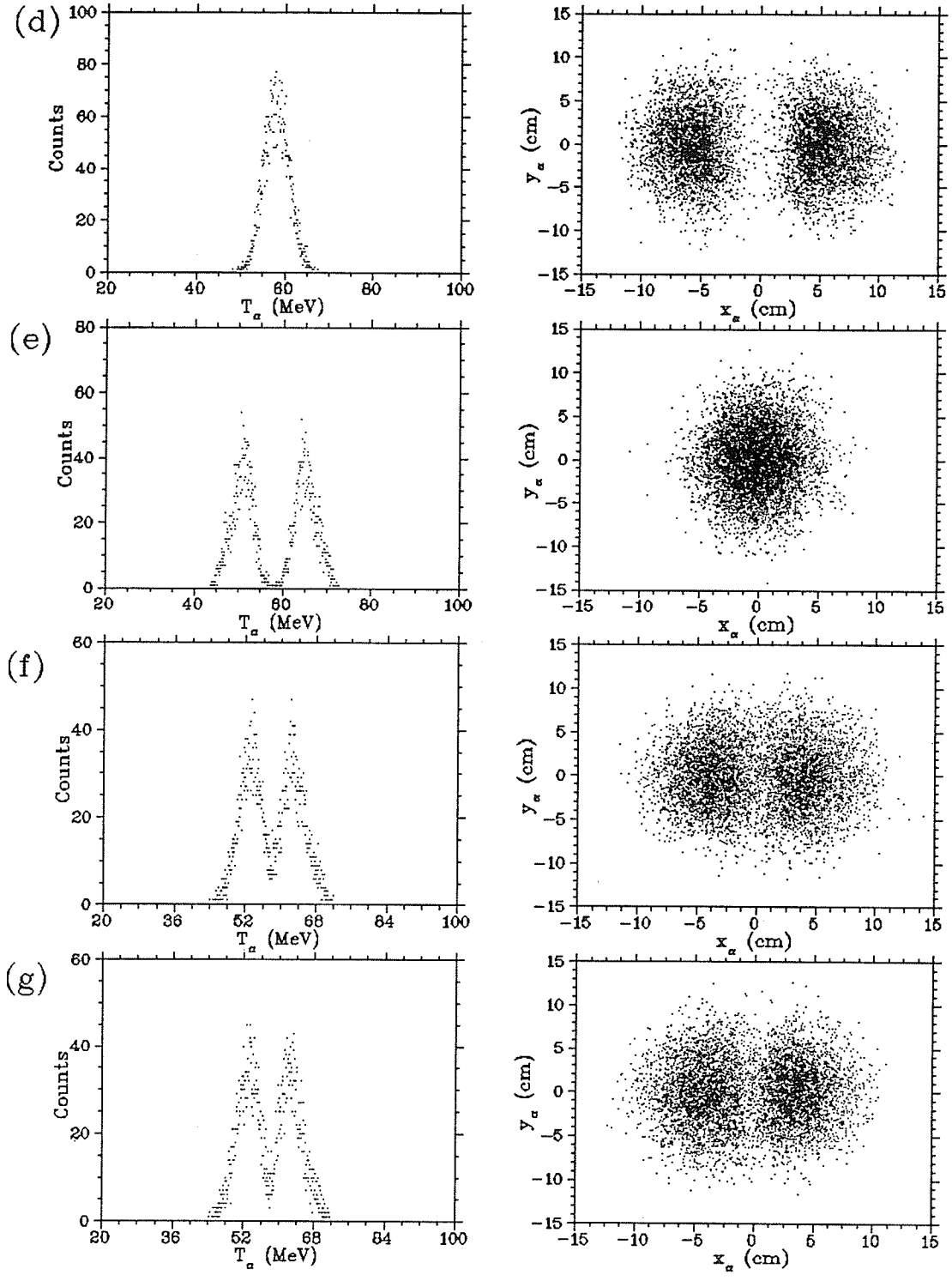

Figure 3.17: Continuation of Fig 3.16. (d):$W_2(+)$, (e):$W_2(-)$, (f):$W_3(+)$, (g):$W_3(-)$.

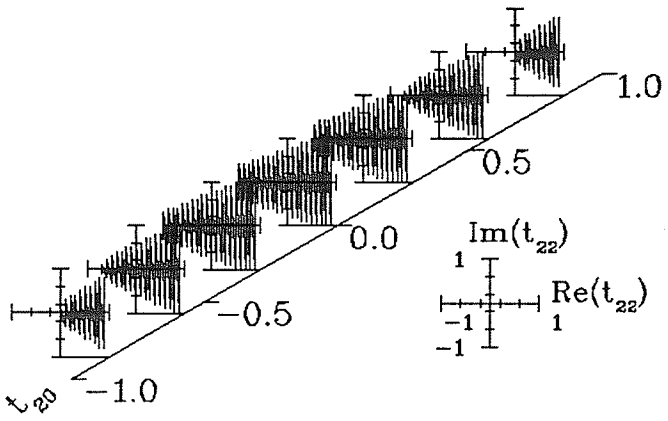

Figure 3.18: The sliced view of the acceptable *volume* of t_{20}, $Re(t_{22})$ and $Im(t_{22})$

Table 3.4: Maximum Values of the Correlation Functions

t_{20}	maximum	
≥ 0	$1 + \frac{1}{2}t_{20} + \sqrt{\frac{3}{2}}\|t_{22}\|$	
< 0	$1 + \frac{1}{2}t_{20} + \sqrt{\frac{3}{2}}\|t_{22}\|$	if $\sqrt{\frac{3}{2}}\|t_{20}\| \leq \|t_{22}\|$
	1 - t_{20}	if $\sqrt{\frac{3}{2}}\|t_{20}\| > \|t_{22}\|$

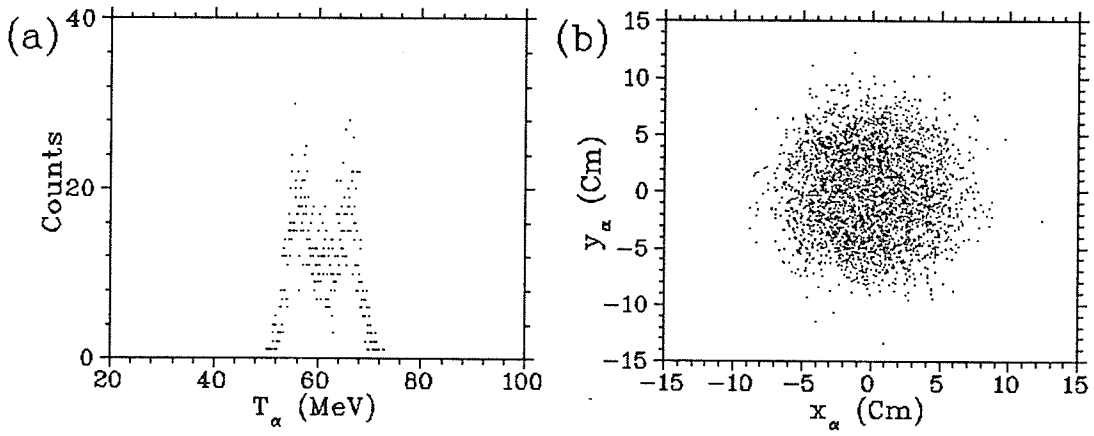

Figure 3.19: *Simulated Experimental Data* (a) α Energy spectrum (b) α position distribution for $(t_{20}, Re(t_{22}), Im(t_{22}))$ =(-0.2,-0.6,0.2)

The tensor set we chose to produce a sample of *Simulated Experimental Data* (SED) was $(t_{20}, Re(t_{22}), Im(t_{22})) = (-0.2, -0.6, 0.2)$, one *point* in the searched *volume*. Fig. 3.19 shows the obtained α energy spectrum and its position distribution on the detector acceptance plane for this particular case.

Chapter 4

Event Reconstruction and Data Analysis Simulation

The *Lab Position and Energy Distributions* (LPED) of α particles corresponding to each individual harmonic function (for both positive and negative portions), as well as to a full correlation function (ie. the *Simulated Experimental Data*, or SED) have been calculated through the Monte-Carlo simulations described in detail in the preceding chapter. In the following sections, we will first perform the event target reconstruction for these lab distributions, then carry out a detailed data analysis simulation based on these reconstructed distributions.

4.1 Event Target Reconstruction

Event target reconstruction is in fact a process opposite to that of the Monte Carlo simulation. With the information obtained in the laboratory for a given event, one can trace back to the recoil c.m. system to find the α emitting direction and hence the angles in the c.m. system. The full angular distribution corresponding to the *Lab Position and Energy Distributions* (LPED) can be reconstructed if this process is carried out for all of the events.

4.1.1 The Reconstruction Process

In the reconstruction process, many uncertainties involved in the determination of the particles' energy, position, trajectories direction etc. have been taken into account. The position and energy uncertainties are due mainly to the resolutions of the detectors.

The process involves a few steps:

1. The MRS will be used to measure the pion energy. Its typical resolution in dispersion matching mode is 0.2 MeV[34]. This resolution is due mainly to the multiple scattering in the wire chamber windows.

   In determining the trajectory direction of π^+, we prefer, in a more efficient way, to use two Front End Chambers (FEC), though MRS transport information plus one FEC would also suffice (angular resolution $1mr$). Pion positions are recorded in two FECs whose relative distance L_F is known. We can then calculate the trajectory direction. The position resolution of a FEC is typically $0.7mm$, which is taken as the uncertainty in each FEC coordinate.

2. Since no beam phase space effect can be taken into account practically in the process of reconstruction, we can only assume that the event originated somewhere in the YZ plane (See Fig. 3.1), with all protons incident in parallel to the beam axis (Z-axis). Therefore the intersection point of the π^+-trajectory with the YZ ($X = 0$) plane is the reaction point o_r, with vertical coordinate $Y_{d,r}$ determining the energy of the incident proton from the dispersion information on the beam.

   Now the path-length of the π^+ in both the target wall and the ^{4}He gas can be calculated. The energy loss in both materials can be further calculated and added to the measured energy. With the reconstructed energy $T_{\pi^+,r}$ and direction, we can set up the π^+ velocity vector $\vec{V}_{\pi^+,r}$. The angle formed by $\vec{V}_{\pi^+,r}$ to the reconstructed proton velocity vector $\vec{V}_{p,r}$ is the π^+ scattering

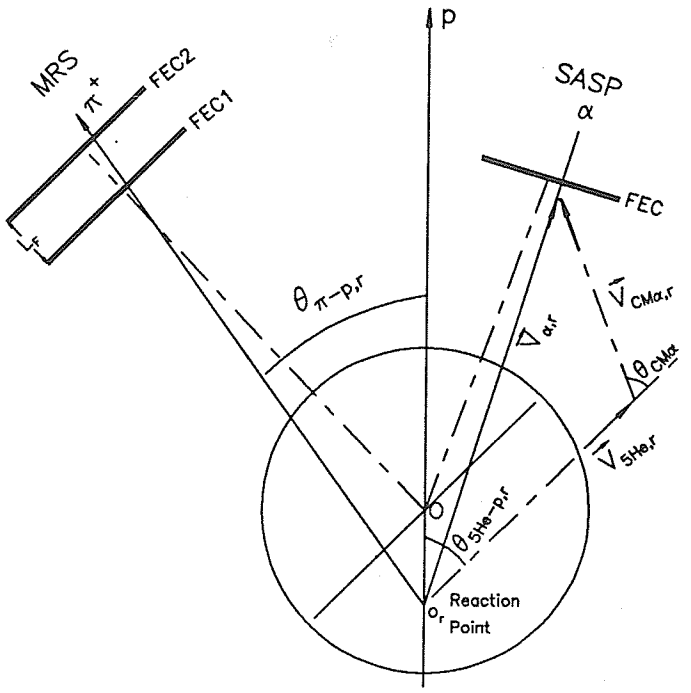

Figure 4.1: The schematic of the target reconstruction (top view)

angle $\theta_{\pi-p,r}$.

3. Conservation of momentum and energy yields

$$P_{^5\mathrm{He,r}} = (P_{p,r}^2 + P_{\pi,r}^2 - 2P_{p,r}^2 P_{\pi,r}^2 \cos\theta_{\pi-p,r})^{\frac{1}{2}}, \tag{4.1}$$

$$E_{^5\mathrm{He,r}} = E_{p,r} + M_{^4He} - E_{\pi,r}, \tag{4.2}$$

The ^{5}He mass and scattering angle can be calculated respectively by

$$M_{^5\mathrm{He,r}} = \sqrt{E_{^5\mathrm{He,r}}^2 - P_{^5\mathrm{He,r}}^2}, \qquad \sin\theta_{^5\mathrm{He-p,r}} = \frac{P_{\pi,r}}{P_{^5\mathrm{He,r}}}\sin\theta_{\pi-p,r}, \tag{4.3}$$

The excitation energy $Q_r = M_{^5\mathrm{He,r}} - M_\alpha - M_n$ is also determined.

In addition, the coplanarity of p, π^+ and ^{5}He gives

$$\phi_{^5\mathrm{He-p,r}} = \phi_{\pi-p,r} + 180°.$$

The angle information $(\theta_{^5\mathrm{He-p,r}}, \phi_{^5\mathrm{He-p,r}})$ is used to reconstruct the ^{5}He trajectory and its velocity $\vec{V}_{^5\mathrm{He,r}}$.

4. The $SASP$ spectrometer, which will be used to detect the α- particle, provides information about its momentum and direction. The energy resolution is expected to be $0.3MeV$. The position resolution is $0.7mm$ if a FEC is used (If no FEC, the angular resolution is typically $2mr$). With these uncertainties taken into account, the ^{5}He break-up point (ie. the reaction point o_r) and the above spectrometer information defines the α trajectory and α velocity $\vec{V}_{\alpha,r}$. A correction to the magnitude of $\vec{V}_{\alpha,r}$ is made to account for the average energy loss in the ^4He gas and the target cell wall.

5. It is seen from Fig. 3.12 that

$$\vec{V}_{\alpha,r} = \vec{V}_{^5\mathrm{He,r}} + \vec{V}_{CM\alpha,r}. \tag{4.4}$$

Thus with $\vec{V}_{\alpha,r}$ determined and $\vec{V}_{^5\mathrm{He,r}}$ obtained from (4.1), $\vec{V}_{CM\alpha,r}$ or the trajectory direction of the α particle in the recoil c.m. system can finally be determined.

4.1.2 Reconstruction Results

Event reconstructions for the LPEDs of the individual harmonic functions, denoted as *Simulated Individual Function Distributions* (SIFDs) for simplicity, are shown on the left of Fig. 4.2 and Fig. 4.3. Also shown on the right side are the distributions of the original functions themselves.

Fig. 4.4 shows the reconstructed distributions for T_p, $T_{^5\mathrm{He}}$ and ^{5}He g.s. excitation energy.

Event target reconstruction for the SED as described in §3.5 is shown in Fig. 4.5. This distribution, in parallel to those SIFDs, is named as *Simulated Correlation Function Distribution* (SCFD). The correlation function itself for generating the SED at $(t_{20}, Re(t_{22}), Im(t_{22})) = (-0.2, -0.6, 0.2)$ is also shown on this figure.

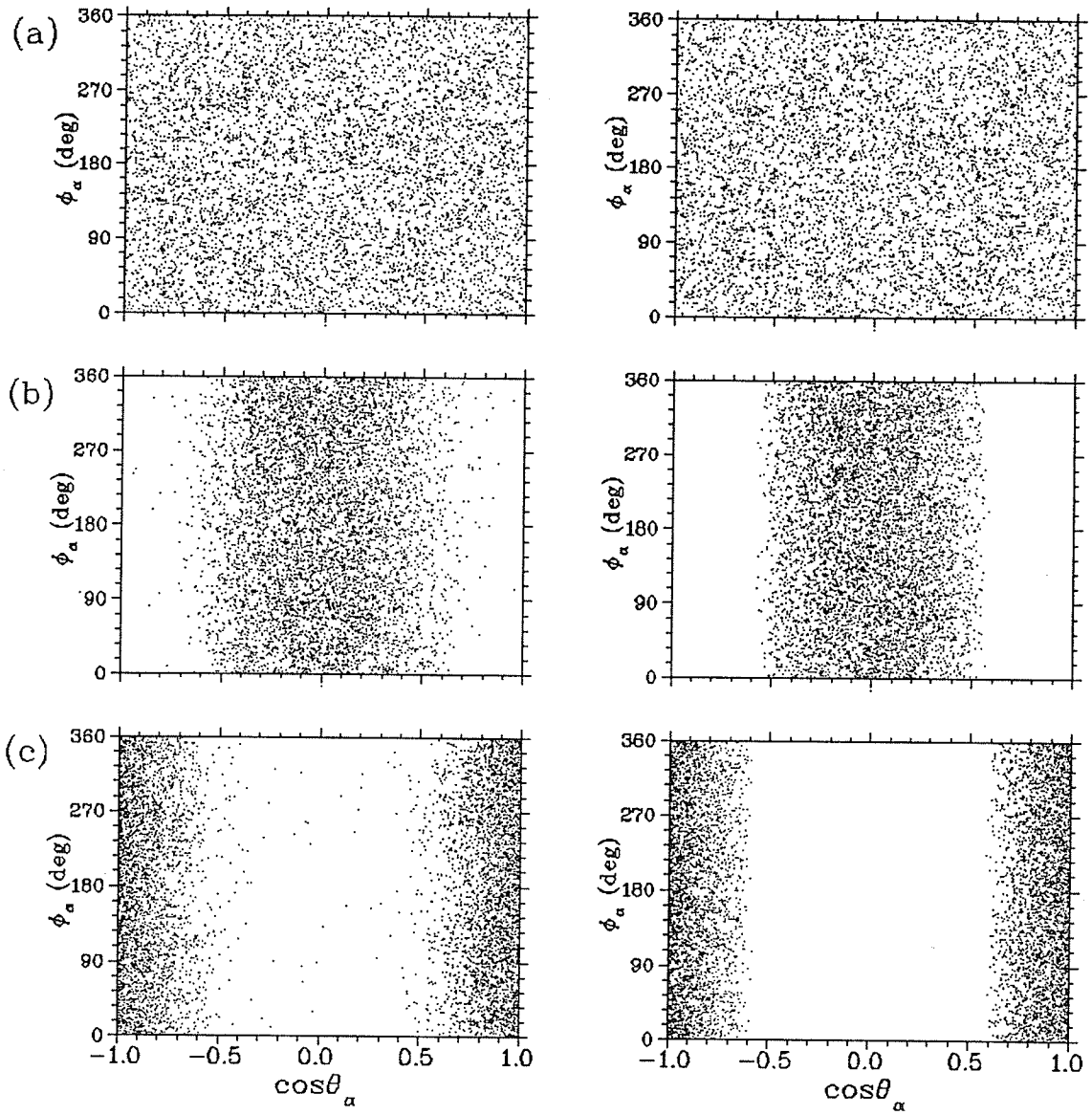

Figure 4.2: Event reconstruction distributions (left) and original distributions (right) for individual harmonic functions. (a): W_0, (b): $W_1(+)$, (c): $W_1(-)$

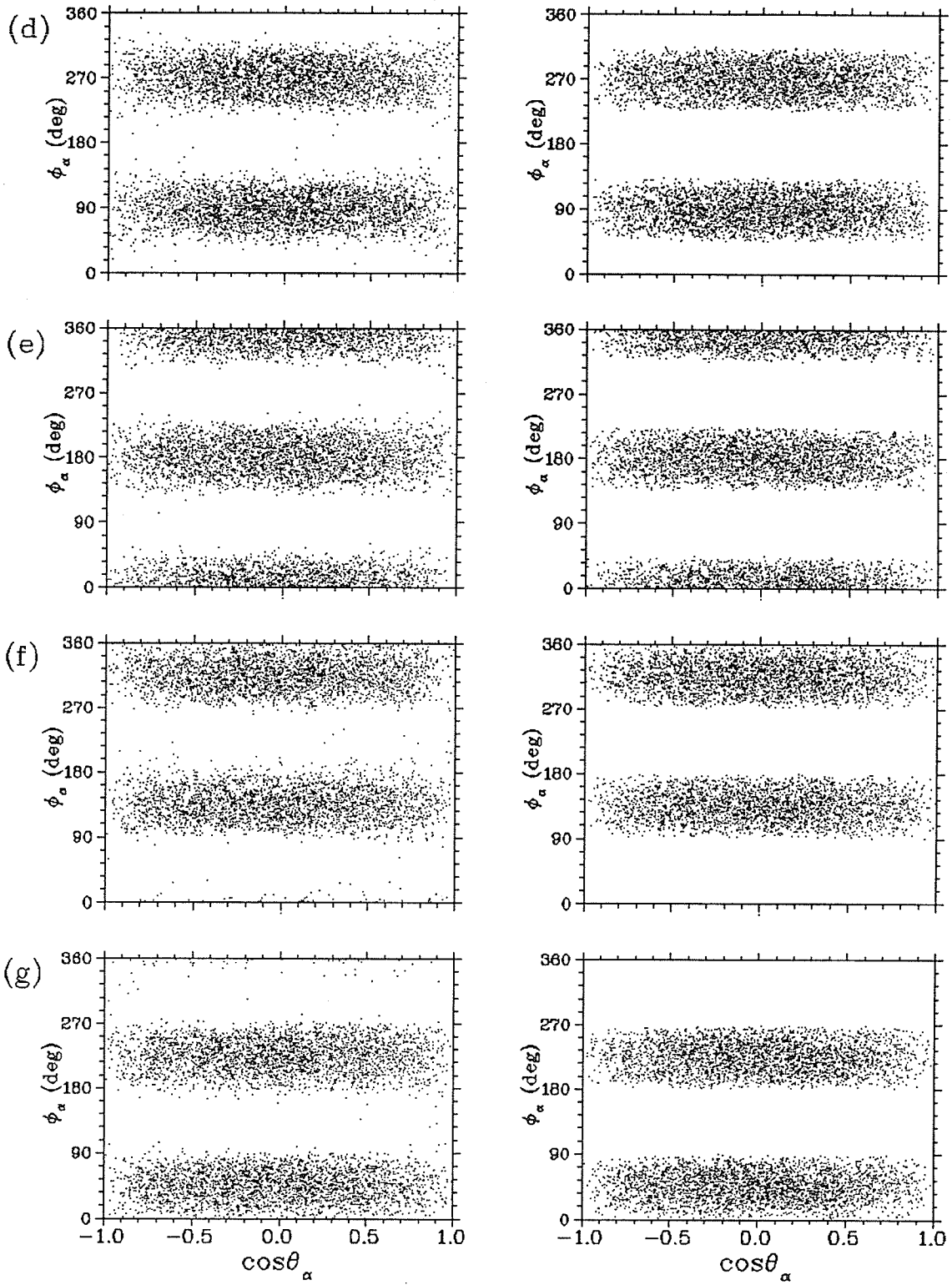

Figure 4.3: continuation of Fig 4.2 (d): $W_2(+)$, (e): $W_2(-)$, (f): $W_3(+)$, (g): $W_3(-)$

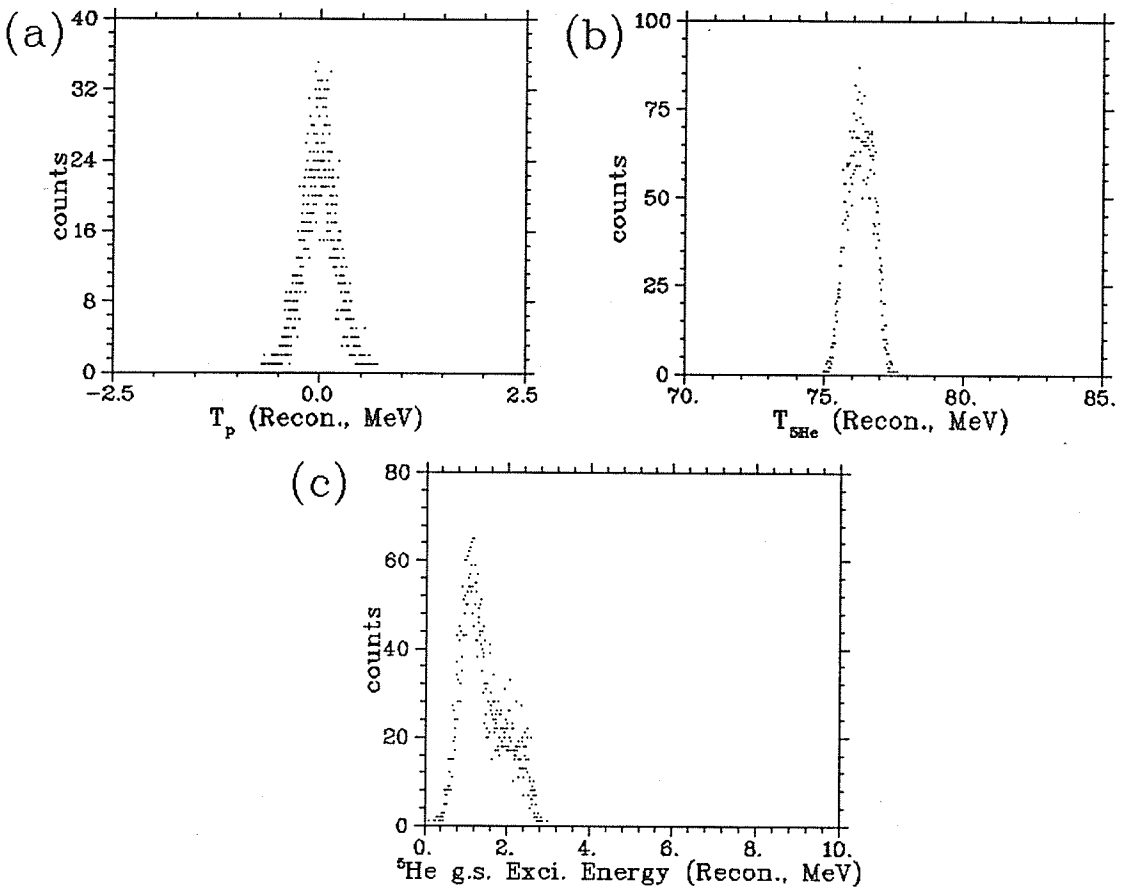

Figure 4.4: Reconstruction distributions for (a) T_p, (b) $T_{^5\mathrm{He}}$ and (c) ^{5}He g.s. Exci. Energy

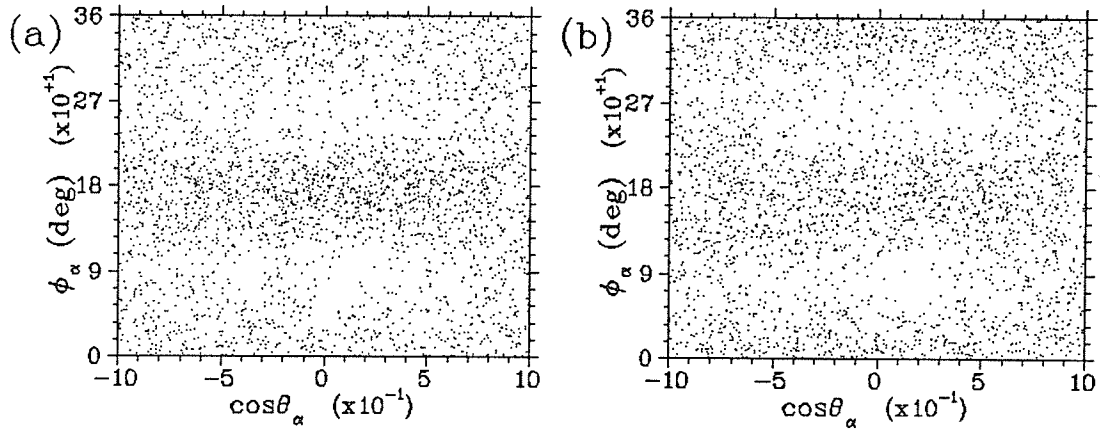

Figure 4.5: (a)Event reconstruction distribution of the SED and (b)the original $W(\theta, \phi)$ distribution at $(t_{20}, Re(t_{22}), Im(t_{22})) = (-0.2, -0.6, 0.2)$

4.2 Data Analysis Simulation

Following Fig. 2.2, by putting the prepared SIFDs and SCFD into the *fitting apparatus* simultaneously, we can now proceed with the process of extracting the tensors.

4.2.1 Event Number Normalization

Event number normalization accounts for the relationship between the number of the event counts for the full correlation function and that for each individual function.

Assume, as a practical example, a 1-Dimensional probability function

$$f(\psi) = 1 + k \sin \psi, \qquad \psi \in (0, 2\pi), k \leq 1,$$

is applied, and a counting distribution of $f(\psi)$ measured. (with total counts N). By generating (or 'simulating') each of the two individual functions $f_1(\psi) = 1$, $f_2(\psi) = \sin \psi$, the composite distribution can be fitted to the measured $f(\psi)$, and the parameter k extracted.

Since the integrated probability $\int f(\psi) d\psi = 2\pi$ receives net contributions from the 1st term or the uniform portion only, this quantity is proportional to the total number of counts, N, in the counting distribution for $f_1(\psi)$. Although for $f_2(\psi)$ the integral $\int f_2(\psi) d\psi = 0$, $f_2(\psi)$ affects the differential distribution. This counting distribution should be generated by a total number $2N/\pi$ (one half positive and the other negative, since $\int |f_2(\psi)| d\psi = 4$). Only then can the parameter k be extracted properly.

Figure 4.6 further illustrates this point.

Such normalization can be directly extended to the two dimensional case $W(\theta, \phi)$ (2.25). The probability integration $\int W(\theta, \phi) d\Omega = 4\pi$ comes only from the integration over the first isotropic term. Integration over any of the other three harmonic functions is 0.

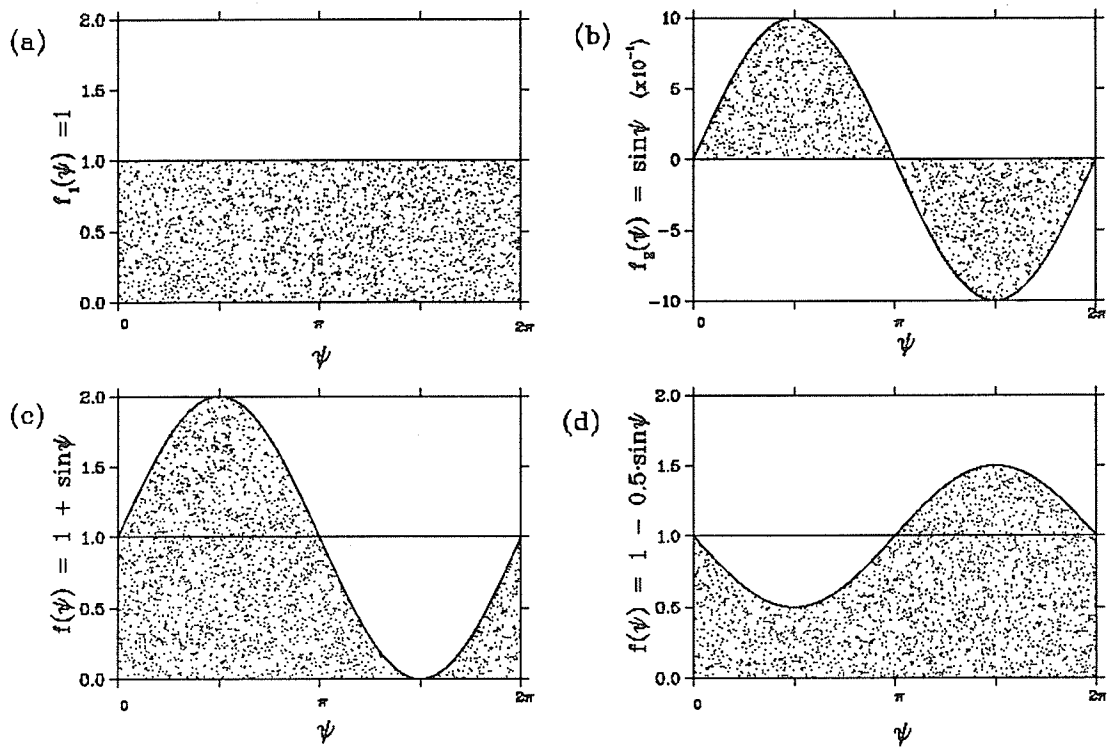

Figure 4.6: Example of Event counts normalization in 1 dimension

In generating the counting distribution for each individual harmonic function, the number of counts is proportional to the absolute probability integration enclosed by each, ie. $\int |w_i(\theta, \phi)| d\Omega (i = 0, 1, 2, 3)$, with half positive and half negative for w_1, w_2 and w_3. These integration values were tabulated in Table 4.1. One set of counts obtained from the Monte Carlo calculations for each individual function was also listed. After each set was normalized to its first term respectively, both sets were found very close in values.

4.2.2 Tensor Extraction Method

SCFD and SIFDs are distributed in the space of the recoil c.m. transverse system. Practically, the numerical range of the space $(\cos\theta_{cm}, \phi_{cm})$=(-1 to +1,0° − 360°) is divided into an array, with l_θ's bins for $\cos\theta_{cm}$ and l_ϕ's for ϕ_{cm}. The data prepared for an analysis simulation is in fact the SCFD and SIFDs recorded in

Table 4.1: Absolute Probability Integration of the Individual Harmonic Functions

	V_i $(\int \lvert W_i(\theta,\phi)\rvert d\Omega)$	$\frac{V_i}{V}$	N_i	$\frac{N_i}{N}$
W_0	4π	1	24627	1
W_1	$\frac{8\pi}{3\sqrt{3}}$	$\frac{2}{3\sqrt{3}}(\pm 0.1925)$	+4736	+0.1923
			-4741	-0.1925
W_2	$\frac{16}{3}\sqrt{\frac{3}{2}}$	$\frac{4}{3\pi}\sqrt{\frac{3}{2}}(\pm 0.2599)$	+6463	+0.2624
			-6434	-0.2613
W_3	$\frac{16}{3}\sqrt{\frac{3}{2}}$	$\frac{4}{3\pi}\sqrt{\frac{3}{2}}(\pm 0.2599)$	+6549	+0.2659
			-6495	-0.2637

this array (For SIFDs, the positive and the negative events are recorded together).

The details of how to bin the angular space is analyzed on §4.2.3.

The Maximum Likelihood Method

For counting distributions, the experimental values are Poisson distributed. Thus, if a mean of $Y^*(i)$ counts is expected in the i^{th} bin, the probability $P(i)$ of observing $N(i)$ in that bin is[35]

$$P(i) = (Y^*(i))^{N(i)} exp(-Y^*(i))/(N(i)!). \tag{4.5}$$

If the probabilities, $P(i)$, are uncorrelated, as is usually the case, the overall joint probability or likelihood function is

$$L = \prod_{i=1}^{n} P(i). \tag{4.6}$$

If the expected values, $Y^*(i)$, are obtained from a theory involving a number of undetermined parameters, a_k, those values of these parameters which yield a maximum in L are the best values to report. In order to maximize L it is more convenient to work with the logarithmic probability

$$W = \ln L = \sum_{i=1}^{n} [N(i) \ln Y^*(i) - Y^*(i) - ln(N(i)!)]. \tag{4.7}$$

W is an extremum when all the first order partial derivatives of W with respect to a_k (which define the theoretical curve) vanish. For m parameters, then, the set of equations

$$\partial W/\partial a_k = 0, \qquad k = 1, m, \tag{4.8}$$

have to be solved simultaneously, thus yield the best values a_k^*. For the Poisson distribution, the set of equations (4.8) turn out to be nonlinear and cannot be solved readily. Instead, iterative methods have to be applied for finding the solution.

Here in our specific case, $N(i)$ is the number of counts of the SCFD in the i^{th} bin of the c.m. transverse space (2D array) and

$$Y^*(i) = Y^*(i, \vec{a}) = \sum_{j=1}^{m=4} a_j Y_j^*(i), \qquad i = 1, 2, \cdots, n, \tag{4.9}$$

is the theoretical number of counts expected, with $\vec{a} = (a_1, a_2, a_3, a_4)$ the four statistical tensors to be determined and $Y_j^*(i)$ the counts in the i^{th} bin of the $j^{th}(j = 1, 4)$ SIFDs. $Y^*(i)$ is a linear function of $a_j(j = 1, 4)$.

The Least Squares Fitting

The iterative scheme employed involves the use of some initial estimates a_k^0 of all the parameters or tensors, and a first order Taylor series expansion of each of the partial derivatives (4.8) employing these initial estimates. Usually in the cases with reasonable statistics, the least square fitting is resorted to get these a_k^0.

The least-square function χ^2 now is[36]

$$\chi^2 = \sum_{i=1}^{n} \omega_i [N(i) - Y^*(i, \vec{a})]^2, \tag{4.10}$$

where ω_i is the statistical weight for the experimental counts $N(i)$ and can be approximated by

$$\omega_i = \frac{1}{\sigma_i^2} \simeq \frac{1}{N(i)}. \tag{4.11}$$

Now from

$$\chi^2 = min, \qquad or \qquad \partial\chi^2/\partial a_k = 0, \qquad k = (1, m), \tag{4.12}$$

one obtains the equations:

$$\sum_{i=1}^{n} \omega_i [N(i) - Y^*(i, \vec{a})] \partial Y^*(i, \vec{a}) / \partial a_k = 0, \qquad k = (1, m). \tag{4.13}$$

With (4.9) substituted into (4.13), this yields

$$\sum_{j=1}^{m} (\sum_{i=1}^{n} \omega_i Y_k^*(i) Y_j^*(i)) a_j = \sum_{i=1}^{n} Y_k^*(i), \qquad k = (1, m),$$

or in matrix form,

$$\mathbf{M}\hat{\mathbf{a}} = \mathbf{B}, \tag{4.14}$$

where

$$M_{kj} = \sum_{i=1}^{n} \omega_i Y_k^*(i) Y_j^*(i), \tag{4.15}$$

$$B_k = \sum_{i=1}^{n} Y_k^*(i). \tag{4.16}$$

Hence (4.14) yields the estimates

$$\hat{\mathbf{a}} = \mathbf{M}^{-1}\mathbf{B}. \tag{4.17}$$

The covariance error matrix for $\hat{\mathbf{a}}$ is

$$\mathbf{V}_{\hat{\mathbf{a}}} = \mathbf{M}^{-1}. \tag{4.18}$$

In this matrix, if the j^{th} diagonal element is much bigger than adjacent non-diagonal elements, ie. if there is little correlation between the parameters, then its square root can be taken as the statistical error for the estimation of a_j.

The Iteration Process of Maximum Likelihood

Now with the initial values $a_k^0 = \hat{\mathbf{a}}$, we make a first order expansion to $(\frac{\partial W}{\partial a_k})_{a_k^*(k=1,m)}$ at a_k^0 :

$$0 = (\frac{\partial W}{\partial a_k})_{(a_k^*, k=1,m)} \tag{4.19}$$

$$= (\frac{\partial W}{\partial a_k})_{(a_k^0, k=1,m)} + \sum_{j=1}^{m} [\frac{\partial^2 W}{\partial a_k \partial a_j} \cdot \Delta a_j]_{(a_k^0, a_j^0, k,j=1,m)}, \tag{4.20}$$

where $\Delta a_j = a_j^* - a_j^0$. In this way the simultaneous equations (4.8) reduce to a set of m linear equations represented by the matrix equations

$$\mathbf{CA} = \mathbf{V}, \tag{4.21}$$

where

$$C_{kj} = [\frac{\partial^2 W}{\partial a_k \partial a_j}]_{(a_k^0, a_j^0, k,j=1,m)}, \tag{4.22}$$

$$A_k = \Delta a_k, \tag{4.23}$$

$$V_k = -(\frac{\partial W}{\partial a_k})_{(a_k^0, k=1,m)}. \tag{4.24}$$

Solutions of the expansion equations (4.21) then yield the first order corrections Δa_k or $\mathbf{A} = \mathbf{C^{-1}V}$, which, when added to the initial estimates a_k^0, yield an improved set of a_k which may again be used in the equations to yield a still better set .

For Poisson statistics in the case of (4.9), the $m \times m$ matrix $\mathbf{C}$ contains the elements

$$C_{kj} = \sum_{i=1}^{n}[(\frac{N(i)}{Y^*(i)} - 1)\frac{\partial^2 Y^*(i)}{\partial a_k \partial a_j} - \frac{N(i)}{Y^{*2}(i)} \cdot \frac{\partial Y^*(i)}{\partial a_k} \cdot \frac{\partial Y^*(i)}{\partial a_j}] = \sum_{i=1}^{n}[-\frac{N(i)}{Y^{*2}(i)} Y_k^*(i) Y_j^*(i)]. \tag{4.25}$$

The vector $\mathbf{V}$ is

$$V_k = -\sum_{i=1}^{n}(\frac{N(i)}{Y^*(i)} - 1)\frac{\partial Y^*(i)}{\partial a_k} = -\sum_{i=1}^{n}(\frac{N(i)}{Y^*(i)} - 1) Y_k^*(i). \tag{4.26}$$

Here it should be noted that V_k is just the first partial derivative of W with respect to a_k. When the maximum likelihood point is reached, V_k should consequently vanish, and matrix $-\mathbf{C^{-1}}$ at this point represents the covariant error matrix for the maximum likelihood estimations.

4.2.3 Record Arrays for SIFDs and SCFD

In proceeding to do the fitting, we need to consider, in advance, in which way the space $(\cos\theta_{cm}, \phi_{cm})$=(-1 to +1, $0° - 360°$) is binned to record the SIFD's and SCFD. Let us consider the correlation function (2.25). $W(\theta, \phi) \geq 0$ requires that

the negative counts from one individual distribution within a certain solid angle should be cancelled by the positive counts from other individual distributions.

To see the point, we generated a *pure mathematical* distribution for $W(\theta, \phi)$ with $(t_{20}, Re(t_{22}), Im(t_{22})) = (-0.2, -0.6, 0.2)$, comprising the individually generated functions. Putting these non-instrumental counting distributions into the *Fitting Apparatus*, we extracted the *'tensors'* (coefficients actually). We found that at all zero-borders (See Fig. 4.2 and Fig. 4.3), where one or more individual functions change signs, like $W_1(\theta, \phi)$ at $\cos\theta = \pm\frac{\sqrt{3}}{3}$ and $W_2(\theta, \phi)$ or $W_3(\theta, \phi)$ at $\phi = k \cdot 45°$ $(k - integer)$, the bins should be cut exactly along these borders, in order to prevent counts of one sign cancelling those of the opposite sign for the same individual distribution. In this way, the extracted values agreed with the input values within statistical errors.

Since SCFD and SIFDs contain the salient features of those *pure mathematical* distributions they originated from (a SCFD and its mathematical origination are shown in Fig. 4.7), the space can be binned in the same way. Note that since many instrumental effects were involved in the Monte Carlo and Event Reconstruction calculations, the counts of SIFDs recorded in the bins near the zero-borders still cancel to a small degree (In effect, such count cancellations reduced the probability integration $\int |w_i(\theta, \phi)| d\Omega$). With relatively denser binning along all zero-borders, we expect to minimize the amount of cancellation.

Five bin arrays are applied in recording the data and in verifying the fitting results, goodness of fit and errors. They are listed in Table 4.2, in which under $\Delta \cos\theta_{cm}$, the numbers listed are actually the borders of the bins in (0 to 1), for example, 0 to $\frac{\sqrt{3}}{3}$-.4 represents a bin, and $\frac{\sqrt{3}}{3}$-.4 to $\frac{\sqrt{3}}{3}$-.25 represents another bin, and so on. (-1 to 0) was binned symmetrically to (0 to 1).

4.2.4 Fitting Results, Goodness of Fit and Errors

In the Monte Carlo simulation, we have set the upper limit on the ^{5}He(g.s.) excitation energy at 3.3 MeV, and pion detector (MRS) acceptances of (H: $\pm 0.8°$,

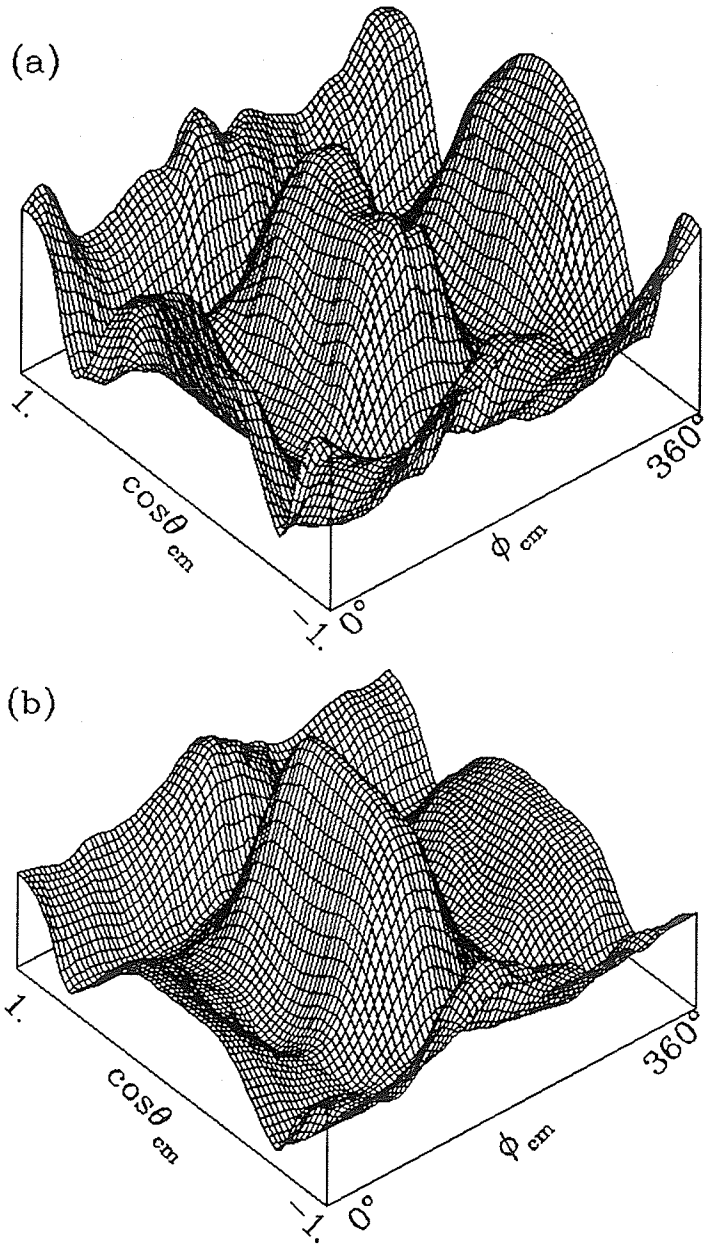

Figure 4.7: (a) The *pure mathematical* (ie. no instrumental effect) distribution of the correlation function (b) The SCFD, both at $(t_{20}, Re(t_{22}), Im(t_{22}))$ = (-0.2,-0.6,0.2)

Table 4.2: Five Record Arrays

l_θ	l_ϕ	$\Delta\cos\theta^{\dagger}_{cm}$										$\Delta\phi_{cm}$
18	32	0	$\frac{\sqrt{3}}{3}$-.4	$\frac{\sqrt{3}}{3}$-.25	$\frac{\sqrt{3}}{3}$-.15	$\frac{\sqrt{3}}{3}$-.05	$\frac{\sqrt{3}}{3}$	$\frac{\sqrt{3}}{3}$+.05	$\frac{\sqrt{3}}{3}$+.15	$\frac{\sqrt{3}}{3}$+.25	1	$11\frac{1}{4}°$
16	14	0	$\frac{\sqrt{3}}{3}$-.35	$\frac{\sqrt{3}}{3}$-.15	$\frac{\sqrt{3}}{3}$-.05	$\frac{\sqrt{3}}{3}$	$\frac{\sqrt{3}}{3}$+.05	$\frac{\sqrt{3}}{3}$+.2	1			$22\frac{1}{2}°$
8	12	0	$\frac{\sqrt{3}}{3}$-.3	$\frac{\sqrt{3}}{3}$-.1	$\frac{\sqrt{3}}{3}$	$\frac{\sqrt{3}}{3}$+.1	$\frac{\sqrt{3}}{3}$+.25	1				45°
8	8	0	$\frac{\sqrt{3}}{3}$-.2	$\frac{\sqrt{3}}{3}$	$\frac{\sqrt{3}}{3}$+.2	1						45°
8	4	0	$\frac{\sqrt{3}}{3}$	1								45°

†: listed are the borders of the bins(for e.g., 0 to $\frac{\sqrt{3}}{3}$-0.4 is a bin), (0 to -1) is symmetrically binned.

V: $\pm 2.5°$) (See Table 3.1). The corresponding α position distributions for both individual and full functions are shown in Fig. 3.16, Fig. 3.17 and Fig. 3.19 respectively. Such distributions require a detector of acceptances (H: $\pm \sim 8.5cm$, V: $\pm \sim 10.4cm$) for measurements. Our detector ($SASP$) has acceptances of (H: $\pm 2.4°$, V: $\pm 5.9°$), that is (H: $\pm 4.2cm$, V: $\pm 10.3cm$) at the distance of $100cm$ from the target.

In the following sections, first we will still perform the tensor extractions with full α acceptance, ie. assuming the detector large enough to accept all of the α particles correlated with the accepted pions. Then we will check the influence on the extracted values if two horizontal settings of SASP measurements are taken which almost cover the horizontal distribution.

Full α Acceptance

We calculate the SCFD samples for $(t_{20}, Re(t_{22}), Im(t_{22})) = (-0.2, -0.6, 0.2)$ for five different values of total counts listed in Table 4.3. The four SIFDs corresponding to each SCFD are also calculated.

For each of the five different cases, the SCFD and the SIFDs are recorded, simultaneously, to five different bin arrays tabulated in Table 4.2 to produce the input data for fittings with different record arrays. On recording, the positive and negative counts cancel to a small degree by amounts which differ from array to array.

Table 4.3: Fitting Results for full α acceptance (5 Counts, 5 Arrays), to be continued

SCFD Counts	Record Array	t_{00}	t_{20}	$Re(t_{22})$	$Im(t_{22})$	$\frac{\chi^2}{\nu}$
6034	8 × 4	1.007 ±0.013	-0.145 ±0.033	-0.534 ±0.022	0.167 ± 0.023	2.73
	8 × 8	1.006 ±0.013	-0.199 ±0.030	-0.524 ±0.021	0.155 ± 0.022	2.71
	8 × 12	1.006 ±0.013	-0.186 ±0.029	-0.520 ±0.021	0.154 ±0.022	2.84
	16 × 14	1.006 ±0.012	-0.199 ±0.028	-0.530 ±0.018	0.185 ±0.019	3.03
12194	8 × 4	1.006 ±0.009	-0.165 ±0.024	-0.599 ±0.016	0.224 ± 0.016	1.97
	8 × 8	1.006 ±0.009	-0.176 ±0.022	-0.598 ±0.016	0.224 ± 0.016	2.34
	8 × 12	1.006 ±0.009	-0.161 ±0.021	-0.599 ±0.015	0.228 ±0.016	2.77
	16 × 14	1.006 ±0.009	-0.175 ±0.021	-0.583 ±0.014	0.208 ±0.014	2.80
	32 × 18	1.006 ±0.009	-0.174 ±0.016	-0.620 ±0.013	0.192 ±0.013	2.86
24627	8 × 4	1.003 ±0.006	-0.195 ±0.017	-0.582 ±0.011	0.202 ±0.011	2.02
	8 × 8	1.003 ±0.006	-0.200 ±0.016	-0.577 ±0.011	0.202 ± 0.011	2.13
	8 × 12	1.003 ±0.006	-0.203 ±0.015	-0.577 ±0.011	0.202 ±0.011	2.36
	16 × 14	1.003 ±0.006	-0.203 ±0.015	-0.564 ±0.010	0.200 ±0.010	2.79
	32 × 18	1.003 ±0.006	-0.236 ±0.015	-0.587 ±0.009	0.191 ±0.009	3.12

Table 4.3, continued

SCFD Counts	Record Array	t_{00}	t_{20}	$Re(t_{22})$	$Im(t_{22})$	$\frac{\chi^2}{\nu}$
37008	8 × 4	1.002 ±0.005	-0.193 ±0.014	-0.593 ±0.009	0.203 ± 0.010	1.59
	8 × 8	1.002 ±0.005	-0.196 ±0.013	-0.592 ±0.009	0.202 ±0.009	1.58
	8 × 12	1.000 ±0.005	-0.193 ±0.012	-0.588 ±0.009	0.201 ±0.009	2.30
	16 × 14	1.000 ±0.005	-0.193 ±0.012	-0.581 ±0.008	0.195 ±0.008	2.31
	32 × 18	1.000 ±0.005	-0.192 ±0.012	-0.600 ±0.008	0.194 ±0.008	2.31
49555	8 × 4	1.004 ±0.005	-0.207 ±0.012	-0.608 ±0.008	0.206 ±0.008	1.840
	8 × 8	1.004 ±0.005	-0.208 ±0.011	-0.609 ±0.008	0.207 ±0.008	2.07
	8 × 12	1.004 ±0.005	-0.211 ±0.011	-0.608 ±0.008	0.208 ±0.008	2.57
	16 × 14	1.004 ±0.005	-0.202 ±0.011	-0.595 ±0.007	0.206 ±0.007	2.57
	32 × 18	1.004 ±0.005	-0.195 ±0.011	-0.573 ±0.007	0.190 ±0.007	2.45

Table 4.4: The example of SIFDs counts cancellation (full α acceptance, record array 16×14)

	N_+	N_-	N_{cancel}	$\frac{2N_{cancel}}{N_+ + N_-}(\%)$	N_{+net}	N_{-net}
W_0	37114	0	0	0	37114	0
W_1	7276	-7131	538	7.469	6738	-6593
W_2	9668	-9553	999	10.395	8669	-8554
W_3	9438	-9555	771	8.119	8667	-8784

Table 4.5: The example of the fitting results (full α acceptance, SCFD counts 37008)

Record Array	t_{00}	t_{20}	$Re(t_{22})$	$Im(t_{22})$	Iteration numbers	$\frac{\chi^2}{\nu}$
16×14	0.987	-0.196	-0.593	0.204	0	
	1.000	-0.195	-0.582	0.196	1	
	1.000	-0.193	-0.581	0.195	2	
	1.000	-0.193	-0.581	0.195	3	2.31
	± 0.005	± 0.012	± 0.008	± 0.008		

For example, Table 4.4 lists the cancelled counts when the SIFDs, corresponding to the SCFD with total counts 37008, are recorded in a 16×14 array. Also listed are the cancelled percentages and the net counts.

Next we perform the tensor extractions by fitting each SCFD with its corresponding SIFDs for all of the 5 different records. As an example, Table 4.5 gives the result when SCFD, with total counts 37008 recorded in a 16×14 array, is fitted with the SIFDs with counts listed in Table 4.4. The first line comes from the least-square fitting and the following lines from the iterations of the maximum likelihood method.

A summary of all the extracted results are listed in Table 4.3. For SCFD with 6034 counts recorded in an array 32×18, the tensors could not be extracted because in a few bins the counts were 0.

Table 4.6: Example of the covariant error matrix, SCFD counts 37008, Record Array 16 × 14

Cov.	$t_{00})$	$t_{20})$	$Re(t_{22}))$	$Im(t_{22}))$
$(t_{00},$	0.0000267	-0.0000058	-0.0000161	0.0000057
$(t_{20},$	-0.0000058	0.0001528	-0.0000270	0.0000103
$(Re(t_{22}),$	-0.0000161	-0.0000270	0.0000650	0.0000008
$(Im(t_{22}),$	0.0000057	0.0000103	0.0000008	0.0000677

In the final covariant error matrix from each fitting, the diagonal elements are much larger than their adjacent non-diagonal elements. To see the point, Table 4.6 gives an example. The errors listed in Table 4.5 or Table 4.3 are the square root of these diagonal elements. We may find that the fewer the SCFD counts and the smaller the record arrays, the bigger are these statistical errors.

Generally, the greater the SCFD counts, the closer the extracted tensors are to the input values. For fewer SCFD counts (e.g., 6034), the differences are obviously outside of the statistical errors. On the other hand for better statistics, as represented by the last three cases, the differences get closer to the statistical errors. This might be because the count cancellations in SIFDs become less important for cases with greater counts.

In order to assess the goodness -or otherwise- of the fit, the χ^2 test is incorporated in the fitting program. With the degrees of freedom n-4, the $\frac{\chi^2}{\nu}$ values calculated are also listed in Table 4.3. Generally speaking, for a given number of total counts, the smaller the record arrays the smaller the $\frac{\chi^2}{\nu}$ value since there are more counts in fewer bins making the counting distributions more effectively Gaussian. Although a little bigger than usually expected from a good fit, these $\frac{\chi^2}{\nu}$ values are acceptable, especially in the cases of greater SCFD counts. The count cancellations, which can generate a kind of non-statistical error, may still be the cause of the non-perfect fit.

In Fig. 4.8, one SCFD (counts 37008) and its fitted distributions are shown

Table 4.7: Tensors extracted by fitting SCFD with the pure mathematical individual distributions

SCFD Counts	Record Array	t_{00}	t_{20}	$Re(t_{22})$	$Im(t_{22})$	$\frac{\chi^2}{\nu}$
37008	32 x 18	1.000 ±0.005	-0.120 ±0.011	-0.550 ±0.007	0.169 ±0.007	6.31
	16 x 14	1.000 ±0.005	-0.121 ±0.012	-0.566 ±0.008	0.181 ±0.007	11.49
	8 x 12	1.000 ±0.005	-0.116 ±0.001	-0.585 ±0.009 ±0.008	0.188	20.77

and they look quite similar. Also shown in Fig. 4.9 and Fig. 4.10 are distributions of the same data but recorded in arrays 32×18 and 8×12 respectively. Fig. 4.9 reveals more detailed structure while Fig. 4.10 shows somewhat less detail than Fig. 4.8.

As an alternative test for the validity of SIFDs, we try to fit SCFD with the *pure mathematical* individual distributions. Fittings results are listed in Table 4.7 for SCFD counts 37008. Corresponding results are also extracted for the other SCFD's.

We find that although no counts cancel in the *pure mathematical* distributions, they do not involve any of the instrumental effects as those of the SIFD's do and therefore very poor fitted values result in unacceptably large $\frac{\chi^2}{\nu}$-values.

Limited α Acceptance

A few α particles from large excitation breakup will not be recorded in the detector. For each SIFD, before being recorded in the 5 different arrays, both positive and negative counts may be lost. The counts lost depend not only on the dimensions of the detector acceptance but also on the individual harmonic function form. From Fig. 3.16 and Fig. 3.17 we see that if two settings of SASP measurements were taken, then $W_0, W_1(+), W_2(+)$ and $W_3(+)$ would suffer losses due to horizontal restrictions and $W_3(-)$ due to vertical restrictions. Then when we record both the positive and the negative counts in their arrays some further can-

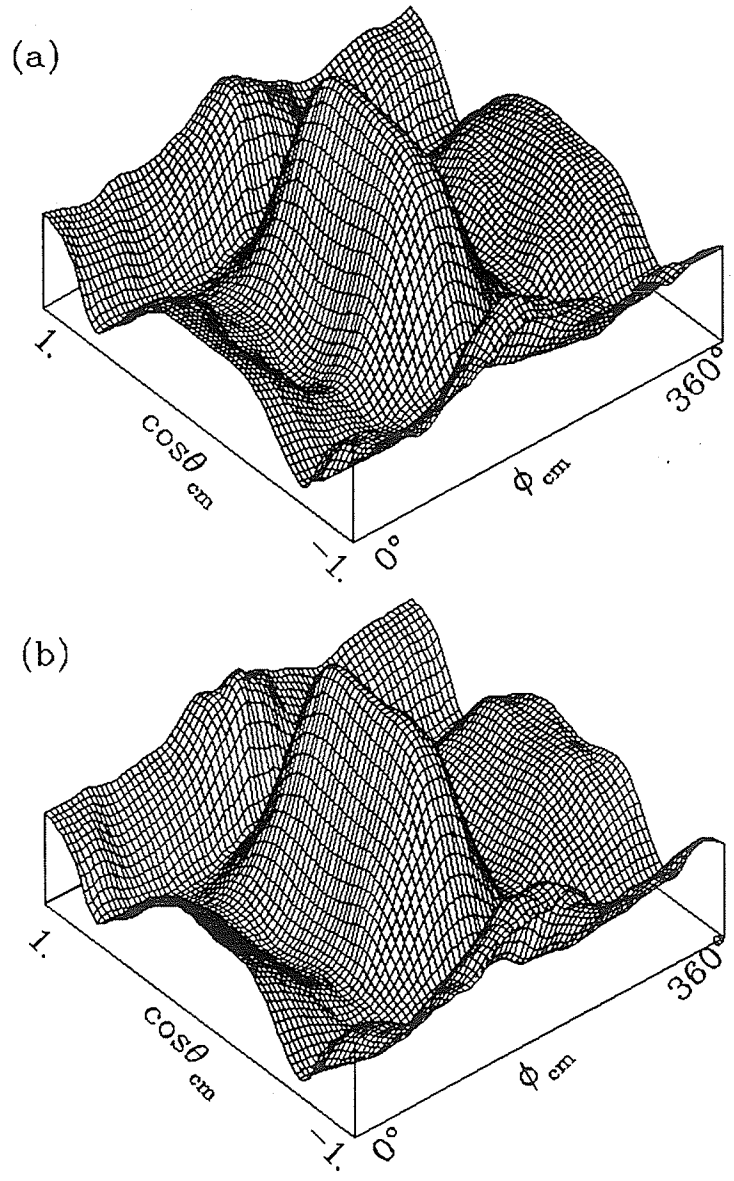

Figure 4.8: The distributions of (a): the SCFD; (b) the fitted data recorded in a 16×14 array

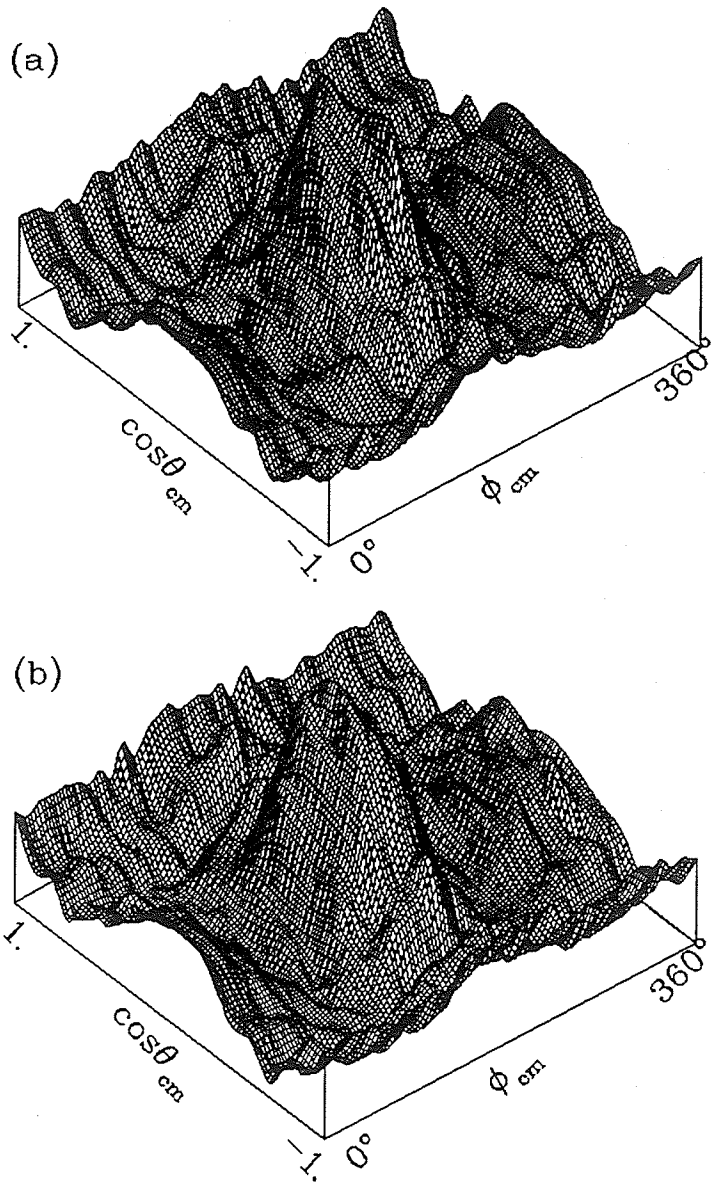

Figure 4.9: The distributions of (a): the SCFD; (b) the fitted data; recorded in a 32×18 array

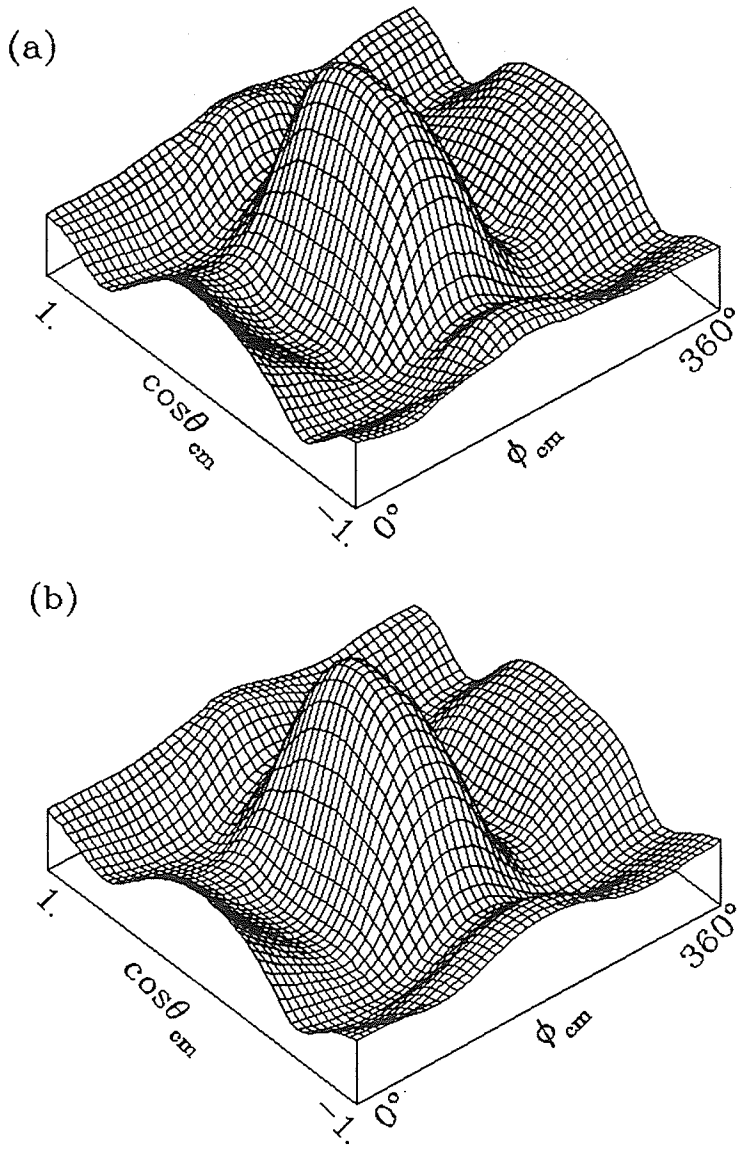

Figure 4.10: The distributions of (a): the SCFD; (b) the fitted data; recorded in a 8×12 array

Table 4.8: The SIFDs Counts (Limited α Acceptance, Record Array 16 × 14)

	N_+	N_-	$N_{+loss}(\%)$	$N_{-loss}(\%)$	N_{+left}	N_{-left}	N_{cancel}	$\frac{2N_{cancel}}{N_+ + N_-}(\%)$	N_{+net}	N_{-net}
W_0	37114	0	387(1.04)	0 (0)	36727	0	0	0	36727	0
W_1	7276	-7131	144(1.98)	-34(0.48)	7132	-7097	534	7.51	6598	-6563
W_2	9668	-9553	331(3.42)	-11(0.12)	9337	-9542	993	10.52	8344	-8549
W_3	9438	-9555	86(0.91)	-92(0.96)	9352	-9463	739	7.86	8613	-8724

Table 4.9: Fitting Results (Limited α Acceptance, SCFD counts 36852)

Array	t_{00}	t_{20}	$Re(t_{22})$	$Im(t_{22})$	Iteration numbers	$\frac{\chi^2}{\nu}$
32 × 18	0.987	-0.204	-0.598	0.204	0	
	1.000	-0.200	-0.587	0.196	1	
	1.001	-0.198	-0.585	0.195	2	
	1.001	-0.198	-0.585	0.195	3	2.33
	±0.005	±0.012	±0.008	± 0.008		

cellation occurs. Table 4.8 lists the lost counts corresponding to those total counts listed in Table 4.4.

Table 4.9 gives the corresponding fitted values, which are very close to those values in Table 4.5

Hence in Table 4.10 we only list the fitting results for the first three SCFD counts corresponding to those listed in Table 4.3. We see that the lost counts only influence the tensor extractions for total counts ~6000. When the total counts increase to ~ 12000, the differences with those values listed in Table 4.3 become negligible.

4.3 Alternate Reference Frames

In the recoil c.m. helicity system, the correlation function is

$$\mathrm{W^H}(\theta,\phi) = 1 - \frac{1}{2}(3\cos^2\theta - 1)\cdot \mathrm{t}_{20} + \sqrt{6}\sin\theta\cos\theta\cos\phi\cdot \mathrm{t}_{21} - \sqrt{\frac{3}{2}}\sin^2\theta\cos 2\phi\cdot \mathrm{t}_{22}. \quad (4.27)$$

Table 4.10: Fitting Results for limited α acceptance (3 Counts, 5 Arrays)

SCFD Counts	Record Array	t_{00}	t_{20}	$Re(t_{22})$	$Im(t_{22})$	$\frac{\chi^2}{\nu}$
5990	8 × 4	1.004 ±0.013	-0.140 ±0.033	-0.534 ±0.022	0.166 ± 0.023	2.88
	8 × 8	1.004 ±0.013	-0.189 ±0.030	-0.521 ±0.021	0.154 ± 0.022	2.81
	8 × 12	1.004 ±0.013	-0.178 ±0.029	-0.524 ±0.021	0.155 ±0.022	2.84
	16 × 14	1.003 ±0.012	-0.170 ±0.028	-0.562 ±0.019	0.183 ±0.019	2.99
12120	8 × 4	1.006 ±0.009	-0.165 ±0.024	-0.600 ±0.016	0.227 ± 0.016	1.98
	8 × 8	1.006 ±0.009	-0.172 ±0.022	-0.598 ±0.016	0.225 ± 0.016	2.38
	8 × 12	1.006 ±0.009	-0.158 ±0.021	-0.602 ±0.015	0.229 ±0.016	2.71
	16 × 14	1.006 ±0.009	-0.170 ±0.021	-0.581 ±0.014	0.204 ±0.014	2.74
	32 × 18	1.006 ±0.009	-0.150 ±0.020	-0.631 ±0.013	0.221 ±0.013	2.77
24577	8 × 4	1.004 ±0.006	-0.195 ±0.018	-0.583 ±0.011	0.205 ±0.011	2.04
	8 × 8	1.004 ±0.006	-0.199 ±0.016	-0.577 ±0.011	0.203 ± 0.011	2.13
	8 × 12	1.004 ±0.006	-0.204 ±0.016	-0.578 ±0.011	0.203 ±0.011	2.39
	16 × 14	1.004 ±0.006	-0.201 ±0.015	-0.564 ±0.010	0.197 ±0.010	2.81
	32 × 18	1.003 ±0.006	-0.225 ±0.015	-0.593 ±0.009	0.223 ±0.009	3.11

Table 4.11: The fitted Tensors in Helicity Frame

SCFD counts	Array	t_{00}^H	t_{20}^H	t_{21}^H	t_{22}^H	$\frac{\chi^2}{\nu}$
37008	32 × 18	1.005 ±0.005	-0.565 ±0.013	-0.197 ±0.009	0.386 ±0.009	2.64
	16 × 14	1.005 ±0.005	-0.615 ±0.013	-0.194 ±0.009	0.414 ±0.009	2.40
	8 × 12	1.005 ±0.005	-0.626 ±0.013	-0.204 ±0.009	0.430 ±0.009	2.18

with t_{20}, t_{21}, t_{22} all real. An alternative way for extracting this set of tensor values exists. As shown in Fig. 4.11, the method is identical to that in the recoil c.m. transverse frame with distribution (2.25) except that the *Target Reconstruction Apparatus* (TRA) here is just one part of the TRA in Fig. 2.2 (where a further transformation should be made from the helicity frame to the transverse frame). Passing the SIFDs and SCFD in either frame through the common *Fitting Apparatus*, both sets of tensors can be extracted.

A sample of *Simulated Experimental Data* (SED) can be produced in the same way as that introduced in §3.5, either with correlation function (4.27) or (2.25). If (4.27) is applied, then the set of tensor values (t_{20}, t_{21}, t_{22}) should also meet the two positivity requirements described in §3.5.

Event reconstruction for the Simulated Experimental Data (SED, generated in §3.5) within the recoil c.m. helicity frame gives the SCFDs in this frame. (A further transformation from this frame to the transverse frame yields those SCFDs in §4.2.4.) Fitting the SCFDs with the SIFDs generated for individual functions in the helicity frame, we extracted the tensors directly. Some of the values are listed in Table 4.11 for three different bin arrays.

On the other hand, by applying the rotation facility as described in Appendix A, we can transform the tensors extracted in the transverse frame to the helicity frame via Euler angles $(\alpha, \beta, \gamma) = (0, 90°, 90°)$. The details are listed in Ta-

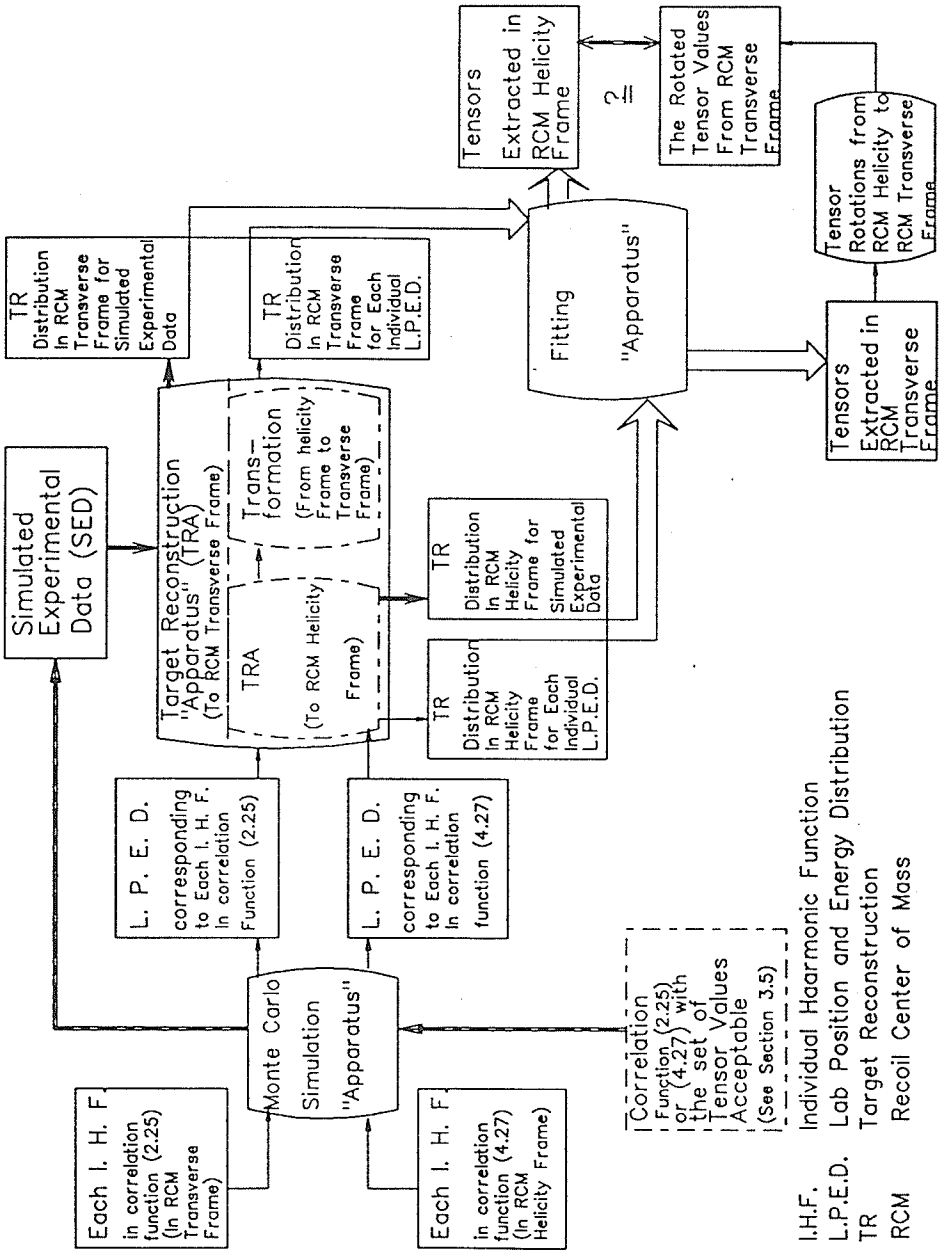

Figure 4.11: The Block Diagram of Tensor Extractions in the Alternate Frames

Table 4.12: Tensor Rotations from Transverse to Helicity Frame

t^H_{00}	t^H_{20}	t^H_{21}	t^H_{22}
t^T_{00}	$\frac{\sqrt{6}}{2}Re(t_{22})^T - \frac{t^T}{2}$	$-Im(t_{22})^T$	$-\frac{Re(t)}{2} - \frac{\sqrt{6}}{4}t^T_{20}$
1.0	-0.635	-0.2	0.430

ble 4.12, and the last line gives the values calculated for $(t_{20}, Re(t_{22}), Im(t_{22})) = (-0.2, -0.6, 0.2)$ in the transverse frame.

This serves as a check that the tensor values extracted directly in the helicity frame do, indeed, agree with those rotated from the transverse frame. Fig. 4.12 shows the fitted distributions in a schematic view.

4.4 An Alternative Arrangement of the Experiment

In a preliminary planning for the coincidence experiment, we decided to use the MRS for detecting π^+ and SASP for the α-particles. An alternative arrangement was also considered as well, which would use an array of solid state position sensitive detectors (PSD) for the α-particles and SASP for π^+ detection instead. The former arrangement employs the two convenient facilities and, in addition, SASP's Dipole could eliminate the intense forward scattered protons. The disadvantage is that its vertical opening limits the acceptance of large excitation energy breakup, even though horizontally we can move SASP to scan the whole break up region. The alternative method could offer the acceptance needed. However, constructing the PSD arrays involves a lot of development work and besides, the heavy *flux* of scattered protons on the detector array results in a count rate problem.

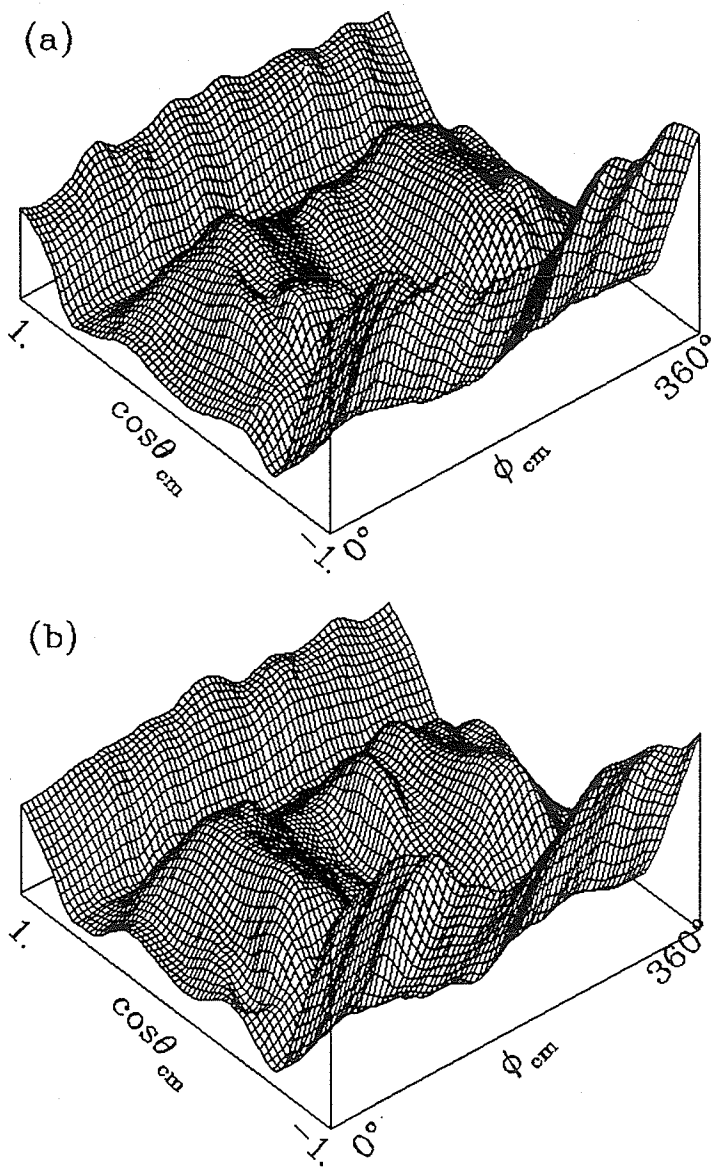

Figure 4.12: The distributions of (a): the SCFD; (b) the fitted data; recorded in a 16×14 array in helicity frame

If the PSD array is to be built and put into use in such an experiment, then the maximum uncertainty in obtaining the α position information would be half the dimension of each array element. This position uncertainty had a strong influence on the angular distribution after event reconstruction.

We assume that a PSD array is $12 \times 12cm^2$, and that it may consist of elements with sizes $0.5\times0.5cm^2$, 1.0×1.0, $\cdots$, or $6.0\times6.0cm^2$. Fig. 4.13 gives the event reconstruction distributions in a few cases, with case (a) of $1.0\times1.0cm^2$ still comparable with Fig. 4.5(a). Generally, the bigger the element size, the more the distribution deviates from Fig. 4.5(a).

The fitting results are related not only to the PSD element size but also to the $\cos\theta_{cm} - \phi_{cm}$ arrays further used to record the event reconstruction data. Four different bin arrays were used to record the reconstruction data from each of the four cases in Table 4.13, in which a summary of the extracted values were tabulated for a SCFD of 8737 counts fitted with SIFDs relating each of the 16 cases. From the table, we see that even using the PSD with elements $4 \times 4cm^2$, one can still obtain reasonable results.

Finally, It should be noted that a PSD with different element size did not influence the reconstruction of the ^{5}He g.s. excitation energy since as we discussed in §4.1.1, information from the π^+ and the proton permits its calculation.

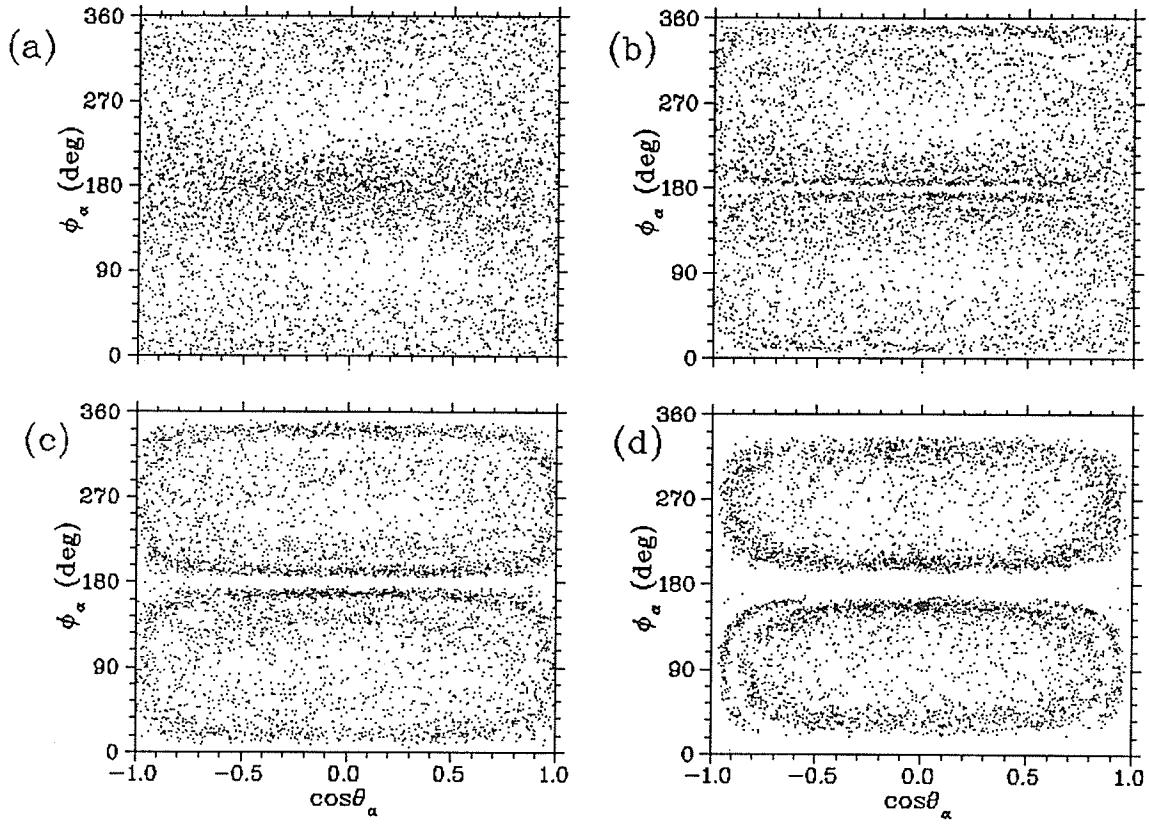

Figure 4.13: Event target reconstruction distributions for various PSD arrays with element sizes: (a)$1.0 \times 1.0 cm^2$, (b) $2.0 \times 2.0 cm^2$, (c) $3.0 \times 3.0 cm^2$, (d) $6.0 \times 6.0 cm^2$.

Table 4.13: Fitting Results (4 Element Sizes of PSD, 4 Record Arrays, SCFD counts 8737)

Size(cm^2)	Record Array	t_{00}	t_{20}	$Re(t_{22})$	$Im(t_{22})$	$\frac{\chi^2}{\nu}$
0.5x0.5	8 x 4	1.013 ±0.011	-0.241 ±0.028	-0.632 ±0.019	0.212 ± 0.019	1.69
	8 x 8	1.013 ±0.011	-0.220 ±0.025	-0.625 ±0.018	0.212 ±0.018	1.90
	8 x 12	1.013 ±0.011	-0.203 ±0.025	-0.615 ±0.018	0.217 ±0.018	2.45
	16 x 14	1.012 ±0.011	-0.178 ±0.024	-0.599 ±0.016	0.197 ±0.016	2.62
1.5x1.5	8 x 4	1.012 ±0.011	-0.229 ±0.029	-0.581 ±0.019	0.219 ±0.019	2.86
	8 x 8	1.012 ±0.011	-0.233 ±0.026	-0.581 ±0.018	0.227 ±0.018	2.49
	8 x 12	1.012 ±0.011	-0.225 ±0.025	-0.581 ±0.018	0.229 ±0.012	2.63
	16 x 14	1.013 ±0.011	-0.266 ±0.025	-0.611 ±0.016	0.211 ±0.016	2.801
3.0x3.0	8 x 4	1.013 ±0.011	-0.219 ±0.029	-0.625 ±0.020	0.236 ±0.019	1.95
	8 x 8	1.013 ±0.011	-0.219 ±0.027	-0.623 ±0.019	0.242 ±0.018	1.72
	8 x 12	1.013 ±0.011	-0.221 ±0.026	-0.615 ±0.019	0.226 ±0.018	2.20
	16 x 14	1.012 ±0.011	-0.198 ±0.025	-0.574 ±0.016	0.211 ±0.012	2.23
4.0x4.0	8 x 4	1.013 ±0.011	-0.232 ±0.030	-0.636 ±0.020	0.216 ±0.020	1.70
	8 x 8	1.013 ±0.011	-0.218 ±0.027	-0.623 ±0.020	0.214 ±0.019	1.92
	8 x 12	1.013 ±0.011	-0.215 ±0.027	-0.616 ±0.019	0.216 ±0.019	2.25
	16 x 14	1.012 ±0.011	-0.182 ±0.026	-0.571 ±0.017	0.214 ±0.017	2.88

Chapter 5

The ^{4}He Gas Target Design and the Pressure Test

Feasibility investigations discussed in the preceding chapters have demonstrated the practicality of the proposed polarization measurement. Therefore we are now proceeding with the preparatory work of designing and building a target.

In the following sections, first we will give comments on the target design based on physical considerations. Then we will discuss how to realize this design and actually build the target. Finally, the results of some pressure tests carried out on a prototype target will be given.

5.1 Physical Considerations of the Target Design

The general aspects of the target have already been displayed in Chapter 3, where various target parameters are listed and introduced into the Monte Carlo calculations. Here we provide some further design considerations based on other physical aspects of the measurement.

5.1.1 ^{4}He Gas Target

As pointed out in Chapter 2, the proposed polarization measurement is made in a sequential decay process where the intermediate nuclear state is characterized by a width of $0.6MeV$ FWHM. If we want to map this state in some detail over the resonance, the resolution will have to be ~0.1 MeV.

This means that reconstruction of events for calculating the ^{5}He polarization requires good position and energy resolution for both the pion and α particle. Energy resolution for the pion is required in order to determine the excitation energy of the ^{5}He. Using the Dispersion Matching beam, this can be accomplished if the position of the reaction event is determined to $\sim 1mm$. For the α-particle, the energy loss in an adequately thick ^4He target is such that, without corrections, it would be difficult to extract the polarization information. However, in order to apply energy loss corrections, the path-length of the α-particles in the gas must be measured.

Both of the requirements can be met if the active target volume extends over $\sim 3cm$ and contains the ^4He gas. The gas density should be chosen such that an adequate event rate can be generated. In Experiment E564, the time to accumulate 2000 events is typically 0.5hr (at angles $\leq 90°$) for the target thickness $\sim 140mg/cm^2$ and beam current $\sim 60nA$. Hence If 6000 counts are expected in the proposed experiment using a beam current $\sim 30nA$ (in order to reduce the flux on SASP which will sits on the forward direction) and the data taking time is not longer than, say 20hrs at one angle (for two settings of SASP measurements), then the target thickness of $\sim 20mg/cm^2$, or density of $\sim 7.0mg/cm^2$ is needed. This implies an increase of the ^{4}He gas density by about 40 times from STP ($0.1785mg/cm^3$), and can be realized by increasing the pressure P to 10 ATM and lowering the temperature T down to 77 K (liquid N_2) since, ideally speaking, gas density is proportional to $\frac{P}{T}$.

Geometrically, we prefer a cylindrical design of the target. This provides for the widest accessibility to the active target volume over a large angular range.

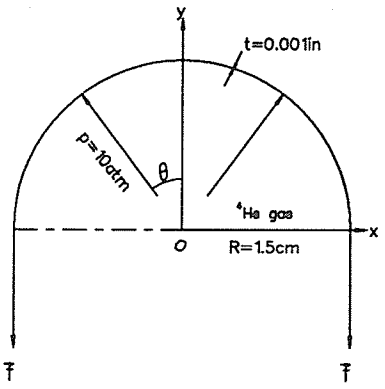

Figure 5.1: The Schematic of the Stress Calculation

To avoid the possibility of the fringes of the beam striking the massive body of the target (see §5.2 below), the height was made equal to 8 cm (The Dispersion-Matching beam, spans about $\pm 1.6cm$ vertically).

5.1.2 Target Wall

The target wall should be strong enough to hold 10 ATM pressure as well as producing the least energy loss and multiple scattering. A compromise arrangement is to use strong, thin material. Havar alloy foil, usually used in high pressure targets of nuclear physics experiments, will be used here with a thickness of 0.001in ($\sim 20mg/cm^2$). We have performed pressure tests with 0.001in stainless steel foil as the target wall, and determined that the blow out pressure is about 10 ATM.

We also performed the stress calculation for the foil. Consider, in an ideal case as shown in Fig. 5.1, a *'long'* and half walled thin tube of length l and radius R, containing gas with p ATM pressure. In the y direction the force is

$$F_y = 2l \int_0^{\frac{\pi}{2}} (p-1)\cos\theta R d\theta = 2(p-1)Rl. \tag{5.1}$$

F_y is balanced by the force $2fl$, where f is the force per unit length in wall. The stress of the foil can be further calculated by

$$\sigma = \frac{f}{t} = \frac{(p-1)R}{t}. \tag{5.2}$$

where t is the thickness of the foil. With the values of p, R and t substituted in, (5.2) yields

$$\sigma = 7.8 \times 10^4 \ psi.$$

This is a value close to the yield point of stainless steel and is consistent with our test result. However, since Havar (the yield strength is $2.4 - 2.7 \times 10^5 \ psi$) is much stronger than stainless steel, the possibility of holding 10 ATM is ensured if we think only from the point of the material strength.

Effective A and Z values of Havar are very close to those of steel. 60 MeV α particles will lose 2 MeV energy on average and, a maximum 2° multiple scattering results in the 0.001in Havar foil (See Fig 3.10(d) and Fig 3.11(d)).

5.2 Target Construction

Mechanically, a target design to realize the physical requirements is a difficult task. The difficulty is how we can hold the 10 ATM pressure in a cylindrical cell with only 0.001in foil as the wall and at the same time, cool it to 77 K. Other related problems are leakage at joints and foil bulging etc.

A design was adopted consisting of a semi-cylindrical foil mounted on a straight extended brass body as shown in Fig. 5.2. Fig. 5.3 shows the drawing of the target body in both the side and the top view. The foil is firmly fixed to the body by a detachable frame. A large enough hollow volume on the back of the target body is used to fill in liquid N_2 to cool the target. On the body, along the area where the frame and the foil meet, a narrow groove is cut for laying the indium wire. When the frame is tightly fastened to the body, the indium will seal the gap in between the foil and the body and keep the 10 ATM ^4He gas within the wall without leaking.

Fig. 5.4 illustrates a practical arrangement of the reaction geometry.

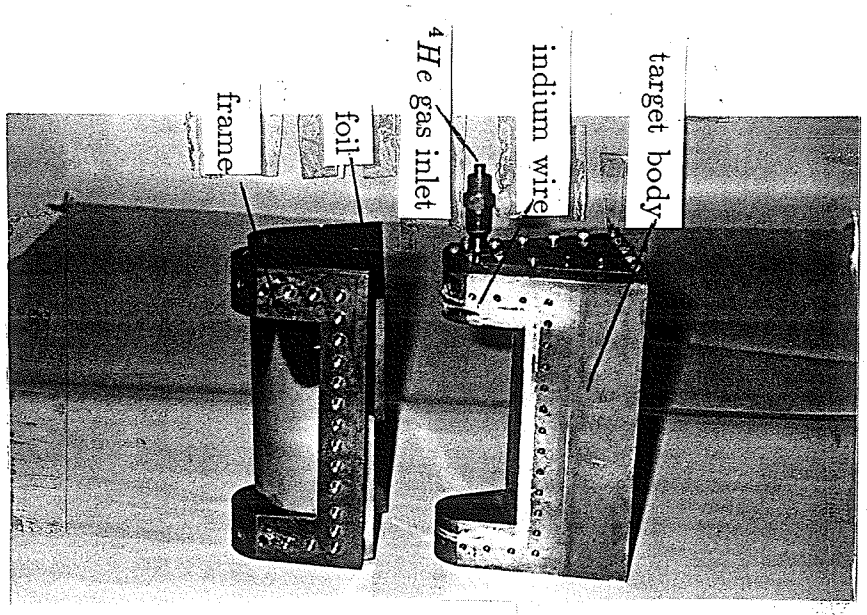

(a)

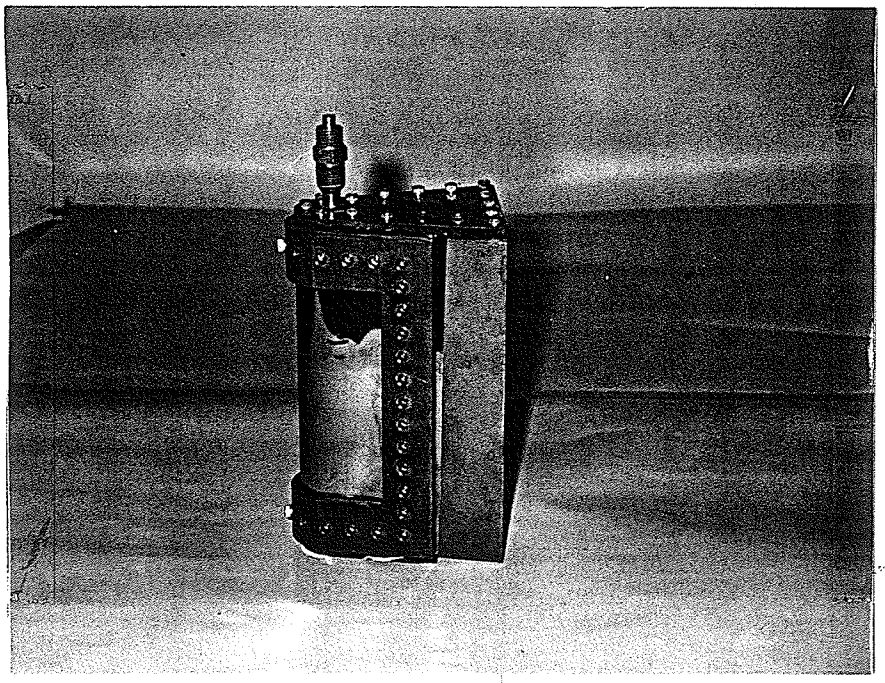

(b)

Figure 5.2: The prototype of the target: (a) a taken apart view, (b) an intact target.

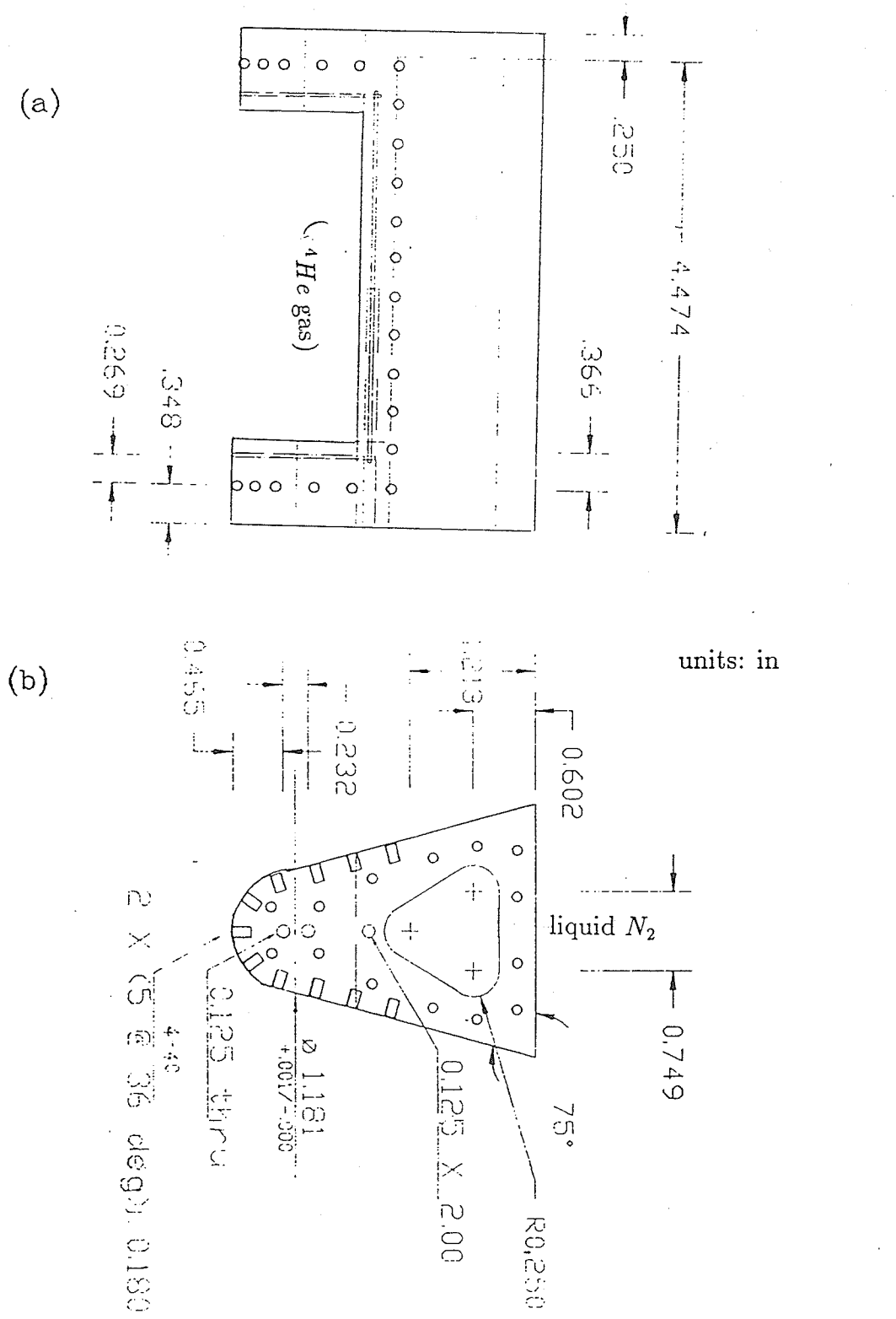

Figure 5.3: The drawing of the target body. (a): the side view and (b): the top view.

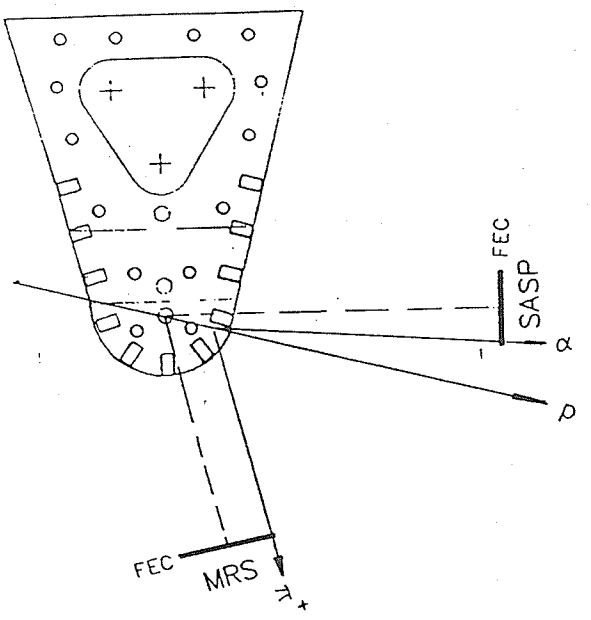

Figure 5.4: A practical arrangement of the reaction geometry (top view)

5.3 Target Pressure Tests

Target tests included pressure tests to the rupture point, and also the long term leak tightness. These two points are essential to the target.

Due to the cost of Havar foil, we used a $0.001in$ thickness of stainless steel foil for these tests. The test was performed with high pressure ^4He gas contained in a gas cylinder. Fig 5.5 shows a schematic view of the arrangement. The target was put under water in a basin in order to observe any bubbles that would indicate leaks, and pinpoint areas in the seal that were faulty. A further reason for putting the target under water had to do with safety. The presence of a heavy glass plate and the water provided protection for the person performing the tests.

We performed four tests in all. Before each test, the grooves where the indium sealing wire was placed were cleaned very carefully, and so were the foil and the fixing frame. After the grooves were filled with indium wire uniformly, we placed the foil and then the fixing frame on the target body and tightened the screws around the grooves symmetrically on both ends and both sides. The tightening

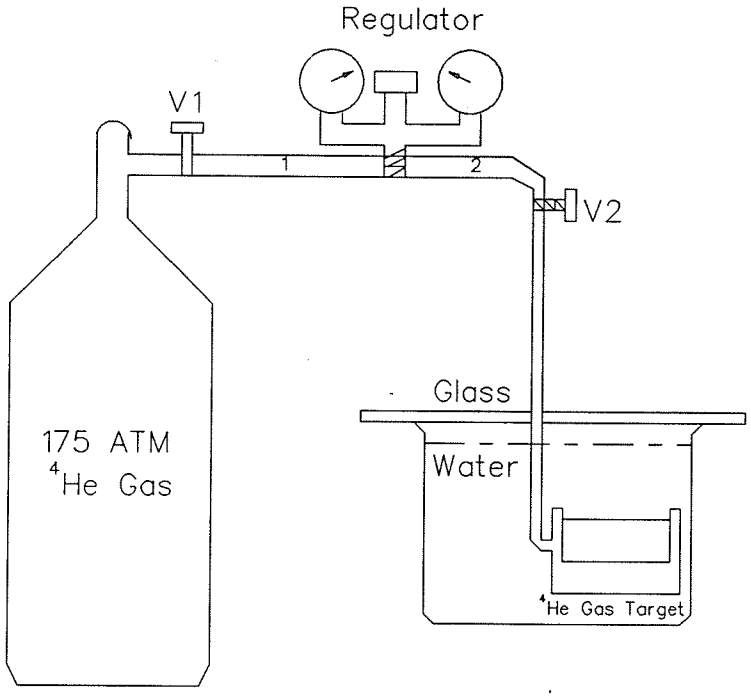

Figure 5.5: The Schematic View of the Target Test

Table 5.1: Target rupture tests

Test No.	1	2	3	4
Rupture Pressure (ATM)	9.0	10.7	8.6	13.0

was done little by little in several rounds for the purpose of obtaining a uniform seal.

5.3.1 Rupture Pressure

The target rupture tests are listed in Table 5.1. In two cases (test 1 and test 3), the target leaked considerably compared to the other two cases (test 2 and test 4) cases.

In test 1 and test 3 , the leaking was minimal at lower pressures (2 or 3 ATMs). However, as the pressures increased, leaking became more apparent as

Table 5.2: The long term leak test results

Test 2	98 psi	$\xrightarrow{5hrs}$	40 psi	$\xrightarrow{2hrs}$	35 psi
	90 psi	$\xrightarrow{1.5hrs}$	60 psi	$\xrightarrow{16hrs}$	15 psi
Test 4	120 psi	$\xrightarrow{1hr}$	82 psi	$\xrightarrow{22hrs}$	30 psi
	120 psi	$\xrightarrow{1hrs}$	80 psi	$\xrightarrow{19hrs}$	34 psi

more and more bubbles appeared. The maximum pressure attained was relatively low at rupture, the foil pulling away from the frame at the points where the leaks occurred. Later, on examination, it was found that the transition place from the cylindrical surface to the straight section was not properly constructed. At these transitions, the seal had not been made properly, resulting in weak spots where the foil was pulled away from the body. In test 2 and test 4 no leaking was observed up to the rupture pressure. These pressures were considerably higher than those in the leaking cases.

5.3.2 Leak Tightness

Although in test 2 and test 4 no observable leaking was found, it is still necessary to know if the target will function over a long period of time. We have two observations for each of test 2 and test 4. The results are listed in Table 5.2. Apparently, a leak existed in the system.

Later we checked the leak tightness of the other two parts in the gas system besides the target cell. The first part is labeled 1 and 2 (See Fig. 5.5) beyond V2. With V2 closed, the pressure can be kept for even a few weeks. The second part is a piece of ~3m long poly-flo connecting V2 and the target. We disconnected the poly-flo from the target and sealed the opened end using a stopper. The test result is

$$100 \text{ psi} \xrightarrow{3.5hrs} 60 \text{ psi} \xrightarrow{36hrs} 20 \text{ psi}$$

since no leaking bubbles were observed at the sealed end, the leak can only be the

gas diffusion through the poly-flo wall (^4He gas can easily diffused through the plastic material). Such a test offered additional proof of the leak tightness of the target.

When the target was pressurized, the foil bulged out a little from its nearly half cylindrical shape and also, small dips and bumps appeared on the central area of foil. These tiny deformations did not change as the pressure increased up to the rupture point.

Chapter 6

Conclusion

The feasibility investigation shows that the angular correlation measurements between the π^+ and α particle permit determination of the ^{5}He(g.s., $\frac{3}{2}^-$) k=2 polarization tensors arising from the ^{4}He($\vec{p}, \pi^+$)^{5}He reaction at T_p=400 MeV. The full distribution measurement of α-particles from the breakup ^{5}He(g.s., $\frac{3}{2}^-$) $\rightarrow$ n + α with a large acceptance detector, rather than just taking measurements in several planes, demonstrated the practicality of this method in the extraction of the polarization tensors. TRIUMF DASS/SASP facility is capable of performing such a coincidence measurement for ^{5}He excitation up to 3.3 MeV.

It has been shown that the Monte Carlo simulations of the individual harmonic functions are necessary and their target reconstruction distributions do a good job in being used as the base functions to fit the fully simulated correlation function distributions. The fitting results show that the greater the total counts, the closer the extracted tensors are to the input values. When the total number of counts is more than $\sim$ 25000, the differences between the extracted tensors and those of the input values are at the level of the statistical errors, and the errors due to the cancellation of events in the individual distributions are negligible. In addition, as the total counts reach more than $\sim$12000, the extracted values do not depend strongly on the record bin size.

The target pressure tests show that, generally speaking, the target designs are

reasonable, and the Havar foil, if used, could stand the 10 ATM pressures.

Bibliography

[1] D. F. Measday and G. A. Miller, Annu. Rev. Nucl. Part. Sci. 29, 121 (1979); B. Hoistad, in *Advances in Nuclear Physics*, edited by J. Negele and E. Vogt (Plenum, New York, 1979), Vol. 11, p. 135; H. W. Fearing, in *Progress in Particle and Nuclear Physics* , edited by D. H. Wilkinson (Pergamon, Oxford, 1981), Vol. 7, p. 113; *Pion Production and Absorption in Nuclei - 1981 (Indiana University Cyclotron Facility*, Proceedings of the Conference on Pion Production and Absorption in Nuclei, AIP Conf. Proc. No. 79, edited by Robert D. Bent (AIP, New York,1982).

[2] E. G. Auld et al, Phys. Rev. Lett. 44, 462 (1978).

[3] T. P. Sjoreen et al, Phys. Rev. C24, 1135 (1981).

[4] E. Korkmaz et al, Phys. Rev. Lett. 58, 104 (1987).

[5] K. M. Furutani, *Pion Production from Few Nucleon Systems in the Region of the* Δ_{1232} *Resonance*, Ph.D. thesis, University of Manitoba, 1991 (unpublished).

[6] B. Hoistad, Phys. ReV. C 29, 553 (1984).

[7] M. Simonius, *Theory of Polarization Measurements, Observables and Symmetries*, Polarization Nuclear Physics, Lecture notes in Physics 30, Springer Verlag, 1974.

[8] *Polarization Phenomena in Nuclear Reactions*, edited by H. H. Barschall and W. Haeberli, p. xxv., University of Wisconsin Press, Madison, 1971.

[9] G. R. Satchler, *Direct Nuclear Reactions*, Oxford University Press, 1983.

[10] G. G. Ohlsen, Rep. Prog. Phys. 35, 717 (1972).

[11] N. S. Zelenskaya and I. B. Teplov, Nucl. Phys. A406, 306 (1983).

[12] J. Campbell, *Tensor Polarization of* ^{12}C *(15.11MeV,* 1^+*) in the* $^{13}C(p,d)^{12}C^*_{\rightarrow^{12}C(g.s.)+\gamma}$ *reaction at* E_p*=41.3 MeV*, Ph.D. thesis, University of Manitoba, 1986.

[13] P. Heiss, Z. Physik, A272, 267 (1975).

[14] K. Wick et al, Nucl. Phys., A444, 49 (1985)

[15] K. Prescher et al, Nucl. Phys., A286, 142 (1977).

[16] F. Pougheon et al, Nucl. Phys., A325, 481 (1979).

[17] A.Aryainejad, *Annual Research Report 1984-85*, University of Manitoba Cyclotron Laboratory, Winnipeg, Canada.

[18] F. Ajzenberg-Selove, Nucl. Phys., A413, 8 (F1984).

[19] M. J. Balbes et al, Phys. Rev., C43, 343 (1991).

[20] H. W. Fearing, *Pion Production in Nuclei: Things Known and Unknown*, Progress in Particle and Nuclear Physics, Vol. 7, Pergamon Press, 1981.

[21] W. R. Falk and K. M. Furutani, *Investigation of* (p,π^+) *Reactions on* ^3He *and* ^4He *in the Region of the* Δ_{1232} *Resonance,* Proceedings of the International Workshop on Pions in Nuclei, Peniscola, Spain, 1991, edited by E. Oset and M. J. Vicente-Vacas (World Scientific).

[22] H. A. Bethe, Ann. Physik 5, 325 (1930).

[23] P. V. Vavilov, SOVIET PHYSICS JETP 5, 749 (1957).

[24] S. P. Ahlen, Rev. of Modern Phys. 52, 121 (1980).

[25] W. H. Beyer, *CRC Standard Mathematical Tables*, 26th Edition, CRC Press, 1981.

[26] G. D. Badhwar, Nucl. Instru. and Meth. 109, 119 (1973).

[27] J. H. Adams and G. D. Badhwar, Nucl. Instru. and Meth. 124, 553 (1975).

[28] W. H. Press et al, *Numerical Recipes*, The Art of Scientific Computering, Cambridge University Press, 1986.

[29] S. Kuhn et al, Nucl. Instru. and Meth. in Phys. Rese., B4, 332 (1984).

[30] H. A. Bethe, Phys. Rev. 89, 1256 (1953).

[31] J. B. Marian and B. A. Zimmermann, Nucl. Instru. and Meth. 51, 93 (1967).

[32] J. Germond and C. Wilkin, J. Phys. G: Nucl. Phys. 11, 1131 (1985)

[33] Y Le Bornec et al, J. Phys. G: Nucl. Phys. 11, 1125 (1985)

[34] *Medium Resolution Spectrometer (MRS) Manual*, TRIUMF, 1988.

[35] P. H. Orth et al, Nucl. Instru. and Meth. 65, 301 (1968).

[36] Tipei Li, *Mathematical Processing of Experimental Data*, China Academia Sinica Press, 1980.

[37] M. E. Rose, *Elementary Theory of Angular Momentum*, John Wiley, 1957.

[38] J. J. Sakurai, *Modern Quantum Mechanics*, Addison-Wesley, 1985.

Appendix A

Reference Frames and Rotations

A general rotation may be represented by the Euler angles. The convention for the order of rotations used is[37]:

(a) a right-hand rotation about the z-axis by an angle α

(b) a right-hand rotation by an angle β about the y-axis which resulted from rotation a)

(c) a right-hand rotation by an angle γ about the z-axis which resulted from rotation b)

The quantum mechanical rotation matrix is given by:

$$D(\alpha,\beta,\gamma) = e^{-i\alpha J_z} e^{-i\beta J_y} e^{-i\gamma J_z} \tag{A.1}$$

which in a standard representation becomes,

$$D^J_{M',M}(\alpha,\beta,\gamma) =< J,M'|D|J,M >= e^{-i\alpha M'} d^J_{M',M}(\beta) e^{-i\gamma M} \tag{A.2}$$

where

$$d^J_{M',M}(\beta) =< J,M'|e^{-i\beta J_y}|J,M >$$

The Wigner formula for $d^J_{M',M}(\beta)$ is[38]:

$$\begin{aligned} d^J_{M',M}(\beta) = \; & \textstyle\sum_k (-1)^{k-M+M'} \frac{\sqrt{(J+M)!(J-M)!(J+M')!(J-M')!}}{(J+M-k)!k!(J-k-M')!(k-M+M')!} \\ & \times (\cos\tfrac{\beta}{2})^{2J-2k+M-M'} (\sin\tfrac{\beta}{2})^{2k-M+M'} \end{aligned} \tag{A.3}$$

Table A.1: $d^2_{M',M}(\beta)$

$M' \rightarrow$ $M \downarrow$	-2	-1	0	1	2
-2	$\cos^4\frac{\beta}{2}$	$\cos^2\frac{\beta}{2}\sin\beta$	$\sqrt{\frac{3}{8}}\sin^2\beta$	$\sin^2\frac{\beta}{2}\sin\beta$	$\sin^4\frac{\beta}{2}$
-1	$-\cos^2\frac{\beta}{2}\sin\beta$	$\cos^4\frac{\beta}{2}-\frac{3}{4}\sin^2\beta$	$\sqrt{\frac{3}{8}}\sin 2\beta$	$\frac{1}{2}(\cos\beta-\cos 2\beta)$	$\sin^2\frac{\beta}{2}\sin\beta$
0	$\sqrt{\frac{3}{8}}\sin^2\beta$	$-\sqrt{\frac{3}{8}}\sin 2\beta$	$\frac{1}{2}(\cos^2\beta-\cos 2\beta)$	$\sqrt{\frac{3}{8}}\sin 2\beta$	$\sqrt{\frac{3}{8}}\sin^2\beta$
1	$-\sin^2\frac{\beta}{2}\sin\beta$	$\frac{1}{2}(\cos\beta-\cos 2\beta)$	$-\sqrt{\frac{3}{8}}\sin 2\beta$	$\cos^4\frac{\beta}{2}-\frac{3}{4}\sin^2\beta$	$\cos^2\frac{\beta}{2}\sin\beta$
2	$\sin^4\frac{\beta}{2}$	$-\sin^2\frac{\beta}{2}\sin\beta$	$\sqrt{\frac{3}{8}}\sin^2\beta$	$-\cos^2\frac{\beta}{2}\sin\beta$	$\cos^4\frac{\beta}{2}$

where the sum is taken over k whenever none of the arguments of factorials in the denominator are negative. The $d^2_{M',M}(\beta)$ are listed on Table A.1.

A rotation may be taken from two viewpoints: one termed the *passive* rotates the coordinate system, keeping the space and state fixed, the other, termed the *active*, rotates the space and state, keeping the coordinate axes fixed. Both points of view are equivalent, although the rotation matrix is applied differently in the two cases.

The statistical tensors rotate in the following way:

$$t^{II}_{kq} = \sum_{q'} D^k_{q',q}(\alpha,\beta,\gamma)t^I_{kq'} \quad Passive \tag{A.4}$$

$$t'_{kq} = \sum_{q'} D^{k*}_{q',q}(\alpha,\beta,\gamma)t_{kq'} \quad Active \tag{A.5}$$

These tensors are expressed in a spherical representation and transform in the same manner as spherical harmonics. The viewpoint used in our calculation is the *passive* one.

In §4.3, the Euler angles rotating the transverse frame to helicity frame are $(\alpha,\beta,\gamma) = (0, 90°, 90°)$. Therefore the tensor rotations for rank $k = 2$ will take the form:

$$t^H_{2q} = \sum_{q'=-2}^{2} d^2_{q'q}(90°)e^{-i\frac{\pi}{2}q}t^T_{2q'} \tag{A.6}$$

Now with the various $d^2_{q'q}(90°)$ from the Table A.1, we can calculate t^H_{2q} in terms of $t^T_{2q'}$.

As is pointed out in §2.5, the transition amplitudes for reaction ^{4}He$(\vec{p},\pi^+)^5$He are calculated under a frame termed *beam helicity frame.* The Euler angles which bring the *Beam Helicity Frame* onto the *recoil transverse frame* are readily seen from Fig 2.3 to be:

$$(\alpha,\beta,\gamma) = (90°, 90°, 180° - \theta^c_{^5\mathrm{He}})$$

where $\theta^c_{^5\mathrm{He}}$ is the ^{5}He center of mass(for ^{4}He$(\vec{p},\pi^+)^5$He reaction) scattering angle around which the breakup distributed. Thus the rotation of the tensor from the beam helicity frame to the recoil transverse frame will be:

$$t^T_{2q} = \sum_{q'=-2}^{2} e^{-i\frac{\pi}{2}q'} d^2_{q'q}(\frac{\pi}{2}) e^{-iq(\pi-\theta^c_{^5\mathrm{He}})} t^{BH}_{2q'} \qquad \text{(A.7)}$$

Appendix B

Additional Geometries

1. In $OXYZ$ frame on Fig 3.1, the equations for the target wall surfaces are:

$$\begin{aligned} X^2 + Z^2 &= R^2 && inner\ surface \\ X^2 + Z^2 &= (R + TD)^2 && outer\ surface \end{aligned}$$

2. The pion and α detector acceptance plane equations:

$$\begin{aligned} X = &\quad L_{\pi d}\sin\Theta_{\pi d} - \tfrac{1}{\tan\Theta_{\pi d}}(Z - L_{\pi d})\cos\Theta_{\pi d} && \pi^+\ detector \\ X = &-L_{\alpha d}\sin\Theta_{\alpha d} - \tfrac{1}{\tan\Theta_{\alpha d}}(Z - L_{\alpha d})\cos\Theta_{\alpha d} && \alpha\ detector \end{aligned}$$

3. If the intersection coordinates of the final pion trajectory with the pion acceptance plane is (X_π, Y_π, Z_π) in $OXYZ$ frame, then the coordinates transformation to $o_{\pi d}x_{\pi d}y_{\pi d}$ frame to get the pion record position is:

$$\begin{aligned} x_{\pi d} &= -Z_\pi \sin\Theta_{\pi d} + X_\pi \cos\Theta_{\pi d} \\ y_{\pi d} &= Y_\pi \end{aligned}$$

The similar transformation for α is:

$$\begin{aligned} x_{\alpha d} &= Z_\alpha \sin\Theta_{\alpha d} + X_\alpha \cos\Theta_{\alpha d} \\ y_{\alpha d} &= Y_\alpha \end{aligned}$$

4. In step 2 of § 3.2.3, the coordinate transformation from recoil CM transverse frame $oX_TY_TZ_T$ to helicity frame $oX_HY_HZ_H$ is:

$$\begin{pmatrix} 0 & 0 & 1 \\ 1 & 0 & 0 \\ 0 & 1 & 0 \end{pmatrix}$$

if α direction (θ_T, ϕ_T) was chosen according to the distribution of one W_i, then the direction unit vector in helicity frame is

$$\hat{\mathbf{n}}_H = (\cos\theta_T, \sin\theta_T \cos\phi_T, \sin\theta_T \sin\phi_T)$$

So the direction (θ_H, ϕ_H) was determined by:

$$\begin{aligned} \cos\theta_H &= \sin\theta_T \sin\phi_T \\ \tan\phi_H &= \frac{\sin\theta_T \cos\phi_T}{\cos\theta_T} \end{aligned}$$

5. In step 4 of § 3.2.3, we could write down the α direction unit vector $\hat{\mathbf{n}}_\alpha$ in frame $oxyz$ using the transformation from frame $oX_HY_HZ_H$ to frame $oxyz$:

$$\hat{\mathbf{n}}_\alpha = \begin{pmatrix} \hat{\mathbf{n}}_{X_H,x} & \hat{\mathbf{n}}_{X_H,y} & \hat{\mathbf{n}}_{X_H,z} \\ \hat{\mathbf{n}}_{Y_H,x} & \hat{\mathbf{n}}_{Y_H,y} & \hat{\mathbf{n}}_{Y_H,z} \\ \hat{\mathbf{n}}_{Z_H,x} & \hat{\mathbf{n}}_{Z_H,y} & \hat{\mathbf{n}}_{Z_H,z} \end{pmatrix} \cdot \begin{pmatrix} \sin\theta_{HL} \cos\phi_{HL} \\ \sin\theta_{HL} \sin\phi_{HL} \\ \cos\theta_{HL} \end{pmatrix}$$

Appendix C

Some Short Notations in the Text

IHF Individual Harmonic Function

LPED Lab Position and Energy Distribution

SED Simulating Experimental Data

SCFD Simulated Correlation Function Distribution

SIFD Simulated Individual Function Distribution

TRA Target Reconstruction Apparatus

MRS Medium Resolution Spectrometer

SASP Second Arm Spectrometer

DASS/SASP Dual Arm Spectrometer/Second Arm Spectrometer

FEC Front End Chamber

PSD Position Sensitive Detector

STP Standard Temperature and Pressure

ATM Atmospheric Pressure

Appendix D

TRIUMF DASS/SASP and Beam Line 4B Specifications

TABLE I SASP Specifications		
Designed Central Momentum		680 MeV/c
Maximum Central Momentum		759 MeV/c
Momentum Acceptance		-10% to +15% ΔP/P
Solid Angle	at -10% ΔP/P at - 5% ΔP/P at 0% ΔP/P at + 5% ΔP/P at +10% ΔP/P at +15% ΔP/P	11.2 msr 13.0 msr 13.5 msr 12.8 msr 11.6 msr 10.0 msr
Resolution @ 680 MeV/c (FWHM) (with 2mr multiple scattering at focal plane)		0.02% ΔP/P
D/M		4.70 cm/%
Flight path @ 680 MeV/c		7.02 m
Angular Acceptance:	bend plane non-bend plane	±103 mr ±42 mr
Focal Plane Tilt		44.3°
Total Bend Angle		90°
Angular Range		14-156°
Angular Resolution (1 mm beam spot with no front end chamber)		2 mr
Maximum target spot size (full acceptance)	vertical horizontal	10 cm 4 cm
Minimum opening angle with the MRS		40°
Minimum opening angle with the beam line		14°

TABLE II MRS Specifications	
Maximum Designed Central Momentum	1400 MeV/c
Momentum Acceptance	-6% to +6% ΔP/P
Solid Angle	1-2.5 msr
Resolution	0.01% ΔP/P
D/M	10.0 cm/%
Flight path	11.0 m
Focal Plane Tilt	45.0°
Total Bend Angle	60°
Angular Range LAC configuration SAC configuration	 15-135° -16↔16°
Angular Resolution (with front end chamber)	1 mr
Focal Plane Polarimeter (FPP) scattering angle acceptance	20° in 2π azimuth

TABLE III 4B Specifications	
Maximum Momentum	1090 MeV/c
Dispersion for momentum matching	0 to 20 cm/%
Emittance (from cyclotron)	H 8.0 π mm·mr V 1.0 π mm·mr
Resolution	~0.15% ΔP/P
Polarization any direction n,t, & l	70.0%
Intensity polarized unpolarized	 100 na 1 μa

Hamilton Precision Metals
1780 ROHRERSTOWN ROAD, P.O. BOX 3014, LANCASTER, PA 17604-3014
PHONE (717) 569-7061 FAX (717) 569-7642

Appendix E Havar

DESCRIPTION:

HAVAR is a non-magnetic, corrosion resistant, cobalt-base alloy which exhibits high strength and a high fatigue endurance limit.

NOMINAL COMPOSITION:

Cobalt	42.5%	Beryllium	.04%
Nickel	13.0%	Manganese	1.60%
Chromium	20.0%	Tungsten	2.80%
Molybdenum	2.0%	Iron	Bal.
Carbon	.20%		

TYPICAL MECHANICAL PROPERTIES: (for strip cold reduced 75%)

	As Rolled	Age Hardened
Ultimate Tensile Strength	260,000 – 290,000 psi	320,000 – 350,000 psi
Yield Strength (at .2% offset)	235,000 – 265,000 psi	300,000 – 330,000 psi
Hardness (Rockwell C)	44 – 50	56 – 60

See Figures 1 and 2 for mechanical properties as a function of cold reduction.

PHYSICAL CONSTANTS:

Density	8.3 gm./cc.	.300 lb./cu. in.
Linear Coefficient of Thermal Expansion		12.5 x 10^6 in/in/°C (0–50°C)
Electrical Resistivity		91.4 microhm cm.
Modulus of Elasticity (Tension)		29.5 – 30.2 x 10^6 psi

PRODUCT CHARACTERISTICS:

The outstanding mechanical properties of HAVAR are developed through a combination of cold working and heat treatment. HAVAR work hardens readily, and for many applications the as-rolled properties are adequate. A simple heat treatment will bring about a substantial increase in the strength and hardness of the as-rolled material, however, solution annealed HAVAR will not respond to the age hardening treatment. HAVAR can be utilized at elevated temperatures, especially in spring applications, with highly satisfactory results. A maximum service temperature of 750°F is recommended. Although maximum strengthening is achieved by heat treating for 3 hours at 950°F to 1000°F, the time can be varied from 3 to 5 hours, depending upon the required properties. In all cases, the treatment should be carried out in vacuum or a dry hydrogen atmosphere.

For applications requiring high fatigue life, HAVAR has demonstrated excellent characteristics when rolled to 75% to 80% cold work and heat treated for 3 hours at 1000°F.

With a magnetic permeability on the order of 1.00004 at room temperature, HAVAR is sufficiently non-magnetic for most applications requiring this characteristic. After exposing a HAVAR specimen to a field of 5000 Oersteds, no residual magnetism could be detected with a search coil of 50 Gauss sensitivity.

Conventional machining of HAVAR can be accomplished, however, not without some difficulty since it work hardens rapidly in front of the cutting tool. Carbide cutting tools used with a cutting fluid of soluble oil in water are generally recommended. Machining operations should be performed on material in the cold worked condition, prior to the final heat treatment.

HAVAR is produced in the form of vacuum melted rod (1" dia. max), wire, strip, and foil in accordance with the standard tolerances.

APPLICATIONS:

Mainsprings
Powersprings
Flat Springs
Drive Bands
Torsion Bars
Flexures
Orthodontic Wire
Pressure Diaphragms
Gap Spacers for Magnetic Recording Heads
Gas Target Foils for Nuclear Physics

Fig. 1
Effect of % Cold Reduction on Strength Properties of .005 Strip "as rolled" and "heat treated at 1000°F"

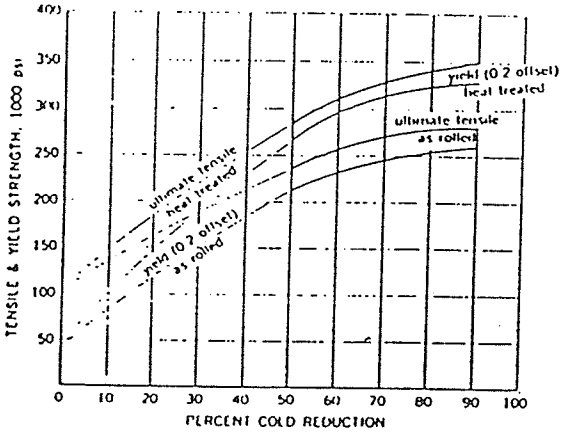

Fig. 2
Effect of % Cold Reduction on Hardness of .005 Strip "as rolled" and "heat treated at 1000°F"